Nanoscale quantification of stress and strain in III-V semiconducting nanostructures

by

Eric James Jones

B.S. in Materials Science and Engineering

North Caroline State University, 2009

SUBMITTED TO THE DEPARTMENT OF

MATERIALS SCIENCE AND ENGINEERING

IN PARTIAL FULFILLMENT OF THE REQUIREMENTS FOR THE DEGREE OF

DOCTOR OF PHILOSOPHY IN

MATERIALS SCIENCE AND ENGINEERING

AT THE

MASSACHUSETTS INSTITUTE OF TECHNOLOGY

June 2015

Signature of Author: _____

Department of Materials Science and Engineering
April 9th, 2015

Certified by: _____

Silvija Gradečak
Thomas Lord Assistant Professor of Materials Science and Engineering
Thesis Supervisor

Accepted by: _____

Donald R. Sadoway
John F. Elliot Professor of Materials Chemistry
Chair, Departmental Committee on Graduate Students

Nanoscale quantification of stress and strain in III-V semiconducting nanostructures

by
Eric J. Jones

Submitted to the Department of Materials Science and Engineering on March 5, 2015 in Partial Fulfillment of the Requirements for the Degree of Doctor of Philosophy in Materials Science and Engineering

Abstract

III-V semiconducting nanostructures present a promising platform for the realization of advanced optoelectronic devices due to their superior intrinsic materials properties including direct band gap energies that span the visible light spectrum and high carrier mobilities. Additionally, the inherently high surface-to-volume ratio of nanostructures allows for the efficient relaxation of stress enabling the realization of defect free heterostructures between highly mismatched materials. As a result, nanostructures are being investigated as a route towards the direct integration of III-V materials on silicon substrates and as platforms for the fabrication of novel heterostructures not achievable in a thin film geometry. Due to their small size, however, many of the methods used to calculate stress and strain in 2D bulk systems are no longer valid as free surface effects allow for relaxation creating more complicated stress and strain fields. These inhomogeneous strain fields could have significant impacts on both device fabrication and operation. Therefore, it will be vital to develop techniques that can accurately predict and measure the stress and strain in individual nanostructures.

In this thesis, we demonstrate how the combination of advanced transmission electron microscopy (TEM) and continuum modeling techniques can provide a quantitative understanding of the complex strain fields in nanostructures with high spatial resolutions. Using techniques such as convergent beam electron diffraction, nanobeam electron diffraction, and geometric phase analysis we quantify and map the strain fields in top-down fabricated InAlN/GaN high electron mobility transistor structures and GaAs/GaAsP core-shell nanowires grown by a particle-mediated vapor-liquid-solid mechanism. By comparing our experimental results to strain fields calculated by finite element analysis, we show that these techniques can provide quantitative strain information with spatial resolutions on the order of 1 nm. Our results highlight the importance of nanoscale characterization of strain in nanostructures and point to future opportunities for strain engineering to precisely tune the behavior and operation of these highly relevant structures.

Thesis Supervisor: Silvija Gradečak
Title: Thomas Lord Associate Professor of Materials Science and Engineering

Acknowledgements

This thesis was made possible only by the support, guidance and contributions of my advisor, collaborators, colleagues, friends, and family members.

I must first thank my advisor, Silvija Gradečak, for her constant support and guidance over the past six years. She has truly had a profound impact on my growth and development as a scientist and researcher, and I know the lessons I have learned being in the Gradečak group will stay with me for the rest of my life. I must also thank my committee members, Gene Fitzgerald and Lorna Gibson. Through numerous conversations and interactions, they have provided me with invaluable support throughout this work and graduate school in general.

I would also like to thank Dr. David Cooper, Dr. Jean-Luc Rouvière, and Dr. Armand Béché for their invaluable help and support in the acquisition and interpretation of NBED and GPA data. I will never forget the two weeks I was able to spend working with this dedicated and passionate group of scientists who have created one of the most exciting and enjoyable working environments I have ever had the opportunity of being in. This work was performed at the nanocharacterization platform on the MINATEC campus of the CEA in Grenoble, France, and was supported by the MIT-MISTI program.

My graduate school experience would not have been the same had it not been for the amazing group of people that I was fortunate to work with every day. Joining the Gradečak group was the best decision I have made during grad school. This exceptional group of people makes me look forward to coming to work every day. In particular, I must thank my office mates Matt, Paul, Matteo, and Zach for creating the best office in Building 13. I also have to thank the members of my second, unofficial office Sema, Jordan, and John. Despite all my trying, they never get tired of me distracting them with coffee breaks or SpaceTeam. I want to thank Xiang who came into the group at the same time I did and was a great help through classes, qualifying exams, and TEM frustrations. My thanks also goes out to the rest of the Gradečak group members and alumni – Mike, Megan, Sung Keun, Sam, Sehoon, Jayce, Zhibo, Olivia, and Kevin – who continue to make the Gradečak group the best group at MIT. GG4C!

Life in graduate school would have been impossible had it not been for the love and support of my friends in the Graduate Christian Fellowship. It has been my joy to have shared my life with this group of amazing graduate students for the past six years. You all have helped me grow deeper in my love for God and neighbor and will be deeply missed. I want to thank the members of my SidPac small group for making this tough transition period such a great year. I also want to thank the members of the Fellowship of the Ringed for the lasting friendships we have and your constant encouragement.

Of course, I would never had made it to MIT had it not been for the patient love of my family – both immediate and by law. Despite the distance between us, your thoughts and prayers have always been close and remind me of your constant love and care you have given me throughout my life. To my wife, Victoria, thank you for staying by my side for this Boston

adventure! There is no one else I would have next to me and I am excited to see what God brings our way next!

Finally, I must give all glory to my Lord and Savior Jesus Christ. It is only by His mercy that I have come this far, and it will be only by His strength that I continue on.

This work was supported by the National Science Foundation Graduate Research Fellowship program and the National Science Foundation CAREER award under award number DMR – 0745555. Access to shared experimental facilities is provided by the MIT Center for Materials Science Engineering supported in part by the MRSEC Program of National Science Foundation under award number DMR-08-19762. I would like to thank Dr. Yong Zhang and Dr. Shiahn Chen for their technical assistance.

"Here I raise my Ebenezer, Hither by Thy help I've come!"

Table of Contents

List of Figures 10

List of Tables 16

List of Abbreviations 17

Chapter 1. Introduction 18

1.1. Strain engineering in semiconducting nanostructures 19

1.2. Characterization of strain in bulk and nanostructured semiconductors 21

1.3. Materials systems of interest 22

1.3.1. InAlN/GaN nanoribbon HEMTs 22

1.3.2. III-arsenide core-shell nanowire heterostructures 24

1.4. Thesis outline 26

Chapter 2: Experimental methods – Electron microscopy 28

2.1. Electron-material interaction 28

2.2. Scanning electron microscopy (SEM) 30

2.2.1. Surface characterization and contrast mechanisms 31

2.3. Transmission electron microscopy (TEM) 32

2.3.1. Electron diffraction 33

2.3.2. Convergent beam electron diffraction and the origin of Higher order Laue zone lines 38

2.3.3. HOLZ lines for nanoscale strain measurement 41

2.3.4. Nanobeam electron diffraction 43

2.3.5. GPA 44

2.3.6. High resolution TEM 47

2.3.7. Scanning transmission electron microscopy 47

2.3.8. Energy Dispersive X-ray spectroscopy 48
2.4. Conclusions 48
Chapter 3. Experimental methods – Finite element modeling of lattice mismatched nanostructures 50
3.1. The finite element method 50
3.1.1. The FEA mesh 52
3.2. Modeling the systems of interest 53
3.2.1. Thin-film heterostructures 53
3.2.2. Core-shell nanowire heterostructures 55
3.3. CBED simulation 65
3.3.1. The Bloch wave method 65
3.4. Conclusions 69
Chapter 4. Correlating Stress Generation and Sheet Resistance in InAlN/GaN Nanoribbon High Electron Mobility Transistors 71
4.1. Introduction 71
4.2. InAlN/GaN nanoribbons for HEMT devices 72
4.3. Fabrication and characterization techniques 73
4.4. TEM investigations 74
4.4.1. Bright-field TEM 75
4.4.2. Strain analysis by CBED 77
4.5. Finite element analysis of the HEMT structure 81
4.5.1. Simulations of TEM thin films 82
4.5.2. Simulations of device-sized structures 84
4.6. Conclusions 86

Chapter 5. Towards rapid nanoscale measurement of strain in III-nitride heterostructures 87

5.1. Introduction 87

5.2. Experimental setup and characterization techniques 88

5.2.1. Nanobeam electron diffraction 89

5.2.2. Geometric phase analysis 91

5.3. Strain analysis by nanobeam electron diffraction 92

5.4. Strain analysis by geometric phase analysis 93

5.5. Finite element analysis 99

5.6. Conclusions 101

Chapter 6. Quantification of stress and strain in GaAs based core-shell nanowire heterostructures 103

6.1. GaAs/GaAsP nanowire heterostructures 103

6.2. Nanowire heterostructure fabrication and structural characterization 104

6.3. Evaluating strain characterization techniques 108

6.4. Characterizing strain in GaAs/GaAsP core-shell nanowires 110

6.4.1. HOLZ line splitting 112

6.4.2. HOLZ line shifting 114

6.5. Finite element analysis and Bloch wave simulations 116

6.5.1. The FEA model 116

6.5.2. Bloch wave simulations 118

6.5.3. The initial model 122

6.5.4. Effects of surrounding media 123

6.6. Conclusions 128

Chapter 7. Conclusions and future work 130

Appendix A.Using Jems for the simulation of CBED patterns 135

A.1. Example files..... 137

Bibliography.....142

List of Figures

Figure 1-1. Common III-V materials plotted by their energy band gap and lattice parameter. Tie lines indicate approximate values for alloys of respective materials. Adapted from [1]..... 19
Figure 1-2. Schematic illustration of the phenomenon of modulation doping utilized in the operation of HEMT devices showing how a 2DEG is formed in the potential well formed at the interface of two materials of differing band gap energies 22
Figure 1-3. Schematic illustration of a nanoribbon structured InAlN/GaN HEMT device..... 24
Figure 1-4. (a) Schematic illustration of core-shell nanowires on a substrate with (b) diagrams of longitudinal and vertical cross sections. 25
Figure 2-1. Schematic representation of various signals generated when irradiated by an electron beam. 28
Figure 2-2. Schematic illustration of some of the more important elements of an SEM including lens and detectors 31
Figure 2-3. Schematic illustration of a TEM operating in (a) traditional TEM mode and (b) scanning TEM (STEM) mode with important elements labeled for each. 33
Figure 2-4. Diffraction of a plane wave by an ordered array of scattering centers creating multiple wavefronts. Adapted from [1]. 34
Figure 2-5. Schematic illustration of the Ewald sphere construction. Black relrods are those that meet the Bragg condition, gray relrods are those intersected by the Ewald sphere with a large s_g, and blank relrods will not appear in the diffraction pattern. The vectors k_i and k_D are the incident wave vector and any arbitrary radius vector, respectively..... 37
Figure 2-6. (a) SAD and (b) CBED patterns from a single crystalline sample of Si along the (1 1 1) zone axis. Adapted from [1]. 38
Figure 2-7. Schematic illustration showing the cone of diffraction resulting from a converged beam of electrons. Parabolas are created at the intersection of the cones with the Ewald sphere and approximate lines in the diffraction plane. 39
Figure 2-8. Plots of dispersion surfaces for (a) $U = 0$ and (b) $U \neq 0$ which opens a gap of disallowed energies. The intersection of the two spheres delineates a plane called the Brillouin Zone Boundary..... 41
Figure 2-9. Illustration demonstrating how various strain fields affect HOLZ line patterns 42

Figure 2-10. Schematic illustrating some of the key differences in how (a) CBED and (b) NBED are performed and the resulting diffraction patterns. 43
Figure 2-11. (a) STEM image of a Si-SiGe superlattice with increasing Ge content in each successive layer. (b) FFT image of lattice resolved STEM image in (a). (c) and (d) show respectively the phase and amplitude images obtained from the (1 11) g-vector. STEM image courtesy of Dr. David Cooper. 45
Figure 2-12. Strain maps calculated along the (a) growth and (b) in-plane directions for the Si-SiGe superlattice shown in Figure 3-10(a). (c) A comparative plot of the strain and STEM image contrast across the superlattice layers. 46
Figure 3-1. Schematic illustration of a 2D, 9-node rectangular element (a) and a 3D, 27-node brick element (b) commonly used in the FE analysis of static mechanical problems. 52
Figure 3-2. Analytical calculations of the (a) radial and (b) hoop stresses of a core-shell nanowire heterostructures. 57
Figure 3-3. (a) Geometry and examples of the model meshed using (b) 28, (c) 175, and (d) 700 elements 58
Figure 3-4. Comparison of the analytical and finite element analysis solutions for the (a) radial and (b) hoop stress. 60
Figure 3-5. (a) Effective, (b) radial, and (c) hoop stress band plots for a 2D hexagonal nanowire cross-section. 61
Figure 3-6. Plots of the (a) radial and (b) hoop stress along the two main directions of a hexagonal cross section compared to the stresses calculated for a circular section. 62
Figure 3-7. Semi-log plot of the maximum radial stress calculated for a core-shell nanowire at the heterointerface along the 112 direction as a function of elements in the model. 63
Figure 3-8. Comparison of the radial and hoop stress components along the <110> and <112> directions for 2D and 3D models. 64
Figure 3-9. Graphical illustration of beams strongly excited (black ellipses) by the Ewald sphere and beams only weakly excited (gray ellipses) 67
Figure 4-1. Sheet resistivity measurements of InAlN/GaN nanoribbon HEMT structures compared to planar structures as a function of Al_2O_3 thickness. Top inset shows a BF-TEM cross-sectional image of some typical ribbon structures [17] 73

Figure 4-2. Schematic illustration of the processes involved in the fabrication of InAlN nanoribbon structures. 74
Figure 4-3. Cross-sectional BF-TEM images of several nanoribbon structures 76
Figure 4-4. HRTEM image of a nanoribbon with a crystallized layer of oxide on top. The boxes number 1 – 3 demark the area of the sample from which the corresponding FFT images are obtained. 77
Figure 4-5. Cross-sectional DF-STEM images of representative (a) planar and (b) nanoribbon structures investigated in this study. 78
Figure 4-6. (a) Experimentally obtained and (b) simulated CBED pattern along the [540] zone axis in GaN with important HOLZ lines labeled 79
Figure 4-7. DF-STEM images of (a) planar and (b) nanoribbon HEMT structures showing the locations where CBED patterns were obtained. (c) and (d) show the evolution of the 117 HOLZ line throughout the series. The colored dots in (a) and (b) denote the onset of HOLZ line splitting as shown in the corresponding panels labeled in (c) and (d) 80
Figure 4-8. (a) Schematic illustration of the free-surface total relaxation assumption and the creation of a bi-crystal for the estimation of HOLZ line broadening shown in (b). 81
Figure 4-9. (a) Comparison of HOLZ line splitting approximations from both experimental series of CBED patterns and FEA calculations of planar and nanoribbon structures. (b) Illustration of the FEA model developed to simulate strain at the InAlN/GaN heterointerface of a nanoribbon structure 82
Figure 4-10. (a) Band plots of the three major strain components along the midplane of the FEA model. (c) Line scans of the strain components shown in (b) showing the variation along a path analogous to the beam direction. 83
Figure 4-11. The average stress (plotted in red) in the InAlN layer is calculated from FEA for device sized structures and is plotted as a function of the thickness of the passivating oxide layer for both planar and nanoribbon structures. Sheet resistance data (plotted in blue) from our previous investigation is replotted for comparison. All lines are used as guides to the eye and emphasize the dramatic decrease in sheet resistance observed for the nanoribbon device at an Al_2O_3 thickness of 45 nm (indicated by arrow). 84
Figure 5-1. HAADF-STEM image of a typical nanoribbon structure studied in this investigation with the important HEMT layers labeled with their nominal compositions. A detail image of the

HEMT layers is shown in the top inset while the bottom inset shows a schematic illustration of multiple nanoribbon structures in cross-section. 89
Figure 5-2. A 5.5 nm probe shown in (a) was used to produce NBED patterns along the [11$\bar{2}$0] zone axis, such as the reference pattern seen in (b). The growth-direction strain profiles obtained from NBED for the nanoribbon HEMT structures seen in the inset are presented in (c)..... 92
Figure 5-3. (a) HAADF STEM image of HEMT structure used to create GPA strain maps. The g-vectors (0002) and (0$\bar{1}$11) are first selected from a FFT image (b). Raw phase and amplitude images are calculated from each vector and shown in (c) – (f). Strain maps are calculated for both the growth direction (g) [0002] and the in-plane direction (h) [0$\bar{1}$10] with the scale shown to the far right..... 96
Figure 5-4. Growth-direction strain maps with spatial resolutions of (a) 5 nm and (b) 2 nm generated from the HAADF STEM image shown in Figure 5-3(a) with the strain scale indicated at the bottom. (c) Linescans are obtained from each image as indicated in (a) and integrated over the whole field of view. 97
Figure 5-5. (a) Overlay of a GPA strain map on a lattice resolved STEM image.(b) A magnified portion of the HEMT region indicated by the box in (a) showing the measured strain values in percent at those locations. 98
Figure 5-6. A summary of strain profiles generated using GPA, NBED, and FEA simulations for both the (a) nominal and (b) calculated chemistries. The inset shows a scaled cross section of the HEMT structure. 100
Figure 5-7. Summary of EDX linescan data obtained from the HEMT structure showing (a) the intensity profiles for Ga, Al, and In. The quantified results throughout the barrier and spacer layers are shown in (b). 101
Figure 6-1. Schematic illustration of steps of core-shell nanowire growth consisting of (a) deposition of Au nanoparticles, (b) nanowire nucleation, (c) nanowire growth, (d) shell deposition, (e) resulting final structure. 105
Figure 6-2. SEM images of GaAs/GaAsP core-shell nanowires. (a) was obtained at a 45° to the surface normal while (b) shows a top down view of the sample. 107
Figure 6-3. (a) ADF-STEM image of a typical GaAs/GaAsP core-shell nanowire cross-section. (b – c) EDS maps of Ga, As, and P signals..... 108

Figure 6-4. Representative images of the (a) [556] and (b) [677] zone axes identified in GaAs near the [111] zone axis and shown to be suitable zone axes for CBED study. 110
Figure 6-5. (a) ADF-STEM image of GaAs/GaAsP nanowire cross section showing approximate locations where CBED patterns were obtained. (b) Typical CBED pattern obtained along the [556] zone axis in GaAs/GaAsP core-shell nanowire with two pairs of prominent lines labeled – the {$\overline{6}$42} and {5$\overline{1}\,\overline{3}$} lines. 111
Figure 6-6. (a) DF-STEM image of GaAs/GaAsP core-shell nanowire with arrows indicating the locations where CBED patterns were obtained. (b) The evolution of the ($\overline{6}$42) HOLZ line is shown with images on the left being obtained from the center of the nanowire cross-section and those on the right at the corner and facet surface. 112
Figure 6-7. Comparison of CBED patterns obtained from (a) a GaAs/GaAsP core-shell nanowire and (b) a InAlN/GaN HEMT structure showing examples of non-symmetric and symmetric HOLZ line splitting respectively. 113
Figure 6-8. Plots of the {4$\overline{6}$2}/{5$\overline{1}\,\overline{3}$} tie line length versus distance from the facet surface for Facets 1 – 4. Dotted lines are a guide to the eye only and shading shows approximate transition between core and shell. 115
Figure 6-9. Examples of the geometries used in the FEA analysis of GaAs/GaAsP core-shell nanowires showing both whole and half sections. 117
Figure 6-10. Examples of strain data extracted from FEA model. Plots showing the average (a) normal strains and (b) shear strains for through-thickness lines at specified distances from the nanowire center. 119
Figure 6-11. Comparison of a typical (a) simulated and (b) experimental CBED pattern with significant lines labeled. 120
Figure 6-12. HOLZ line shift profiles from series of simulated CBED patterns based on initial FEA investigation of half-hexagonal, core-shell heterostructures. Dotted lines are guides to the eye only. 121
Figure 6-13. Band plots of the (a) – (c) normal and (d) – (e) shear strain components calculated for a core-shell nanowire heterostructures surrounded by a carbon coating 123
Figure 6-14. Band plots of the (a) radial, (b) hoop, (c) axial, and (e – f) shear components of strain for a core-shell nanowire surrounded by an amorphous carbon coating. 124

Figure 6-15. Comparison of second-iteration simulated HOLZ line shift plots (black dots) to experimental HOLZ line shift data (colored markers) for some facets. 125
Figure 6-16. Band plots of (a) – (c) normal and (d) – (f) shear strain components of a core-shell nanowire heterostructures with a circular core. 127

List of Tables

Table 3-1. Materials parameters for GaN and AlN used in analytical and FEA solutions..... 55
Table 3-2. Relevant materials properties used in analytical and FEA solutions 57
Table 4-1. Summary of elastic constants used in FEA simulations of planar and nanoribbon HEMT structures..... 82
Table 5-1. Summary of strain characterization techniques used in this investigation highlighting their various strengths and weaknesses..... 102
Table 6-1. Elastic constants and pseudo-coefficients of thermal expansion for materials used in FEA models. 118

List of Abbreviations

CBED	Convergent beam electron diffraction
ADF	Annular dark field
BF	Bright field
CL	Cathodoluminescence
EDS	Energy dispersive X-ray spectroscopy
FEA	Finite element analysis
FIB	Focused ion beam
FWHM	Full-width at half maximum
GBP	Generalized Bethe potential
GPA	Geometric phase analysis
HAADF	High angle annular dark field
HEMT	High electron mobility transistor
HRTEM	High resolution transmission electron microscopy
MOCVD	Metal-organic chemical vapor deposition
NBED	Nanobeam electron diffraction
RIE	Reactive ion etching
SAD	Selective area diffraction
SEM	Scanning electron microscopy
STEM	Scanning transmission electron microscopy
TEM	Transmission electron microscopy
TMAl	Tri-methyl aluminum
TMGa	Tri-methyl gallium
VLS	Vapor-liquid-solid
VS	Vapor-solid

Chapter 1. Introduction

III-V compound semiconducting materials have become an important materials platform due to their excellent intrinsic properties including high electronic carrier mobilities, direct energy band gaps, and band gap energies that span a wide range of values covering the entirety of the visible spectrum. These properties have allowed compound semiconductors to outperform and replace silicon – the material of choice for the electronics industry since its inception – in certain application spaces such as photonics, where silicon performance is limited by its basic materials properties. These materials, however, are typically more expensive and difficult to fabricate. There is therefore a strong need to integrate III-V materials into existing silicon technologies, thereby creating devices with advanced functionality at low cost. However, defects that arise at the interface between lattice mismatched materials (silicon and III-V materials in this case) are a major obstacle in reaching this goal. While techniques such as the fabrication of graded buffer layers offer solutions to mitigate the formation of strain-related defects such as threading dislocations, challenges still exist in the form of thermal expansion differences and control of material polarity. Alternatively, nanostructured materials offer a unique platform for the direct integration of defect free III-V materials on Si and other substrates of interest. This promise stems, in part, from a nanostructure's inherently large surface area-to-volume ratio which allows for the efficient relaxation of stress without the formation of defects. In practice, this means that the critical thickness of a misfit layer is increased in a nanostructured architecture, such as a core-shell nanowire, compared to that observed for thin film structure allowing for not only thicker layers but also layers of materials with higher values of mismatch.

Furthermore, novel structures can be realized on these nanostructured platforms that would otherwise be infeasible in a thin-film geometry due to high levels of stress creating new opportunities to take fuller advantage of the wide range of materials properties. Figure 1-1 plots various compound semiconducting materials according to their band gap energies and their lattice constant [2]. As this map shows, not only do these materials cover a wide range of band gap energies – extending from InSb at 0.17 eV to AlN at 6.2 eV – but they also cover a wide range of lattice parameters which is the source of misfit stress. As it has been said, this misfit stress poses great challenges in the design of III-V based devices, but it also presents a great opportunity for the fine tuning of materials properties through strain engineering. To fully take

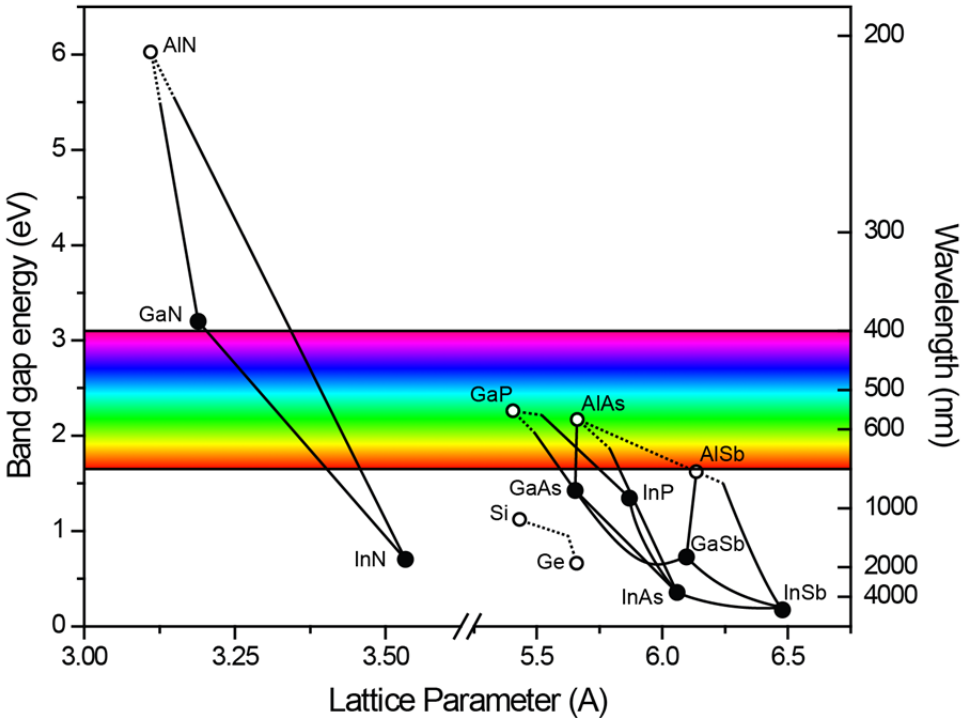

Figure 1-1. Common III-V materials plotted by their energy band gap and lattice parameter. Tie lines indicate approximate values for alloys of respective materials. Adapted from [1].

advantage of this opportunity, however, one must be able to fully characterize the stress and strain fields within an individual nanostructure with nanoscale spatial resolution. Due to their inherent small size, however, characterization by standard bulk techniques such as X-ray diffraction (XRD) and Raman spectroscopy are difficult and only provide average values. In this thesis investigation, we will show how the combination of advanced electron microscopy techniques and simulations methods can provide a quantitative understanding of the stress and strain fields of individual nanostructures on the nanoscale. This new understanding and toolset for characterization will prove vital for the future development of advanced opto-electronic devices based on III-V semiconducting nanostructures.

1.1. Strain engineering in semiconducting nanostructures

The performance of an electronic device is, in large part, dictated by its materials properties such as electronic band gap, carrier mobilities, etc. However, as the demands for better, faster, and more efficient devices increase, these same materials properties often put constraints on what can be achieved. Therefore, strategies must be developed to push beyond these materials limits and enable the fabrication of next generation devices.

One such strategy is strain engineering. The effects of strain on the band structure of semiconducting materials have been studied for some time; however, the first devices to make use of these effects did not begin to appear until the late 1980's and early 1990's. Work like that of Jorke and Herzog provided experimental evidence of the splitting of the six-fold degenerate conduction bands in silicon [3] while Welser *et. al* were among the first to demonstrate a strain enhanced silicon n-MOSFET device [4, 5]. Since then, strain enhancement has become a crucial component of device design and fabrication. As modern devices continue to scale to smaller and smaller length scales, however, the ability to reliably create strain becomes more difficult as edge relaxation effects become a key consideration. Therefore, it is important to identify novel architectures that will enable the reliable application of strain to enhance device performance.

Nanostructured materials fabricated through both top-down processes (e.g. lithography, etching, etc.) and bottom-up processes (e.g. free standing nanowires) offer a promising platform for the design of novel strain engineered devices. Because nanostructures are not confined in 2D like thin-films are, strain can be imposed on the material in variety of ways. This flexibility of design has allowed for the realization of nanostructures with enhanced mobilities [6, 7], tunable bandgaps [8, 9], and materials combinations not achievable in a thin film geometry [10, 11]. Because of their direct bandgap energies, the use of strain to tune the luminescent properties of III-V materials is an important and widely researched phenomenon. For example, Sköld *et al.* demonstrated that by varying the composition, x, of a $GaIn_{1-x}P_x$ shell on a GaAs nanowire, the band gap could be tuned over a range of 240 meV [8]. Other studies achieved similar results with GaAs/AlGaAs/GaAs nanowires using a uniaxial stress applied mechanically [9]. The great opportunities of utilizing nanostructures efficient strain relaxation have been demonstrated in the fabrication of InGaN shells with In concentrations greater than 40%at on GaN nanowires [11]. This result is even more significant when we consider the difficulty of fabricating planar films of InGaN on a GaN substrate. Films containing over 20%at In are known to suffer from phase segregation, plastic relaxation, and polycrystallization [12]. While powerfully illustrating the great opportunities nanostructures provide, many of these studies also demonstrate the need to better understand and characterize the stress and strain fields of individual structures. Variations in strain across a structure could have significant ramifications on device fabrication and operation[11] making it important to develop tools and techniques that can accurately measure strain with nanoscale spatial resolution.

1.2. Characterization of strain in bulk and nanostructured semiconductors

As device structures become smaller and the use of nanostructured materials increases, many of the assumptions that are used for a 2D strain calculation are no longer valid making the characterization of strain on the nanoscale vital for the continued development of strain enhanced devices. Additionally, most of the techniques used to quantify strain in bulk systems do not have the spatial resolution needed to probe strain fields in individual structures. Two of the most commonly used techniques for strain characterization in bulk semiconductors are XRD and Raman spectroscopy. XRD takes advantage of the short wavelength of X-rays that allows for interaction with the crystalline lattice and the formation of diffraction patterns. Because diffraction will be dependent on the crystalline lattice spacing (see Chapter 2 for a more detailed discussion), an analysis of the diffraction peak position can yield information about stress in a material. However, X-ray beams are difficult to focus to small spot sizes and even nanobeam X-ray diffraction can only achieve spatial resolutions on the order of ~100 nm. μ-Raman spectroscopy uses a focused laser to excite optical phonon modes in a material. By observing the shift in the resonance of those phonon peaks, the strain in a material can be determined. However, like XRD, the spot sizes achievable in μ-Raman are typically on the order of 1 μm – larger than an individual nanostructure. Despite this resolution limit, many studies of stress and strain in core-shell nanostructures using these techniques do exist, though only average stress values from ensembles of nanostructures can be retrieved [10, 13-16]. One method of characterization common throughout most of these studies, however, is the use of mechanical models; and, while some of these models predict an inhomogeneous nature of strain in the structure [13, 14, 17], to our knowledge there exists no experimental evidence directly demonstrating this behavior.

Electron microscopy comprises a number of analytical techniques that are well suited to the nanoscale characterization of many aspects of a material including structure, chemical composition, and morphology. In Chapter 2 we will discuss EM techniques that will allow for the nanoscale scale quantification of strain in individual nanostructures with spatial resolutions on the order of 1 nm and subsequently show that these results can be directly compared to mechanical models of the system. We will demonstrate these techniques in two types of semiconducting nanostructures which represent both two key materials systems (GaN and GaAs

based materials) and two prominent nano-fabrication methods (electron-beam lithography and particle-mediated nanowire growth).

1.3. Materials systems of interest

Two important materials systems that have already proved to be promising platforms for future electronic and optical devices will be the focus of this investigation of stress and strain fields in III-V nanostructured heterointerfaces. In this section these systems will be discussed with an emphasis on the role of stress and strain in device operation and the need for nanoscale studies.

1.3.1. InAlN/GaN nanoribbon HEMTs

High electron mobility transistors (HEMTs) are an important device structure for the realization of high-frequency and high power applications. HEMTs operate based on the phenomenon of modulation doping illustrated in Figure 1-2. When two materials of differing band gap energies are joined together, extreme bending of the conduction and valence bands occurs at the interface of the two materials. By choosing the proper materials, this band bending can be used to create a potential well below the Fermi energy, E_F, at the interface which will trap electrons creating a two-dimensional electron gas (2DEG). Because the electrons in the 2DEG are spatially separated from charged scattering centers in the bulk of the material their mobility will be enhanced, improving device performance.

The AlGaN/GaN system has been a standard choice for the fabrication of GaN-based HEMT devices due to the material's high band gap, high break down voltage, high carrier

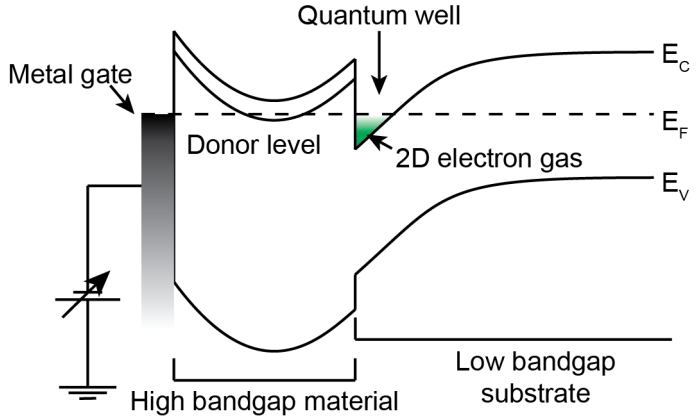

Figure 1-2. Schematic illustration of the phenomenon of modulation doping utilized in the operation of HEMT devices showing how a 2DEG is formed in the potential well formed at the interface of two materials of differing band gap energies

mobilities, and thermal stability [18]. Because the concentration of the 2D-electron gas created at the heterointerface is heavily dependent on a piezoelectric effect resulting from the lattice difference between the AlGaN and GaN, the concentration of carriers increases with increasing Al content; however, increasing Al content inevitably leads to higher stress at the heterointerface. The performance of AlGaN/GaN based devices is therefore a careful balance between the desire to have a high carrier concentration and minimizing strain related defects [19]. Relaxation of strain over time can also lead to problems in device reliability [18].

It was proposed by Kuzmík that InAlN may be used instead of AlGaN due to the ability to grow an alloy consisting of $In_{0.17}Al_{0.83}N$ lattice-matched to GaN [20]. He showed that by using InAlN instead of AlGaN, current densities could be increased by 105% due to the high spontaneous polarization of InAlN while retaining many of the same intrinsic properties, such as a high band gap, that make AlGaN attractive. Consequently, high concentration 2D gasses could be fabricated while avoiding the reliability and other defect issues related to the strain in AlGaN/GaN systems. However, strain is still an important consideration in this materials system. Kuzmík also showed that by varying the composition of the InAlN film, a compressive or tensile strain could be induced in the active layers of the HEMT device [21]. Since InAlN is also piezoelectric, the introduction of strain will allow the carrier concentration to be changed. Kuzmík predicted that an optimal HEMT structure could be achieved by fabricating a tensile strained InAlN material. Others have also pointed out that compressively strained InAlN/GaN devices could be useful for the preparation of enhancement mode GaN-based devices [22].

In addition to chemical tuning, the fabrication of nanostructures could be a viable route towards engineering strain in this system. In their attempts to mitigate short channel effects through carrier confinement in highly scaled AlGaN/GaN HEMT devices, Azize *et al.* discovered that the fabrication of nanoribbon structures allowed for relaxation in the plane of the device, degrading its electrical performance [23]. In order to maintain the biaxial strain state of the original planar film, thin films of Si_xN_y were deposited on top of the nanoribbon structures which restored the performance. This method of nanoribbon-enhanced HEMT devices was then applied to the InAlN system (shown schematically in Figure 1-3) as a means to not only confine carriers spatially, but also as a new means of strain engineering the material [24]. Electrical measurements showed that fabricating nanoribbons creates an increase in sheet resistivity as would be expected due to the removal of material. However, it was also observed that deposition

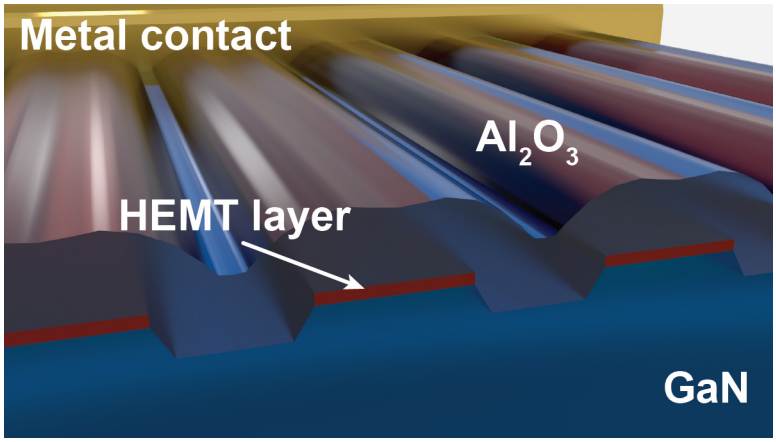

Figure 1-3. Schematic illustration of a nanoribbon structured InAlN/GaN HEMT device

of a passivating layer of Al_2O_3 could decrease the sheet resistivity. More surprising was the observation that the sheet resistivity was dependent on the thickness of the oxide film and can decrease the sheet resistance below that of the planar device when the nanoribbons were completely buried. These results would suggest that there is some stress that is relieved in the film during the creation of the nanoribbons and subsequently confined with the oxide deposition. However, little is known about the origin of stress in this system and the role of the passivating layer, warranting a more rigorous investigation on the nano-scale.

1.3.2. III-arsenide core-shell nanowire heterostructures

In addition to nanoribbons fabricated from planar heterostructures, this investigation will study stress and strain in free standing nanowires. III-V semiconducting nanowires are an interesting and important class of materials as they provide a novel platform for the fabrication of optical and electronic devices due to their superior intrinsic properties with the promise of integration onto a number of substrates – such as silicon [25], or flexible substrates [26]. Core-shell nanowires, illustrated schematically in Figure 1-4, are of particular importance as the addition of a shell not only passivates surface states that can lead to quenching of carriers [8] but also provides a means of band engineering. This opens up the door for modulation doping making them attractive structures for the fabrication of lasers [27], LEDs [28], and high mobility electronics [29]. Furthermore, the wrap-around heterointerface in a core-shell nanowire presents a unique extension of the planar interface leading to novel behavior of the strain fields. Therefore, in order to fully utilize the outstanding properties of these structures, it will be essential to fully characterize the strain created by the deposition of a shell.

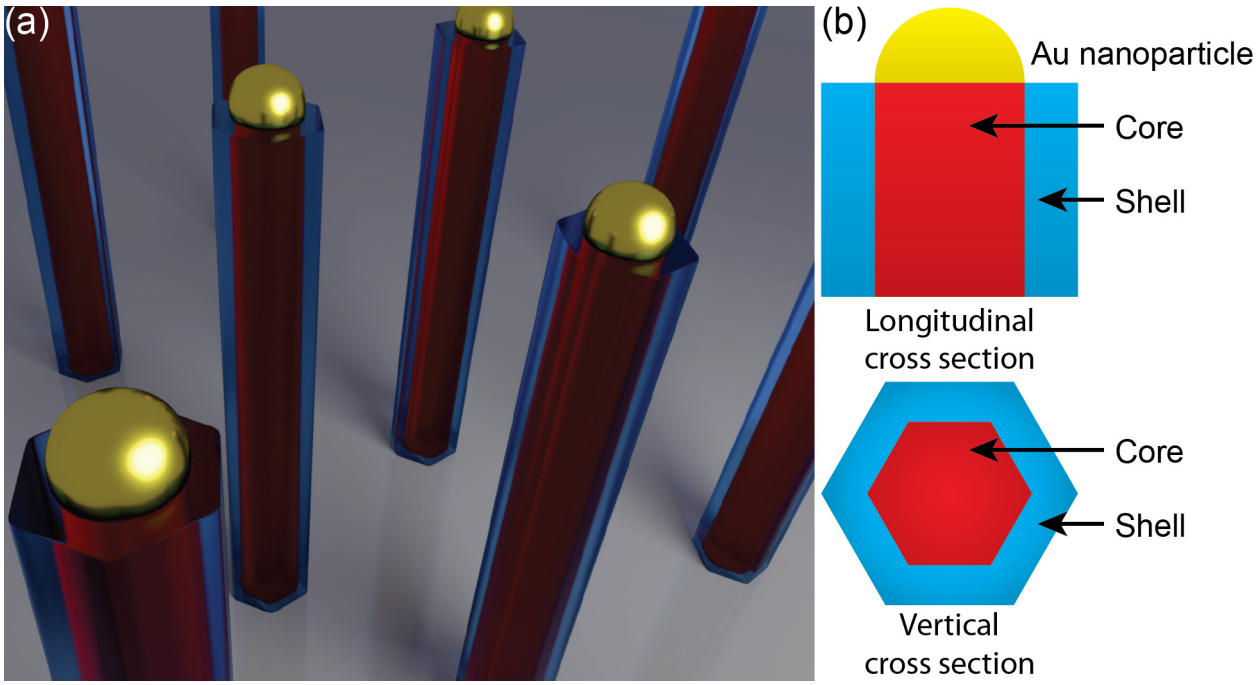

Figure 1-4. (a) Schematic illustration of core-shell nanowires on a substrate with (b) diagrams of longitudinal and vertical cross sections.

GaAs nanowires are of significant interest due to the high mobilities achievable [30]. Additionally, a number of different shell materials can be deposited on a GaAs nanowire core depending on the desired application. AlGaAs has been shown to form defect free shells [29] on GaAs cores that allow for the creation of modulation doping and enhanced carrier mobility [31]. Other shell materials like GaP [10] and InGaP [8] have also been studied and shown to introduce a strain that alters typical GaAs nanowire behavior. This study will focus on the use of GaAsP as a shell material. Not only has GaAsP been shown to be an adequate material for the passivation of surface states [27, 32]; but, with a maximum misfit of 3% GaAs, GaAsP also offers a large range of strain that can be engineered in the system by tuning the composition of the shell. This flexibility could allow for the design of advanced structures such as multi-shell superlattices of varying composition where each shell is tuned to emit at a different energy. However, such rational design will require that the stress and strain in each layer be quantified; and, as it has just been discussed, the current standard techniques for strain characterization do not possess the spatial resolution necessary for such an investigation.

1.4. Thesis outline

Having introduced the materials systems of interest and the motivation for a nanoscale investigation of stress and strain in this chapter, the remainder of this thesis is organized in the following manner.

Chapter 2 introduces and discusses the theory and practice of electron microscopy including scanning electron microscopy (SEM) and transmission electron microscopy (TEM). These tools along with the related techniques of convergent beam electron diffraction (CBED), nanobeam electron diffraction (NBED), and geometric phase analysis (GPA) will form the basis of our experimental investigation and will therefore be discussed in detail.

While Chapter 2 will focus on experimental techniques, Chapter 3 will examine the computational and modeling approaches used to supplement and help interpret the experimental data. Strain fields are calculated using the finite element analysis (FEA) of mechanically static models while Bloch wave calculations provide a bridge between calculated strain fields and experimental electron diffraction patterns. As it will be shown in Chapters 4 through 6, the modeling of strain fields and subsequent comparison to the experimental data is essential in forming a quantitative understanding of the stress created at the heterointerface in a nanostructure.

In Chapter 4, we will investigate how the fabrication of nanoribbons can allow for strain engineering of InAlN/GaN HEMT structures. CBED is used to locally probe the stress state of individual nanoribbons and demonstrate large variations in strain along the growth direction. An appropriate FEA model is developed based on the experimental results and used to demonstrate the ability of a passivation layer to impart stress in the plane of the HEMT structure providing novel routes for strain engineering and control of carrier concentration in the active layers of the device.

Chapter 5 will continue our investigation of stress and strain in the InAlN/GaN nanoribbon HEMTs with a focus on developing more facile methods of strain quantification and mapping in individual nanostructures. To this end, NBED and GPA are employed and shown to provide highly sensitive strain information with spatial resolutions of only a few nanometers. This new data is used to refine the FEA model developed in Chapter 4 which in turn provides

new insights into possible effects that high temperature device fabrication processes have on the final structure.

In Chapter 6, we will turn our attention to the strain characterization of GaAs/GaAsP core-shell nanowire heterostructures. These bottom-up fabricated nanostructures not only provide a unique platform for the fabrication of highly mismatched heterostructures but also extend the idea of a heterointerface to the 3D geometry of the core-shell interface. In this chapter we demonstrate how the tracking of higher order Laue zone lines in CBED patterns can provide strain information with spatial resolutions of 1 nm. Furthermore, the use of Bloch wave simulations of CBED patterns based on the strain field calculations from FEA provide a powerful picture of how the combination of experimental and theoretical calculations create a more robust picture and understanding of the system.

Finally, in Chapter 7 we will summarize the important scientific contributions of this work and briefly discuss future directions of work in this field based on the results presented here.

Chapter 2: Experimental methods – Electron microscopy

As discussed in Chapter 1, the ability to quantify strain in individual nanostructures with high spatial resolution will be vital in the optimization of advanced devices providing new insights into fabrication and operation. The ability to obtain chemical, topological, and strain information at high spatial resolution makes electron microscopy an ideal platform for the nanoscale characterization of materials. This chapter will discuss some of the fundamental operating principles of both scanning electron microscopy (SEM) and transmission electron microscopy (TEM) with a particular focus on diffraction, image formation, and X-ray spectroscopy.

2.1. Electron-material interaction

Electron microscopy's great strength comes from its ability to combine a number of different techniques that can yield a wealth of information about a sample (crystallinity, chemical composition, electronic band structure information, stress/strain states, etc.) at high spatial resolutions. For this reason, it has become a standard tool for nanoscale characterization. The great versatility of electron microscopy is directly due to the instrument's use of high energy electrons – typically ranging from 1 to 1000 keV – to probe materials. As the high energy electrons hit the sample, they interact with the material creating a number of signals composed of

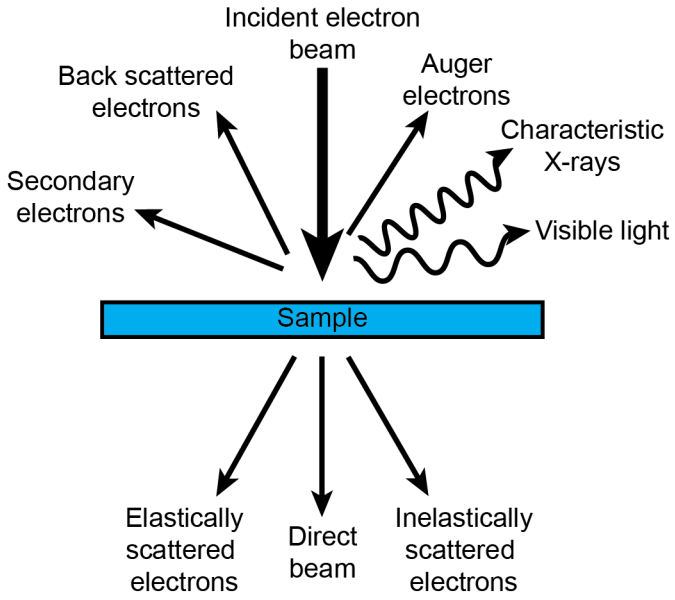

Figure 2-1. Schematic representation of various signals generated when irradiated by an electron beam.

electrons, X-rays, and visible light, as illustrated in Figure 2-1. Throughout this discussion of electron microscopy we will show how each of these signals is used to analyze the physical, chemical, or electronic structure of the sample.

Electron microscopy was first conceived as a means of overcoming the resolution limits of traditional light microscopy. The imaging resolution (δ) of traditional light microscopy can be approximated by the well-known Rayleigh criterion given by

$$\delta = \frac{0.61\lambda}{\mu \sin\beta} \qquad (2\text{-}1)$$

where λ is the wavelength of the incident light, μ is the index of refraction of the imaging media, and β is the semi-angle of collection of the magnifying lens. Using appropriate values, it can be shown that the best resolution achievable using visible light is on the order of 300 nm, well above the limits required for nanoscale investigation. When we consider what the spatial resolution of an image created using electrons would be, we must first carefully consider what the wavelength of an electron is. Taking into account de Broglie's ideas of wave-particle duality and the relativistic effects of high speed particles, it can be shown that the wavelength of an electron accelerated through a field V is given by

$$\lambda = \frac{h}{\left[2m_0 eV\left(1 + \frac{eV}{2m_0 c^2}\right)\right]^{1/2}} \qquad (2\text{-}2)$$

where e is the charge constant (1.602×10^{-19} C), m_0 is the rest mass of an electron, c is the speed of light, and h is Plank's constant (6.0626×10^{-34} N m s). Using this equation, we can calculate the wavelength of an electron with an energy of 200 keV – typical of TEM – is 2.5 pm. Using this value for λ in Equation 2-1, it is clear that the theoretical resolution limit of electron microscopy is well below what is needed for nanoscale investigation. In fact, the current limitations on resolution in electron microscopy do not depend on the wavelength of the electrons, but on our ability to manipulate and focus those electrons using magnetic optics. In most modern microscopes, the primary defect is a spherical aberration of the electron beam that tends to dominate the resolution limit. It has therefore been shown that the minimum resolution achievable can be estimated by

$$r_{min} \approx 0.91(C_s\lambda^3)^{1/4} \qquad (2\text{-}3)$$

where C_s is the spherical aberration coefficient. Typical values of C_s are on the order 1mm, resulting in a minimum resolution of about 0.5 Å [1]. However, recent advancements in special aberration correcting lens systems over the past decade mean that working resolutions as low as 50pm are achievable [33].

Electron microscopy techniques can be broadly categorized into two categories based on the type of microscope used to perform the analysis – either a scanning electron microscope or a transmission electron microscope. Even those techniques that can be performed in either mode, such as energy dispersive X-ray spectroscopy (EDS), will have certain advantages and disadvantages of being performed in one way or the other.

2.2. Scanning electron microscopy (SEM)

SEMs have become a common and routine characterization platform for a wide variety of materials due to their versatility and accessibility. SEMs operate by forming a converged electron probe that is, as its name implies, scanned across the surface of the sample. Because SEMs are generally operated at electron energies between 1 and 40 keV, the main signals observed will be those that are generated near the surface of the sample including secondary electrons, backscattered electrons, Auger electrons, X-rays, and visible light. By varying the energy of the electrons, the penetration depth of the electron beam can be varied allowing for some degree of depth resolved characterization [34, 35].

Figure 2-2 illustrates some of the key parts of an SEM. Electrons are first generated from a source through either field emission or thermal generation and accelerated by an anode. The electrons then pass through the condenser optics that help to shape and form the beam. The objective aperture is then used to select the size of the beam changing the total current. In general, high beam currents will reduce statistical noise in an image but will also reduce spatial resolution. The objective lens then acts to form a probe of approximately 1 – 10 nm in diameter. Finally the scan coils allow the beam to be rastered over the surface of the sample. Generated electron signals are collected by either the secondary electron (or Everhart-Thornley) detector which consists of a Faraday cage and photomultiplier tube or backscatter detector which is generally a solid state detector consisting of four quadrants.

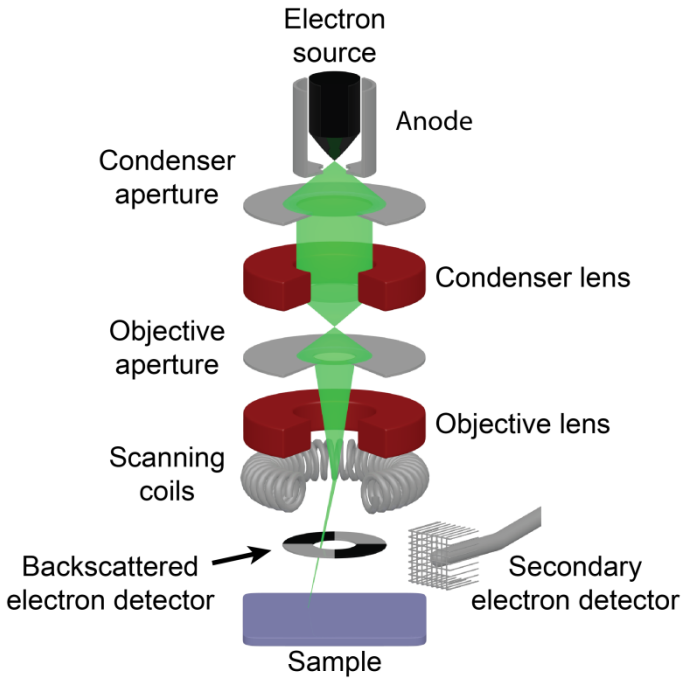

Figure 2-2. Schematic illustration of some of the more important elements of an SEM including lens and detectors

2.2.1. Surface characterization and contrast mechanisms

SEM is most commonly used for the imaging of surface structure. By using a relatively low energy beam (1 – 5 keV) spatial resolutions of 1 nm are readily achieved in a modern machine. When the electron beam is rastered across the surface of the sample, the high energy electrons in the beam interact with the sample and scatter. During this scattering process, the incident electron either retains its energy (elastic) or loses some energy to the material (inelastic). Some of the energy that is lost during an inelastic scattering event then forms secondary electrons (SE) from those weakly-bound outer shell electrons in the material. Using a positively biased Faraday cage, the low-energy (< 50 eV) electrons can be collected to form an image by correlating the intensity of the SE signal and the position of the scanning electron beam. Because of their low energy, only those electrons near the sample surface escape the sample to be collected. Therefore the geometry of the surface relative to the beam incidence has a significant impact on the total signal collected making this mode of imaging especially useful for topological investigation.

Some of the energy lost in inelastic scattering is also used in the formation of X-rays. These signals are useful for the characterization of chemical composition; however, since SEM was

only used for structural investigation in this study, discussion of these techniques will be reserved for later in this chapter and will be discussed in the context of TEM characterization.

Alternatively if the electron undergoes enough elastic scattering events, it can change its trajectory enough to return to the surface and be emitted as a backscattered electron (BSE). Because the process of scattering is dependent on the atomic number of the scattering atom, materials with a higher atomic number (Z) will generate more BSEs [36]. This sensitivity to Z number will highlight changes in chemical composition across a sample. After exiting the surface of the sample, the electrons will impinge on a solid state detector located directly above the sample. By analyzing and combining the signals from the four quadrants of the BSE detector, the image can be tuned to highlight either chemical information or topographical information.

As useful as SEM analysis is, it still cannot provide the nanoscale information needed to quantify stress and strain states in a nanostructure. Even though SEM techniques such as electron backscatter diffraction have been shown able to provide stress information with spatial resolutions on the order of 10 nm [37], we will shortly see that TEM provides an extremely powerful platform for strain characterization with atomic resolution.

2.3. Transmission electron microscopy (TEM)

Unlike SEM, TEM is mostly concerned with those electrons that pass through the sample. Like in SEM, electrons scatter either elastically (diffraction) or inelastically as they travel through the sample. Elastically scattered electrons will be important in characterizing local lattice strains while inelastically scattered electrons will allow us to determine chemical composition. TEMs also operate and much higher accelerating voltages – anywhere from 80 keV to 1 MeV – compared to typical SEMs. These high energies coupled with thin samples (~100 nm), reduce total interaction with the sample greatly increasing spatial resolution over SEM.

Figure 2-3 illustrates some of the key components of a TEM operating in either traditional TEM mode or scanning TEM (STEM) mode. A key difference between these modes is how the sample is illuminated. In TEM mode, a large portion of the sample is illuminated by a parallel beam of electrons. As the electrons pass through the sample, many diffracted beams of electrons are created. Using the objective lens and aperture, some or all of these diffracted beams can blocked from the final image created by the intermediate and projector lenses. In this way, different kinds

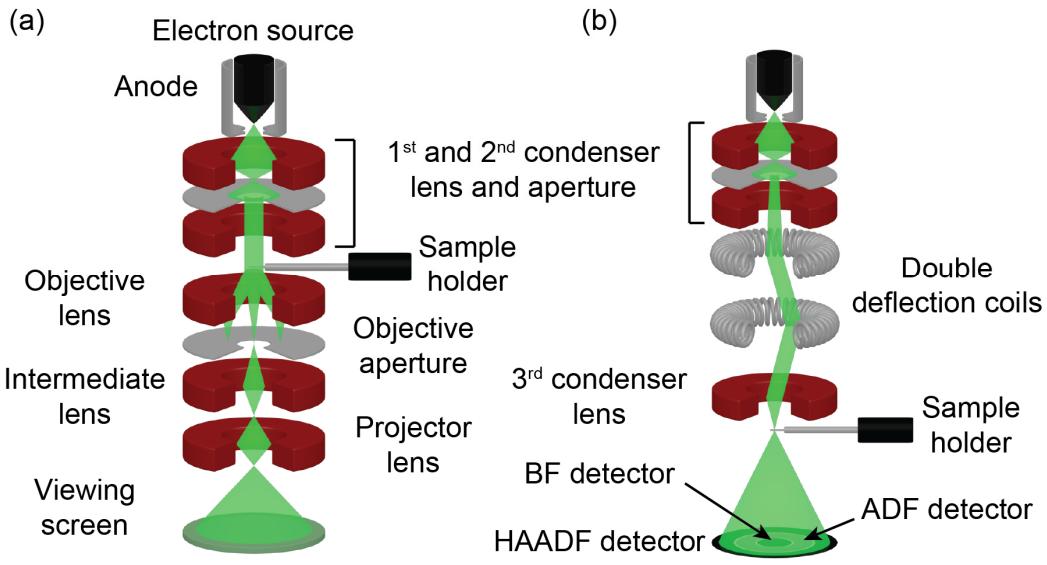

Figure 2-3. Schematic illustration of a TEM operating in (a) traditional TEM mode and (b) scanning TEM (STEM) mode with important elements labeled for each.

of information can be obtained from the sample, as will be discussed in more detail later. In STEM mode, the electron beam is focused to a small probe that is rastered across the surface of the sample much like as in a SEM. However, the signal of interest in STEM are those electrons that pass through the sample. Located below the sample are three detectors – a bright field (BF) detector, an annular dark field (ADF) detector, and a high-angle annular dark field (HAADF) detector. Using these three detectors, different signals can be detected from electrons that scatter at different angles. In general, elastically scattered electrons will scatter to small angles (on the order of 10mrad) while inelastically scattered electrons will be scattered to much higher angles (>50mrad). Therefore, while the BF detector mostly collects elastically scattered electrons, the HAADF detector exclusively collects inelastically scattered electrons. By focusing on differently scattered electrons, different aspects of a sample can be highlighted and characterized, as will be discussed below.

2.3.1. Electron diffraction

Of the various techniques available in a TEM, those most useful for the determination of strain in a nanostructured sample are diffraction techniques. Therefore, it is important to highlight and explain the operating principles behind these techniques to understand the kind of information that can be gathered through their use and what their limitations are. Here we present a short

description of the theory of electron diffraction in materials. For a more detailed discussion, the reader is referred to the excellent text of Williams and Carter [1].

The diffraction of electrons in a TEM is the most important scattering mechanism due to the large amount of information that can be gathered about the positions of atoms in a crystal's lattice. In practice, there are two general diffraction techniques that are predominantly used in a TEM: selected area diffraction (SAD) and convergent beam electron diffraction (CBED). Each of these techniques have their own set of advantages and disadvantages and should be viewed as complementary techniques; however, by comparing these two techniques it will be shown why CBED is a powerful tool for the characterization of nanostructures and strain.

A simple model of diffraction was developed in 1913 by the father and son team Sir William H. and Mr. Lawrence Bragg [38]. In their analysis of diffraction (not physically valid but simple and illustrative) they considered the conditions necessary for two waves to interfere constructively after being reflected off parallel planes of atoms. The resulting conclusion is famously known as Bragg's law and can be written as:

$$n\lambda = 2d \sin \theta_B \qquad (2\text{-}4)$$

where n is an integer, λ is the wavelength of the incident radiation, d is the interplanar spacing, and θ_B is the Bragg angle. While this relationship was formulated with X-ray diffraction in mind, it is still applicable to electron diffraction and helpful for indexing SAD patterns. It also does not treat the problem of determining the intensity of the diffracted intensity. To do this, a more

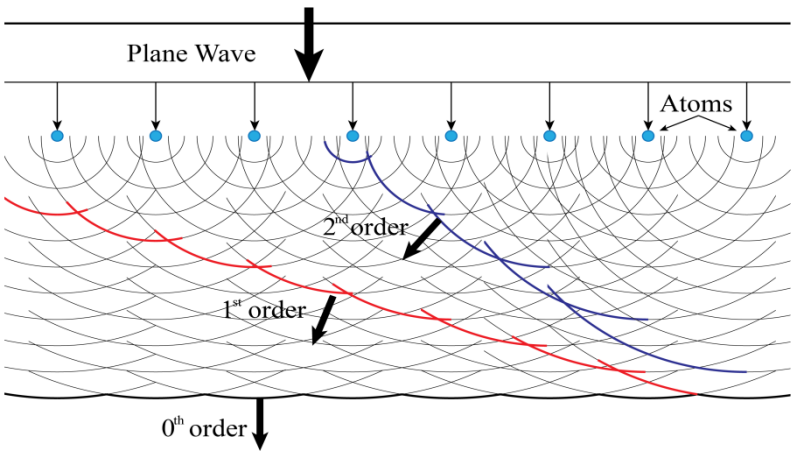

Figure 2-4. Diffraction of a plane wave by an ordered array of scattering centers creating multiple wavefronts. Adapted from [1].

complex model must be considered.

Consider a planar wave of electrons (defocused beam) passing through a crystalline sample. Obstacles in the path of the planar wave act as scattering centers that propagate spherical wavelets. When these obstacle are arranged in a periodic fashion (*i.e.* a crystalline lattice), a series of spherical wavelets are formed that interact with each other to create multiple wave fronts traveling at specific angles (given by Bragg's law) relative to one another. This process for a one-dimensional system is illustrated in Figure 2-4 and shows that there is always one wave front, called the direct beam that travels in the same direction as the incident wave, while other wave fronts traveling at different angles are called the diffracted beams. Using this model, the intensity of different diffracted beams can be calculated by considering the scattering from atoms contained within a unit cell of the crystalline material. By summing the scattering f_i from the individual atoms in a unit cell (with coordinates x_i y_i z_i) and considering an additional phase shift from other atoms on parallel planes with Miller indices (*hkl*) the scattering amplitude from a unit cell $F(\theta)$ can be expressed as:

$$F(\theta) = \sum_{i}^{\infty} f_i e^{2\pi \mathrm{i}(hx_i + ky_i + lz_i)} \qquad (2\text{-}5)$$

Examining this equation – called the structure factor – it can be seen that when applied to various unit cell types (face centered, body centered, etc.), some reflections will have a scattering amplitude of zero. This allows us to formulate selection rules that indicate which planes of a particular crystal structure will create a diffraction event and which will not. These two relationships can now be used to identify experimental diffraction patterns obtained from a sample.

In addition to the structure factor, diffraction from a finite sample will also depend on the shape factor. While the structure factor describes the position of atoms within a unit cell, the shape factor describes the position and arrangement of unit cells in a finite sample. If we consider the diffraction from a finite thin rectangular film of material with dimensions A, B, and C, we can write the diffraction intensity as the summation of the diffraction from each unit cell within the film as:

$$\phi_g = \frac{e^{2\pi i \mathbf{k}.\mathbf{r}}}{r} \sum_n F_g e^{(-2\pi i(\mathbf{g}+\mathbf{s}_g).\mathbf{r}_n)} \quad (2\text{-}6)$$

where r is the propagation distance of the diffracting electrons, **r** is a real-space lattice vector, **k** is the wave vector of the electron in the material, F_g is the structure factor for a unit cell, **g** is a reciprocal-space lattice vector, and $\mathbf{s_g}$ is the excitation error, or deviation parameter. The excitation error is simply a vector quantity that describes how far a reciprocal lattice point is from satisfying the Bragg condition exactly. This parameter will be important to remember in our future discussion of CBED pattern simulation. We will not consider the full derivation of this equation here, but will consider the important result. For a more complete derivation, the reader is referred to any good text on diffraction [1]. Summing Equation 2-6 overall unit cells in the film results in the following equation

$$\phi_g = \frac{e^{2\pi i \mathbf{k}.\mathbf{r}}}{rV_c} F_g \frac{\sin(\pi A u)}{\pi u} \frac{\sin(\pi B v)}{\pi v} \frac{\sin(\pi C w)}{\pi w} e^{iD} \quad (2\text{-}7)$$

where V_c is the volume of a unit cell, D is a phase factor, and (uvw) are the components of the excitation error vector. This equation tells us that the reciprocal lattice points are not delta points, but have some shape defined by the arrangement of unit cells in the finite sample. These shapes have given reciprocal lattice points their more commonly used name relrods.

Additionally, this equation shows that even beams that do not fully satisfy the Bragg condition for diffraction will appear in a diffraction pattern depending on the deviation parameter. A convenient way of visualizing much of the previously described theory is through the use of the Ewald sphere construction shown in Figure 2-5 and first described by Ewald in 1913 [39]. The construction consists of a reciprocal lattice populated by reciprocal lattice points. Each of these lattice points has a shape determined by the shape factor. A circle of radius $1/\lambda$ is then drawn intersecting with the origin of the reciprocal lattice where λ is the wavelength of the incident radiation. Relrods intersected by the Ewald sphere with a small excitation error (black relrods) will be strongly excited while those with a large excitation error (gray relrods) will still appear in the diffraction pattern but with an attenuated intensity. Relrods not intersected by the Ewald sphere will not appear in the diffraction pattern.

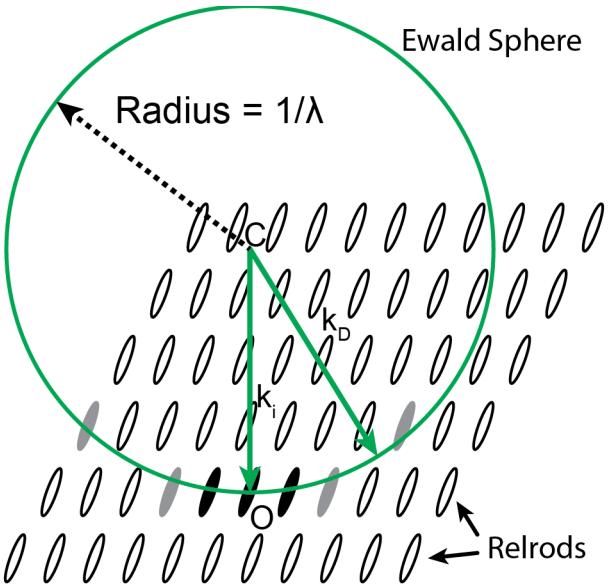

Figure 2-5. Schematic illustration of the Ewald sphere construction. Black relrods are those that meet the Bragg condition, gray relrods are those intersected by the Ewald sphere with a large s_g, and blank relrods will not appear in the diffraction pattern. The vectors k_i and k_D are the incident wave vector and any arbitrary radius vector, respectively.

With this brief look at how SAD patterns are created, experimental diffraction patterns can be analyzed to understand what kind of information can be extracted and what its limitations are. Figure 2-6(a) shows a typical example of a SAD pattern obtained from a single crystalline sample (in this case Si). The bright spot in the center is the direct beam and the surrounding spots are the diffracted beams. Due to the parallel nature of the incident beam, SAD patterns can only provide 2D sample information meaning that only those planes that are parallel to the beam direction will create a diffraction spot. Also, because SAD patterns are formed from a defocused, planar beam of electrons, the region of the sample that generates the pattern is relatively large and depends on the size of the limiting aperture used. In most cases this is around 500 nm and at best 100 nm for microscopes with very low values of spherical aberration. This limitation alone makes characterization of nanostructures difficult. Finally, while structural information such as interplanar spacings can be calculated from a SAD pattern, the error associated with this type of measurement can often be significant: well calibrated SAD patterns will have an error margin of at least 1-2% [1].

2.3.2. Convergent beam electron diffraction and the origin of Higher order Laue zone lines

Having looked at SAD to understand some of the operating principles behind electron diffraction, a complementary diffraction technique will now be considered that can overcome many of the limitations associated with SAD for the analysis of nanostructures. As its name implies, CBED differs from SAD in that the electron beam is focused on the sample. This allows for diffraction from planes that are not parallel to the beam direction creating three-dimensional information in the resultant diffraction pattern. Figure 2-6(b) is a CBED pattern obtained from the same sample that was used to produce the SAD pattern seen in Figure 2-6(a). Comparing the two patterns, several striking differences and similarities can be observed. Like the SAD pattern, the CBED pattern contains bright spots in the same locations as the spots observed in SAD. However, instead of the flat intensity of the SAD pattern, each disc now has a dynamic intensity related to the extra dimensional information achieved by the converged beam. Bright and dark lines, known as Kikuchi lines, also appear both inside and outside of the bright intensity spots. These lines are result of electrons entering the sample in different directions (though mostly forward). Some of these electrons will be traveling at the exact Bragg angle to be diffracted resulting in a cone of diffraction emanating from the plane. When viewed on a screen the resulting parabolic curves will appear linear as illustrated in Figure 2-7. More useful than Kikuchi lines is the similar phenomena of higher order Laue zone (HOLZ) lines. HOLZ lines can

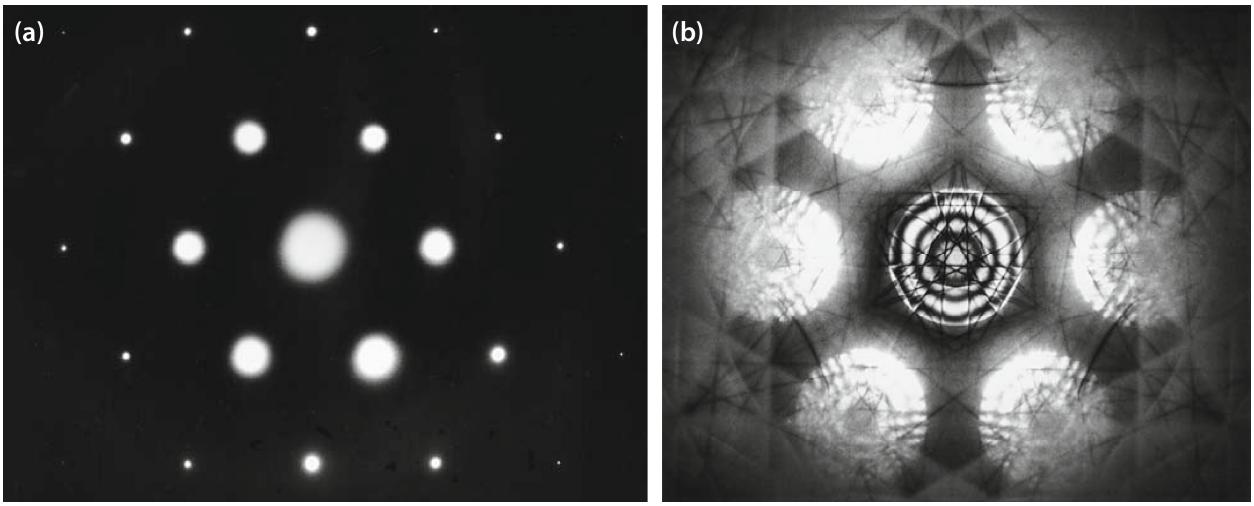

Figure 2-6. (a) SAD and (b) CBED patterns from a single crystalline sample of Si along the (1 1 1) zone axis. Adapted from [1].

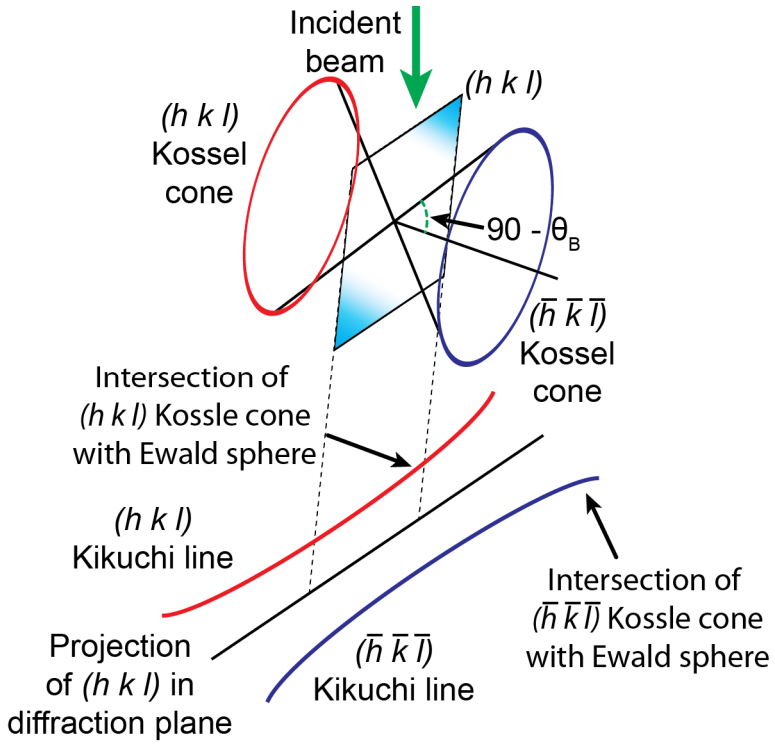

Figure 2-7. Schematic illustration showing the cone of diffraction resulting from a converged beam of electrons. Parabolas are created at the intersection of the cones with the Ewald sphere and approximate lines in the diffraction plane.

be simply defined as the elastic Bragg diffraction of electrons in the direct beam disc to high angles; for a more rigorous understanding, however, a careful consideration of Bloch wave interaction must be considered.

The wave equation of an electron in a periodic potential is described by a Bloch wave equation:

$$\psi^{(j)}(r) = e^{2\pi i \mathbf{k}^{(j)}\cdot\mathbf{r}} \sum_{g} C_g^{(j)} e^{2\pi i \mathbf{g}\cdot\mathbf{r}} \qquad (2\text{-}8)$$

consisting of a plane wave multiplied by a function that contains the periodicity of the crystal potential where j corresponds to the individual Bloch waves in the crystal. Schrödinger's equation can also be written to incorporate the nature of Bloch waves as

$$\nabla^2\psi(r) + \frac{8\pi^2 me}{h^2}\left(E + \frac{h^2}{2me}\sum_{g} U_g e^{2\pi g\cdot r}\right)\psi(r) = 0 \qquad (2\text{-}9)$$

where g is a reciprocal lattice vector, and U_g is a coefficient of the Fourier series describing the periodic potential. Defining a new term K as:

$$K^2 = \frac{2meE}{h^2} + U_0 \qquad (2\text{-}10)$$

and using the definition of a Bloch wave, Equation 2-9 can again be rewritten as:

$$\left\{-\left|k^{(j)} + g\right|^2 + K^2\right\} C_g^{(j)} + \sum_{h \neq 0} U_h C_{g-h}^{(j)} = 0 \qquad (2\text{-}11)$$

This form of Schrödinger's equation is important because it can be used to analyze the interaction of different beams inside the crystal potential. In the simple case of two beams, Equation 2-11 is simplified to

$$\left(\left|k^{(j)}\right| - K\right)\left(\left|k^{(j)} - g\right| - K\right) = \frac{\left|U_g\right|^2}{4K^2} \qquad (2\text{-}12)$$

and is recognized as a dispersion relationship where j can be either 1 or 2. Plotting this equation for the case where $U_g=0$ (in vacuum) results in two intersecting spheres centered at two points separated by a reciprocal lattice vector (O and G) as illustrated in Figure 2-8a. However, in a crystal potential U_g cannot be 0 and creates a separation of energies at the points of intersection, see Figure 2-8b. This creates a gap of energies that are no longer accessible to the electrons as they pass through the lattice and is directly analogous to the electronic band gap. Using this method, it can be seen that the dark deficient HOLZ lines in the (000) diffraction disc are the direct result of the interaction of dispersion surfaces from higher order Laue zones with the zero layer dispersion surfaces. This was first observed by Jones *et al.* [40] who used 85 beams from the zero layer and a few beams of interest in the first order Laue zone to compute the position of deficient lines in the (000) diffraction disc.

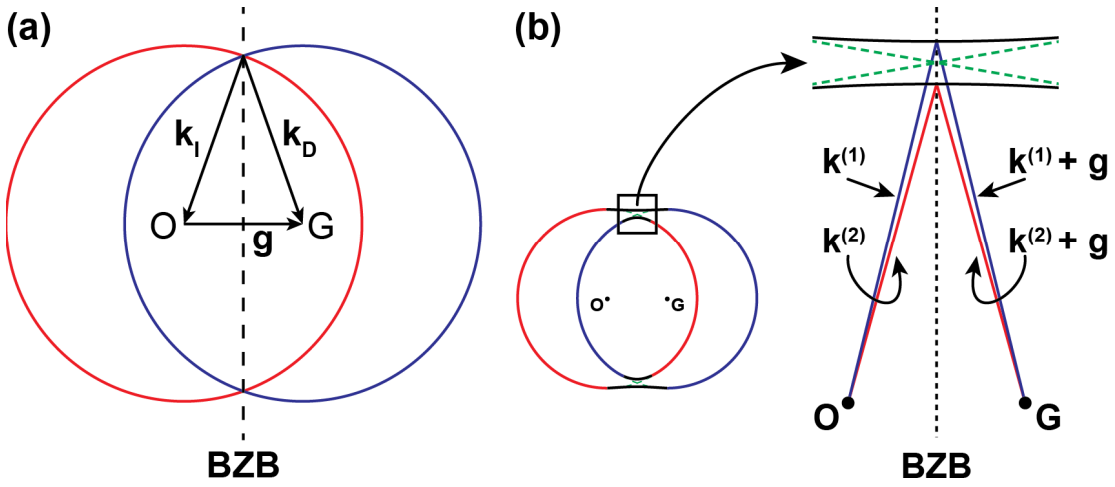

Figure 2-8. Plots of dispersion surfaces for (a) $U = 0$ and (b) $U \neq 0$ which opens a gap of disallowed energies. The intersection of the two spheres delineates a plane called the Brillouin Zone Boundary

Because HOLZ lines result from the diffraction of high order planes (planes highly indexed in *hkl*), their position is highly sensitive to changes in the small interplanar spacings of their respective planes. This high sensitivity has made HOLZ line examination the best method for determining material lattice parameters with accuracy up to 0.02% - two orders of magnitude higher than that achievable with a calibrated SAD pattern. This also makes HOLZ lines useful for determining strain as low as 10^{-4} [41]. The fact that CBED is achieved using a converged beam also greatly enhances the spatial resolution of the technique over SAD with resolutions on the order 1 nm being routine in today's microscopes. The converged beam also allows for integration with other scanning techniques such as scanning TEM (STEM) and energy dispersive X-ray spectroscopy (EDS) streamlining the process of both imaging the sample, collecting diffraction patterns and performing chemical analysis.

2.3.3. HOLZ lines for nanoscale strain measurement

Since strain measurement is a main focus of this work, it is important to understand how HOLZ lines can be used to quantify the stress state in a TEM sample. Figure 2-9 illustrates three types of stress and strain fields that can exist in a typical sample. First, the sample could be unstressed. Secondly, the sample could be uniformly stressed resulting in a uniform strain field throughout the sample. Finally, various regions of the sample could be relaxed (due to a free surface for example) leading to the creation of strain gradients throughout the sample. These two different states of strain will have different effects on the HOLZ line patterns that are obtained from the

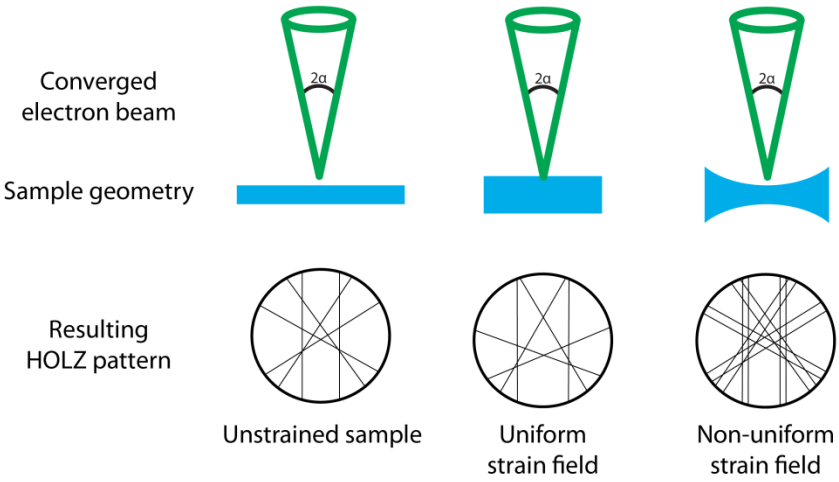

Figure 2-9. Illustration demonstrating how various strain fields affect HOLZ line patterns

respective samples. As it was previously mentioned, HOLZ lines are the result of electrons within the direct beam traveling at the exact Bragg angle to a plane *hkl* and diffracting out to high angles. Remembering Bragg's law (Equation 2-4), it can be seen that if the interplanar spacing is changed due to a uniform strain on the sample, the Bragg angle will change resulting in a shift of the corresponding HOLZ line. Therefore by obtaining a CBED pattern in a strained area and comparing the shift of the HOLZ lines with respect to a pattern taken in an unstrained area, the effective lattice parameter and therefore the strain can be calculated in that region of the sample through a series of kinematic simulations. This approach has been used throughout literature as a means to quantitatively measure strain in appropriate samples [41, 42].

Samples that contain non-uniform strain gradients are not as simple to analyze as they result in a splitting of the HOLZ lines. The splitting is a direct result of the gradient in interplanar spacings observed through the thickness of the sample and the quantity of splitting can be directly related to the severity of the gradient [43]. The splitting of HOLZ lines has been frequently observed, yet has always proved difficult to use for quantitative analysis. More recently, however, advanced simulation techniques have been developed that can accurately reproduce experimentally observed splitting effects when combined with an appropriate mechanical model that provides a displacement field. By comparing experimental HOLZ patterns to simulations, the calculated displacement field can be refined to yield the best fit. Examples and more details of these simulations and other techniques for quantitative data extraction will be considered in the following chapter. It is important to note, however, that both types of HOLZ (shifted and split) line patterns obtained from strained samples require some level

of simulation to obtain quantitative data. Both also require reference patterns that can be used to assess the operating conditions of the microscope as small variances in accelerating voltage can also shift HOLZ lines – though these reference patterns do not need to be obtained from the same material as the area of interest.

Despite the great strength of CBED as a characterization technique, it will also be important to identify techniques that can complement CBED and make up for some of its shortcomings. Because a complete CBED analysis will require a significant amount of simulation, techniques with more straightforward data extraction will be important for samples where high throughput is important. In this study, nanobeam electron diffraction and geometric phase analysis were identified as complementary techniques for strain analysis.

2.3.4. Nanobeam electron diffraction

Nanobeam electron diffraction (NBED) is a TEM based technique that analyzes changes in diffraction patterns obtained from strained and unstrained regions of the sample. In contrast to CBED, NBED uses a highly focused parallel beam of electrons to produce spot patterns from local regions of the sample. With the proper choice of condenser apertures and convergence angles of only 0.5 mrad, spot sizes of 3 to 5 nm can be readily achieved. Additionally, the spot patterns produced require much less data processing to determine strain values than the HOLZ

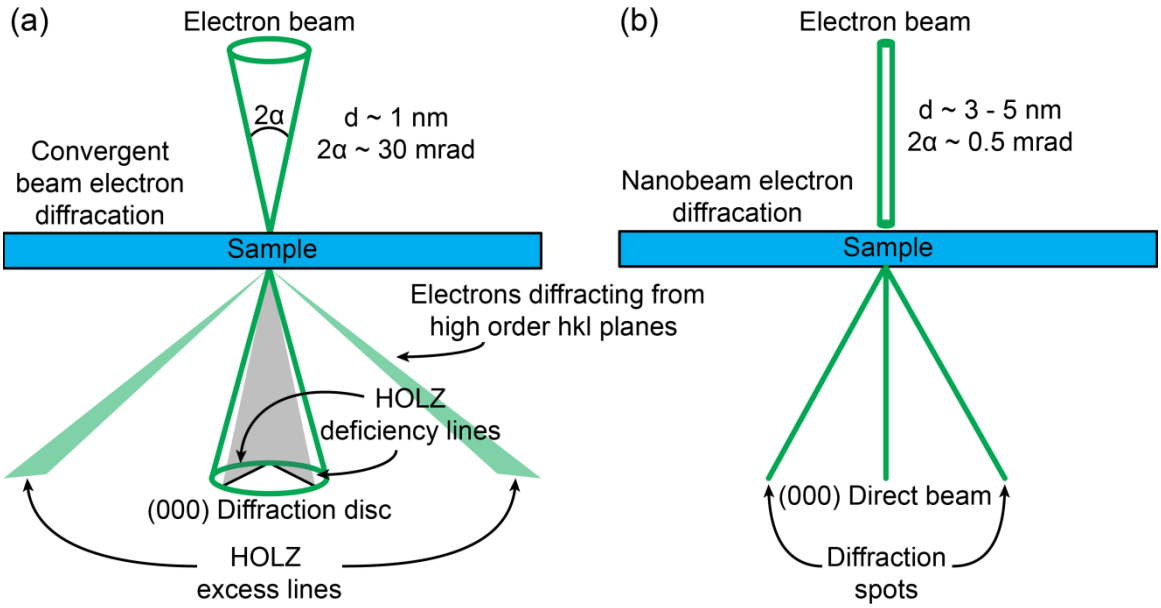

Figure 2-10. Schematic illustrating some of the key differences in how (a) CBED and (b) NBED are performed and the resulting diffraction patterns.

line patterns that are acquired from CBED. Using this technique, it has been demonstrated that strains can be measured with an accuracy on the order of 10^{-3} [44].

Figure 2-10 illustrates how NBED differs from CBED in both how it is performed and how the resulting diffraction patterns appear. Due to the nearly parallel beam of electrons, the 3D information contained in a CBED pattern is lost resulting in a spot pattern typical of a SAD pattern. Although this information is lost, NBED pattern analysis is more straightforward. By comparing the position of certain reflections in an area of interest to those in a strain free reference, distortion, strain, and rotation matrices can be calculated for those directions normal to the beam direction. Using this method, it has been shown that strains can be measured with a precision of 6×10^{-4} [44]. However, like CBED, NBED requires that a diffraction pattern be obtained one spot at a time making the technique sensitive to mechanical drift of the sample. This drift will limit the final spatial resolution of the technique over larger length scales and makes mapping strain extremely difficult.

2.3.5. GPA

Another technique suitable for nanoscale strain measurements is geometric phase analysis (GPA). In this technique, an atomically resolved image is separated into amplitude and phase images through the selection of specific *g*-vectors in Fourier space [45, 46]. The lattice image can first be described as a Fourier series:

$$I(r) = \sum_{g} H_g e^{2\pi i \boldsymbol{g}\cdot\boldsymbol{r}} \qquad (2\text{-}13)$$

where *I(r)* is the intensity of the image at a location *r* and *g* are vectors corresponding to the to the periodicity of the image. H_g are Fourier coefficients that can be expressed as

$$H_g = A_g e^{iP_g} \qquad (2\text{-}14)$$

where A_g is the amplitude and P_g is the phase of the sinusoidal fringes corresponding to a particular *g*-vector. In order to separate and calculate the phase and amplitude, a fast Fourier transform (FFT) is first performed on the lattice image and a mask is used to select the appropriate *g*-vector. By calculating the inverse Fourier of this masked image, a complex image is produced and can be defined as

$$H'_g(r) = A_g(r)e^{2\pi \mathbf{g}\cdot\mathbf{r} - 2\pi \mathbf{g}\cdot\mathbf{u} + P_g} \quad (2\text{-}15)$$

from which amplitude and phase images can be directly calculated. The phase image is then related to the displacement via the equation:

$$P_g(\boldsymbol{r}) = -2\pi \boldsymbol{g}\cdot\boldsymbol{u}(\boldsymbol{r}) \quad (2\text{-}16)$$

where ***u(r)*** is the displacement matrix. By defining a zero strain reference area in the sample, a strain map can then be generated over the entire image. GPA of both high resolution TEM (HRTEM) and lattice resolved STEM images have been shown to be useful in quantifying strain in nanostructures with spatial resolutions of a few nanometers [45, 47]. However, STEM images offer an advantage over HRTEM for GPA as they are less sensitive to variations in sample thickness and can be used for samples that would generally be too thick for HRTEM analysis. From these techniques, it has been shown that strain can be measured in devices with spatial resolutions in the range of 1 – 5 nm with standard deviations of 0.15% - 0.32% for total strains as low as 1.4% [47].

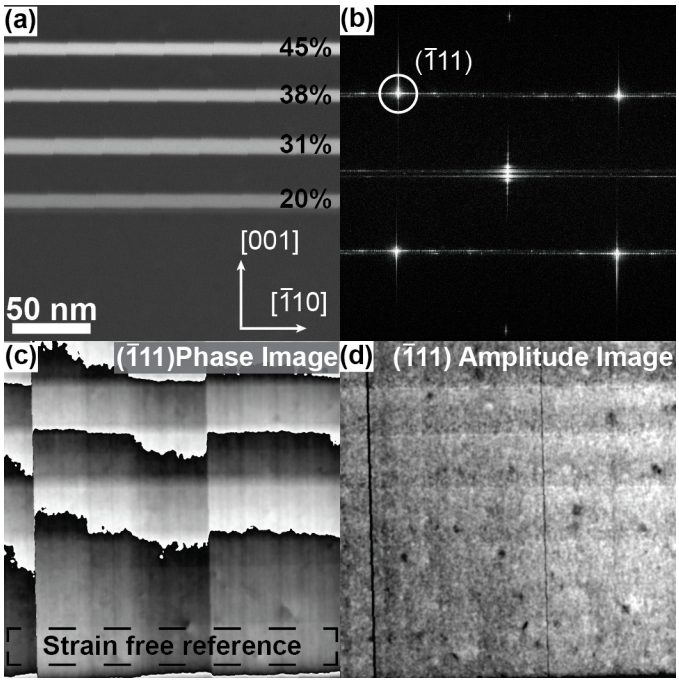

Figure 2-11. (a) STEM image of a Si-SiGe superlattice with increasing Ge content in each successive layer. (b) FFT image of lattice resolved STEM image in (a). (c) and (d) show respectively the phase and amplitude images obtained from the ($\bar{1}$ 11) g-vector. STEM image courtesy of Dr. David Cooper.

With this brief discussion we can consider the simple example of a Si-SiGe superlattice as shown in Figure 2-11. In this specific example, each successive layer of SiGe contains an increasing concentration of Ge, as indicated in Figure 2-11, which should result in an increasing in-layer strain due to Ge's larger lattice constant. After calculating the Fourier transform of the lattice resolved image in (b), appropriate *g*-vectors are chosen for use in extracting the phase and amplitude images. In this case, vectors of the {111} family are chosen and the resulting phase and amplitude images can be seen in Figure 2-11(c) and (d) respectively. Careful examination of the phase image already gives some indication of variation at the superlattice positions, though it is by no means evident due to the fact that the variation is being along a non-orthogonal direction to the layers. Furthermore, sharp transitions in phase from 0 to 2π (black to white) also hinder a direct interpretation of the phase image though they do not interfere with the calculation of the strain image. While the amplitude image does not directly contribute to the calculation of strain, it is important to note areas in the image where the amplitude is low. At these areas, the strain calculation is unreliable due to insufficient signal. Many times, this lack of signal is the result of

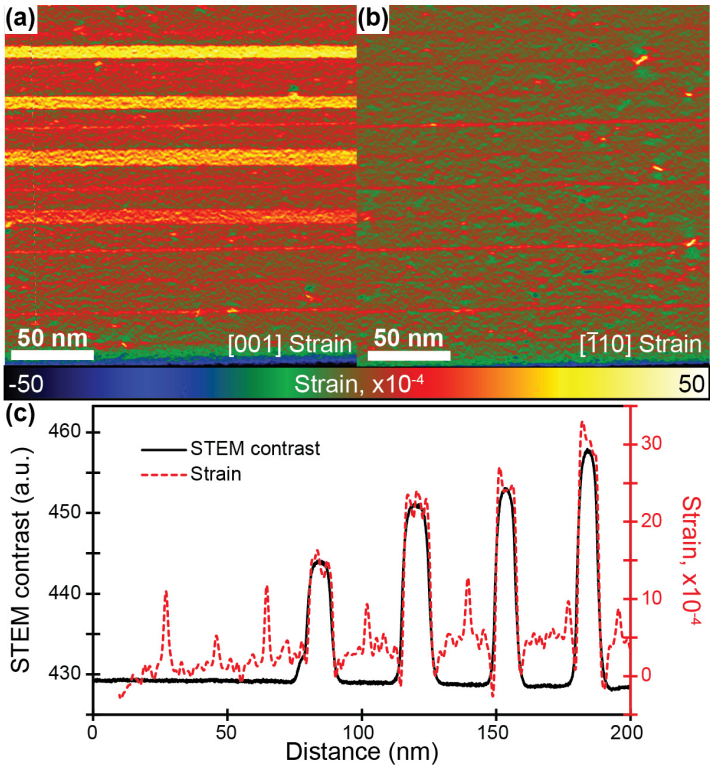

Figure 2-12. Strain maps calculated along the (a) growth and (b) in-plane directions for the Si-SiGe superlattice shown in Figure 3-10(a). (c) A comparative plot of the strain and STEM image contrast across the superlattice layers.

poor crystalline nature of the sample or, as in this example, due to errors in image acquisition.

Using the phase images from two vectors of the {111} family and defining an area of zero strain as shown in Figure 2-11(c), strain images along the growth direction [001] and in-plane direction [$\bar{1}$10] were obtained [Figure 2-12(a) and (b) respectively]. Along the growth direction, we see strain at each SiGe layer with increasing intensity as would be expected for a system with increasing Ge content. Additionally, in the plane of the superlattice layers there is no strain seen indicating that there is no appreciable amount of relaxation of the stressed layers with respect to the silicon lattice [48]. Plotting the growth direction strain against the STEM image contrast in Figure 2-12(c), highlights the ability of GPA to create strain maps with high spatial resolution though it also serves to highlight the care that must be taken to correctly interpret signal from noise.

2.3.6. High resolution TEM

While strain is the primary focus of this investigation, TEM offers a number of techniques that will prove invaluable in understanding various other aspects of the nanostructures. High resolution TEM takes advantage of the interaction of the direct beam and the many diffracted beams that are created as a planar wave of electrons passes through the sample. The interaction of these beams will create an interference pattern with characteristic spacings that are directly related to the interatomic spacing of the sample. Because the crystal lattice is not directly being imaged, interpretation of the HRTEM image is not always straightforward. The resulting image will be dependent on the thickness of the specimen, the imaging conditions of the microscope such as beam energy and defocus value. Depending on these conditions, areas of bright contrast could correspond to atomic columns, but do not necessarily have to. Therefore it is not unusual to observe inversions of contrast over a sample that, for example, has variations in thickness. Nevertheless, HRTEM is useful in identifying crystalline structure and localized defects such as dislocations that may be created at high strain interfaces. The state of the heterojunction interface will be an important consideration when formulating a mechanical model of the system.

2.3.7. Scanning transmission electron microscopy

As previously described, in STEM mode, a focused beam of electrons is rastered across the surface of the sample [Figure 2-3(b)]. The transmitted electrons are then collected by various

annular detectors below the sample. By collecting electrons scattered at different angles, different aspects of the sample can be highlighted. For example, a BF detector will mainly collect elastically scattered electrons and has been shown useful for a variety of situations such as light element imaging. [49] A HAADF detector, on the other hand, can be used to preferentially collect inelastically scattered electrons. Because, inelastic scattering is heavily dependent on the atomic number (Z) of the element, this imaging mode will highlight compositional differences in a sample. As a result, areas of a sample with a high average Z will have a brighter contrast compared to a region of low average Z. Additionally, because the contrast in the image is directly due to scattering from a single atomic column, HAADF-STEM imaging is much less sensitive to variations in thickness and does not suffer from the same contrast inversions often seen in HRTEM imaging. This makes image interpretation much simpler and reliable. However, STEM imaging does most often require a stable sample stage as sample drift can adversely affect final image quality due to the serial nature of image acquisition though post-processing techniques have been shown able to correct for these errors [50].

2.3.8. Energy Dispersive X-ray spectroscopy

Besides structural information, chemical information will also be important as changes in composition will change the lattice parameter of an alloyed ternary semiconductor and thereby the stress-state at a heterojunction interface. EDS is a powerful technique that can also be couple with STEM as it uses a focused beam to create high energy X-rays in small regions of the sample. As high energy electrons enter a sample some will scatter off other electrons in the core electronic shells of the materials atoms. This will stimulate a relaxation event emitting an X-ray of a characteristic energy. The X-rays can then be collected and used to characterize the type, location, and relative amounts of the various chemical components of a material.

2.4. Conclusions

Semiconducting nanostructures are an exciting platform for the design and fabrication of advanced optoelectronic devices due to their small size. However, it is their small size that make them inherently difficult to characterize. In this chapter, we have shown how SEM and TEM provide a suite of characterization techniques perfectly suited to nanoscale characterization. A particular focus was given to diffraction and similar techniques for strain quantification with

high spatial resolution. As powerful as these methods are, it is often necessary to combine them with various simulation methods in order to determine quantitative results. In the next chapter, we will explore several computational methods that will allow us to more thoroughly quantify and use the experimental data collected via our experimental techniques.

Chapter 3. Experimental methods – Finite element modeling of lattice mismatched nanostructures

In our discussion of transmission electron microscopy (TEM) for strain field determination the importance of reliable modeling techniques was pointed out. In a CBED study, not only must the CBED pattern simulations be performed to confirm the identity of a particular higher-order Laue zone (HOLZ) line, but the strain field itself must also be modeled in order to calculate how the HOLZ line splitting or shifting will occur. NBED and GPA will also benefit from a comparison to simulated strain fields as will be shown in later chapters. In this chapter we will discuss the various computational methods used for strain field calculation. Strain fields are modeled using the finite element analysis (FEA) method while CBED patterns are calculated using the Bloch wave method.

3.1. The finite element method

FEA is now a standard method for the calculation of a body's response to a number of external stressors. Although FEA can be applied to a number of different scenarios, only bodies that are in mechanical static equilibrium will be considered in this study. Such bodies must satisfy the equations for equilibrium, continuity, and the material's stress-strain laws. In one dimension these equation are written as follows:

$$EA\frac{d^2u}{dx^2} + f^B = 0 \qquad (3\text{-}1)$$

$$EA\frac{du}{dx}\Big|_{x=S_f} = R \qquad (3\text{-}2)$$

$$u|_{x=S_U} = 0 \qquad (3\text{-}3)$$

where E is the elastic constant of the material, A is the cross-sectional area, f^B is a body force, R is the reactionary force at the material pinning points, and u is the location of any material particle in the body. Equation 3-1 is the balance of internal and external work applied to the body, Equation 3-2 is a balance of the reactionary forces to the applied forces, and Equation 3-3 indicates that the body does not move at the specified fixed points. It should be here noted that the stress strain-law is contained within the expression of E. From these equations it is observed that any solution must be continuous to the second order, making analysis difficult. Therefore,

the principle of virtual work can be applied to avoid this requirement. This principle is a simple, yet powerful mathematical approach that allows these equations to be recast into a form that is more easily solved. To apply the principle of virtual work, the equation of equilibrium (Equation 3-1) is multiplied by an arbitrary virtual displacement $\bar{u}$, where the virtual displacement field $\bar{u}$ is continuous and is equal to 0 at fixed points prescribed by the model. Integrating the resulting equation over the length of the one-dimensional body yields

$$\int_0^l \left(EA\frac{d^2u}{dx^2} + f^B \right) \bar{u} dx = 0 \qquad (3\text{-}4)$$

Finally integrating by parts yields the variational formulation written as:

$$\int_0^L \frac{d\bar{u}}{dx} EA \frac{du}{dx} dx = \int_0^L f^B \bar{u}\, dx + R\bar{u}_L \qquad (3\text{-}5)$$

where we define the reactionary force acting over the length of the virtual displacement field as:

$$R\bar{u}_l = EA\frac{du}{dx}\bar{u}\Big|_0^l \qquad (3\text{-}6)$$

While the preceding derivation was done for a one dimensional system for simplicity, it is equally valid for three dimensional systems. These derivations can be found in any text dealing with the formulation of the finite element method [51]. It is important to note that although it has not been shown here, these two forms of the equations (the differential and the variational) are identical. Therefore, any solution that satisfies the first will also satisfy the second. Using this variational formulation, the model can be discretized and matrix methods can be applied to calculate a solution to the problem.

No FEA solution, however, will be able to completely satisfy the above equations due to the discretization of the important loads and masses; though it can be shown (and will be shown later in this chapter) that as the number of elements in a particular model increases, the FEA solution of a properly formulated model will converge to a corresponding analytical solution. FEA is particularly useful for complex geometries that analytical solutions would struggle to properly describe. It also makes the use of multiple materials systems a straightforward endeavor. Some of these strengths will be highlighted in our discussion of the FEA model formulated for the analysis of core-shell nanowire and thin film heterostructures.

3.1.1. The FEA mesh

One of the great advantages of the FEA method is its ability to model geometrically complex systems that would otherwise be intractable to solve analytically. This is achieved by breaking the model up into smaller more regularly shaped elements. The collection of all these elements is commonly referred to as the mesh. Each element in the mesh is comprised of a number of node points which are used to track the deformation of the element. The stress and strain of each individual element is then calculated according to the proper boundary conditions and external stressors to yield the final solution. It is therefore no surprise that the geometry of these elements is an important consideration in creating an FEA model. A wide number of different element types exist that are often designed for use in specific situations or for particular types of calculations (beams, trusses, thin shells, fluid flow, etc.); however, the two most common types of elements used for 2D or 3D static mechanical models are the 9-node rectangular element and the 27-node brick element (Figure 3-1), respectively. In general, elements with a higher number of nodes will be preferred as they are able to interpolate higher degrees of functional space. Take, for example, a 2D rectangular element like that shown in Figure 3-1(a) but with only 4 nodes located at the corners. Such an element could only interpolate changes in stress over the element as a linear function. The addition of edge and face centered nodes will allow for a full quadratic interpolation of stress variation. Similarly, a 27-node 3D brick element will be able to interpolate a higher functional space than an 8-node 3D brick element. The improved

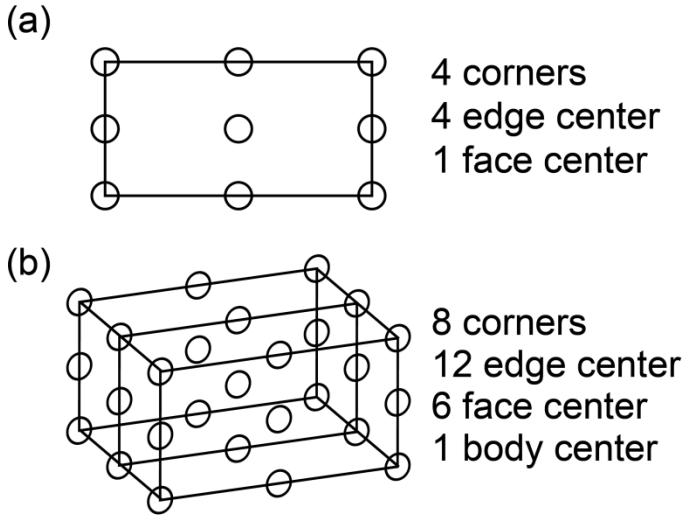

Figure 3-1. Schematic illustration of a 2D, 9-node rectangular element (a) and a 3D, 27-node brick element (b) commonly used in the FE analysis of static mechanical problems.

functionality of the higher-order elements will mean that fewer elements will be required for the FEA model to converge to the proper solution. Therefore, whenever possible, 9-node rectangular and 27-node brick elements were used in our 2D and 3D FEA models.

3.2. Modeling the systems of interest

In the previous section, the finite element method was presented as a recasting of the set of differential equations that govern a mechanical body. While a solution calculated using FEA should in principle be able to exactly match an analytical solution, care must be taken to properly set up the model including the loads, boundary conditions, solution parameters etc. It is therefore good practice to first use an analytical model to approximate the body's response to a particular stimulus and use this result to compare the FEA result against. This will allow for the immediate identification of erroneous solutions. In the following sections we will consider the analytical and FEA solutions to both thin-film and core-shell heterostructures. A comparison of FEA and analytical solutions will give more confidence to FEA models of systems not amenable to analytical investigation and allow us to better understand the origin of deviations from the standard model.

3.2.1. Thin-film heterostructures

We will first consider the analytical solution for the stress and strain in an epitaxial thin film. For a thin-film of material B on a semi-infinite substrate of material A, far from any edges the stresses in the layer can be expressed by the following equations:

$$\sigma_{xx} = C_{11}\varepsilon_{xx} + C_{12}\varepsilon_{yy} + C_{13}\varepsilon_{zz} \quad (3\text{-}7)$$

$$\sigma_{yy} = C_{12}\varepsilon_{xx} + C_{11}\varepsilon_{yy} + C_{13}\varepsilon_{zz} \quad (3\text{-}8)$$

$$\sigma_{zz} = C_{13}\varepsilon_{xx} + C_{13}\varepsilon_{yy} + C_{33}\varepsilon_{zz} \quad (3\text{-}9)$$

$$\sigma_{xy} = \sigma_{xz} = \sigma_{zz} = 0 \quad (3\text{-}10)$$

where σ_{ij} is the stress along each direction, C_{ij} is the stiffness constant, and ε_{ij} are the respective strain components. These equations assume in-plane directions X and Y with Z being the substrate normal. Additionally, it assumed that material has at least an orthotropic symmetry typical of hexagonal structures. Using the fact that the surface normal is a free surface, the strain component ε_{zz} can be written as:

$$\varepsilon_{zz} = -\frac{2C_{13}}{C_{33}}\varepsilon_{xx} \tag{3-11}$$

given that the in-plane strain components ε_{xx} and ε_{yy} are equal. Additionally, if we assume that the material is free of defects, the in-plane strain will simply be the lattice mismatch *m* defined as:

$$m = \frac{a_A - a_B}{a_B} \tag{3-12}$$

where a_A and a_B are the lattice constants of materials A and B, respectively.

While these equations will allow us to directly calculate the stress in the layers, it will be more useful to instead compare values of strain. By looking at strain values instead of stresses, we will be able to direct compare experimental data to both FEA and analytical results. This fact will become more apparent during our discussion of nanobeam electron diffraction and geometric phase analysis in Chapter 5. To compare strains calculated from FEA models, we must first define the material misfit and strain slightly differently. Strain due to lattice misfit is created in FEA through a pseudo-thermal expansion. Therefore, each material in the model is given a coefficient of thermal expansion equal to its misfit with the substrate material – with its sign chosen based on whether the material should expand (positive) or contract (negative). Since strain values will be calculated with respect to the substrate as a reference, we must consider Lagrange strains in our analytical calculations. The Lagrange misfit, *f*, is defined as:

$$f = \frac{a_B - a_A}{a_A} \tag{3-13}$$

Accordingly, the Lagrange strain, ε'_{ij}, is related to the material strain by the following equation:

$$\varepsilon'_{zz} = \varepsilon_{zz}(f + 1) + f = \varepsilon_{zz}\left(\frac{1}{m + 1}\right) - \frac{m}{m + 1} \tag{3-14}$$

For a hexagonal material with two lattice parameters *a* and *c*, Equation 3-14 becomes:

$$\varepsilon'_{zz} = \varepsilon_{zz}(f_a + 1) + f_c \tag{3-15}$$

where f_a and f_c are the Lagrange misfits of the *a* and *c* lattice parameters, respectively.

We will now consider the case of a thin film of AlN on a GaN substrate. Using the materials parameters in Table 3-1, a Langrange strain of -0.0533 is calculated using the above

Material	C_{11} (GPa)	C_{12} (GPa)	C_{13} (GPa)	C_{33} (GPa)	C_{44} (GPa)	a (nm)	c (nm)
GaN	367	135	103	405	95	3.189	5.186
AlN	396	137	108	373	116	3.112	4.982

Table 3-1. Materials parameters for GaN and AlN used in analytical and FEA solutions

analytical solution. With these same parameters, an FEA model of the system calculates a strain of -0.0535 – a difference of less than 0.5%. This result therefore gives confidence to the FEA model and enables us to construct more complex models that would be difficult to solve analytically. In Chapters 4 and 5, we will discuss the strain in nanoribbon structured high-electron mobility transistor containing two stacked thin films and several free surfaces. In this investigation, FEA will play a major role in allowing us to understand experimental data collected by TEM techniques.

3.2.2. Core-shell nanowire heterostructures

Core-shell nanowires present an interesting extension of the idea of a planar heterointerface by wrapping that interface around on itself creating a "substrate" core and a "thin-film" shell. Most core-shell nanowires have relatively complex geometries making analytical solutions difficult. The FEA method, however, lets us easily calculate the stress and strain fields for any arbitrary geometry. However, it will still be important to consider the FEA model's ability to replicate analytical solutions. Therefore, we will first consider an analytical solution of a simplified geometry and compare an FEA model with similar assumptions and slowly change these assumptions to better reflect the physical nanowire system.

3.2.2.1. The analytical solution

Various analytical solutions for core-shell heterostructures have been developed – though each uses slightly different assumptions about the model system or considers the misfit strain in a different fashion [52, 53]. Therefore, in creating a finite element model for this investigation, an analytical model was chosen that best fit what the FEA sought to represent. In their 2005 paper, Liang *et al.* looked at the enhancement of SiGe thin film deposition on Si nanowires over the standard deposition on planar Si substrates. They first develop an analytical model to describe the stress and strain created due to the lattice mismatch between the SiGe shell and Si core. The

authors begin by using pressure vessel theory to describe the stress and strain in the outer shell and the inner core in terms of P_i – the misfit induced pressure. By considering the axisymmetric nature of the problem and balancing the forces in the z direction, the following equations are derived to describe the stress and strain fields in the shell as a function of radius r:

$$\sigma_{or} = -\frac{E\varepsilon^{misfit}}{1-\nu}\frac{c^2\left[1-\left(\frac{a}{r}\right)^2\right]}{2a^2} \tag{3-16}$$

$$\sigma_{o\theta} = -\frac{E\varepsilon^{misfit}}{1-\nu}\frac{c^2\left[1+\left(\frac{a}{r}\right)^2\right]}{2a^2} \tag{3-17}$$

$$\sigma_{oz} = -\frac{E\varepsilon^{misfit}}{1-\nu}\frac{c^2}{a^2} \tag{3-18}$$

$$\varepsilon_{or} = -\frac{c^2\varepsilon^{misfit}(1+\nu)}{2a^2(1-\nu)}\left(1-\frac{a^2}{r^2}\right) \tag{3-19}$$

$$\varepsilon_{o\theta} = -\frac{c^2\varepsilon^{misfit}(1+\nu)}{2a^2(1-\nu)}\left(1+\frac{a^2}{r^2}\right) \tag{3-20}$$

$$\varepsilon_{oz} = -\frac{c^2\varepsilon^{misfit}}{a^2} \tag{3-21}$$

where c is the radius of the core, a is the radius of the nanowire including the shell, E is the elastic constant, v is Poisson's ratio, and ε^{misfit} is the strain created by the difference in lattice parameter, defined as $(a_{SiGe} - a_{Si})/a_{Si}$. While in the core, the stress and strain fields are described by:

$$\sigma_{ir} = \frac{E\varepsilon^{misfit}}{1-\nu}\frac{a^2-c^2}{2a^2} \tag{3-22}$$

$$\sigma_{i\theta} = -\frac{E\varepsilon^{misfit}}{1-\nu}\frac{a^2-c^2}{2a^2} \tag{3-23}$$

$$\sigma_{oz} = -\frac{E\varepsilon^{misfit}}{1-\nu}\frac{a^2-c^2}{a^2} \tag{3-24}$$

$$\varepsilon_{ir} = \frac{a^2-c^2}{2a^2}\varepsilon^{misfit}\frac{1-3\nu}{1-\nu} \tag{3-25}$$

$$\varepsilon_{i\theta} = \frac{a^2-c^2}{2a^2}\varepsilon^{misfit}\frac{1-3\nu}{1-\nu} \tag{3-26}$$

$$\varepsilon_{iz} = \frac{a^2 - c^2}{a^2}\varepsilon^{misfit} \qquad (3\text{-}27)$$

It should also be noted that the authors assumed the same elastic constants for both the shell and core and that both materials are isotropic[54].

The GaAs/InAs system was used as a first test case to verify the suitability of the FEA model due to the large lattice mismatch between the materials (7.7%). Table 3-2 shows a summary of the relevant materials properties that were used in both the analytical and FEA solutions [55, 56].

Material	Elastic constant (GPa)	Poisson's ratio	Lattice constant (Å)
GaAs	119	0.3	5.6233
InAs	83.4	0.35	6.0583

Table 3-2. Relevant materials properties used in analytical and FEA solutions

Using these values (the elastic constant for GaAs is used for both core and shell) and assuming a 50 nm core diameter with 25nm shell thickness, both the radial and hoop stresses are calculated as a function of radius using Equations 3-16, 3-17, 3-22, and 3-23. A careful examination of the plots in Figure 3-2 helps us to understand what is physically occurring in this model. The discontinuity at 50 nm in both plots is the result of the misfit at the heterointerface. Since the

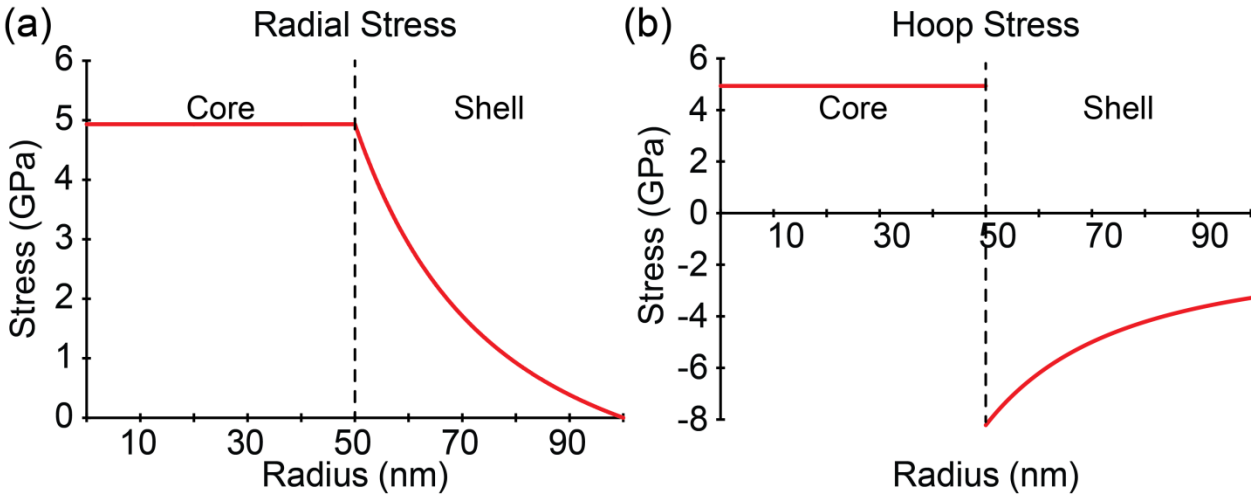

Figure 3-2. Analytical calculations of the (a) radial and (b) hoop stresses of a core-shell nanowire heterostructures.

core has a smaller lattice parameter in this case it will be pulled out in all directions resulting in a positive hoop and radial stress components. In the shell, a negative hoop stress results due to compression at the interface where the lattice is most confined. Closer to the surface, the hoop stress relaxes though from the equations it is evident that it will only relax to a certain value regardless of how far away from the interface it is. Likewise, the positive radial stress relaxes closer to the free surface, though it does reach zero as would be expected.

3.2.2.2. 2D FEA models

Having seen what the analytical model predicts, an appropriate FEA model can now be formulated and the results compared. To replicate the same assumptions as the analytical model,

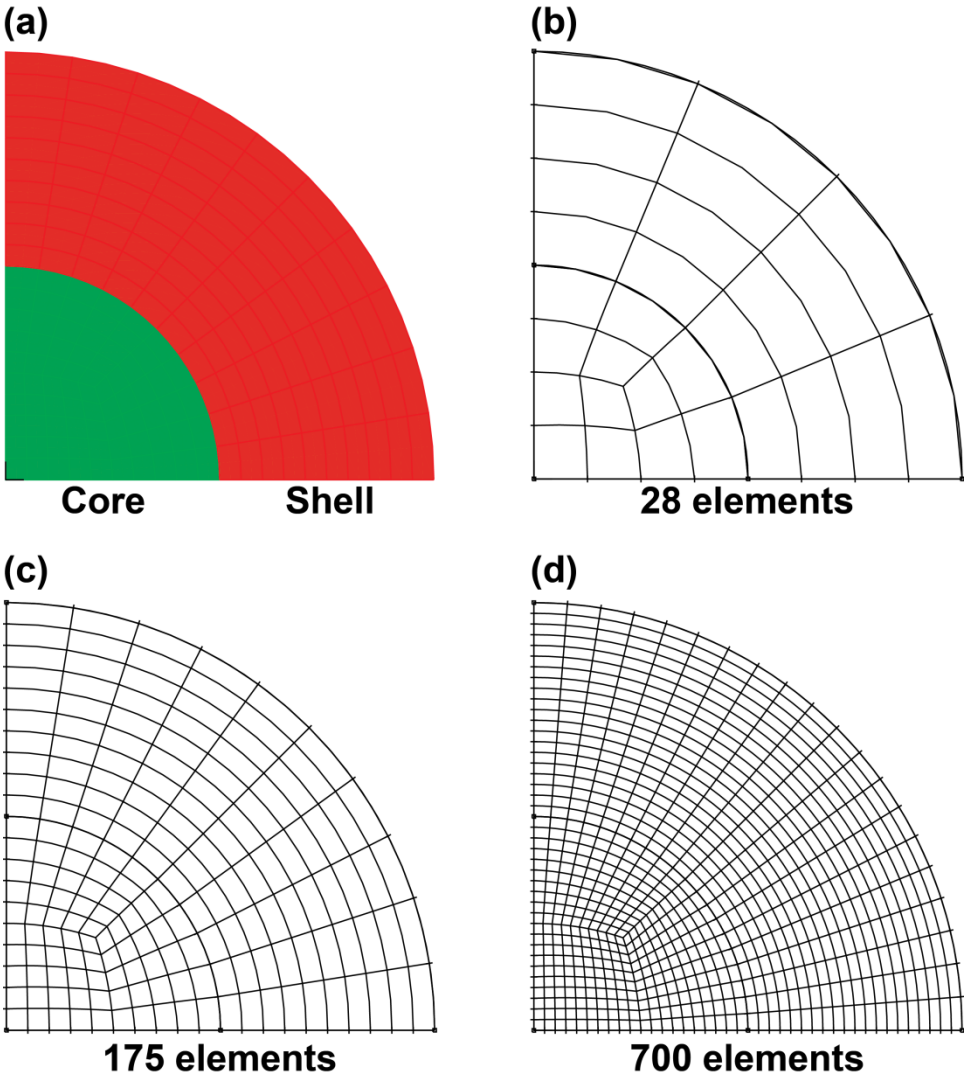

Figure 3-3. (a) Geometry and examples of the model meshed using (b) 28, (c) 175, and (d) 700 elements

a model consisting of a circular geometry was used, isotropic materials with equal elastic constants, and a 2D plain strain model was used. All 2D meshes consisted of 9-node rectangular elements. The high symmetry of the model also allows us to take advantage of symmetric boundaries which are defined as having no displacement of nodes perpendicular to the boundary. Creating symmetric boundaries along two perpendicular axes of the model will result in a quarter section and reduce computation time. Figure 3-3 shows the geometry and series of meshes that were used in the FEA calculation of the stress fields. As in the previous thin-film example, the lattice misfit was created in the FEA model through the use of a pseudo-thermal expansion – a method commonly used in literature [57]. This was accomplished by first calculating the lattice misfit between the two materials. Then particular values of thermal expansion were assigned to each material such that at a specific temperature, the material with a lager lattice constant will expand creating the proper value of misfit at the interface. Therefore, in this solution, the shell material was given a thermal expansion coefficient of 0.0774 (the lattice misfit between the two materials) and a uniform temperature of 1 degree was applied to the system creating a thermal expansion equal to the lattice misfit. The results of this calculation can be seen in Figure 3-4. Plotting the radial and hoop stresses calculated by the FEA model on top of the analytical model shows excellent agreement. It is also evident that as the number of elements increase the FEA result converges more closely to the analytical solution. Unless otherwise noted, all future 2D FEA models are composed of 175 elements to balance computation time and accuracy.

3.2.2.3. 2D hexagonal models

Having shown that the FEA model can reproduce the analytical results given the same assumption, changes can now be made to model that will more closely reflect the physical problem. With each new model, the results must be checked to ensure that deviations correlate with the changes made to the model's assumptions. The changes that were made in this case include: the use of two materials constants, hexagonal geometry, and formulating a 3D model that resembles a typical TEM sample geometry. Each of these incremental changes results in predicable changes to the hoop and radial stress curves.

While the inclusion of a different elastic constant for the shell material creates only minor differences, the creation of a model with a more accurate geometry is seen to have more significant effects. While nanowires can exhibit a number of different cross-sectional shapes,

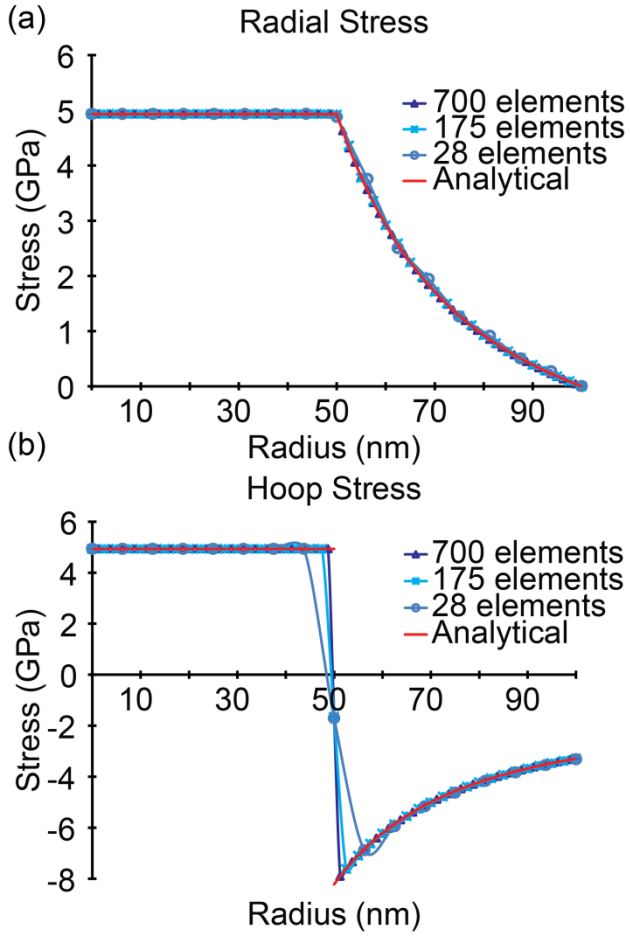

Figure 3-4. Comparison of the analytical and finite element analysis solutions for the (a) radial and (b) hoop stress.

hexagonal cross-sections are the most common shape for cubic materials grown along a (111) crystallographic direction (e.g. GaAs, GaP, InAs). Figure 3-5 shows the effective, radial, and hoop components of the calculated stresses for the hexagonal cross-section. From these images we can see similarities with the circular cross-section, but also some key differences. First, we can notice that the core is in tension while the shell is under compression; however, the tension in the core is no longer constant as was the case for the circular cross-section (Figure 3-4).

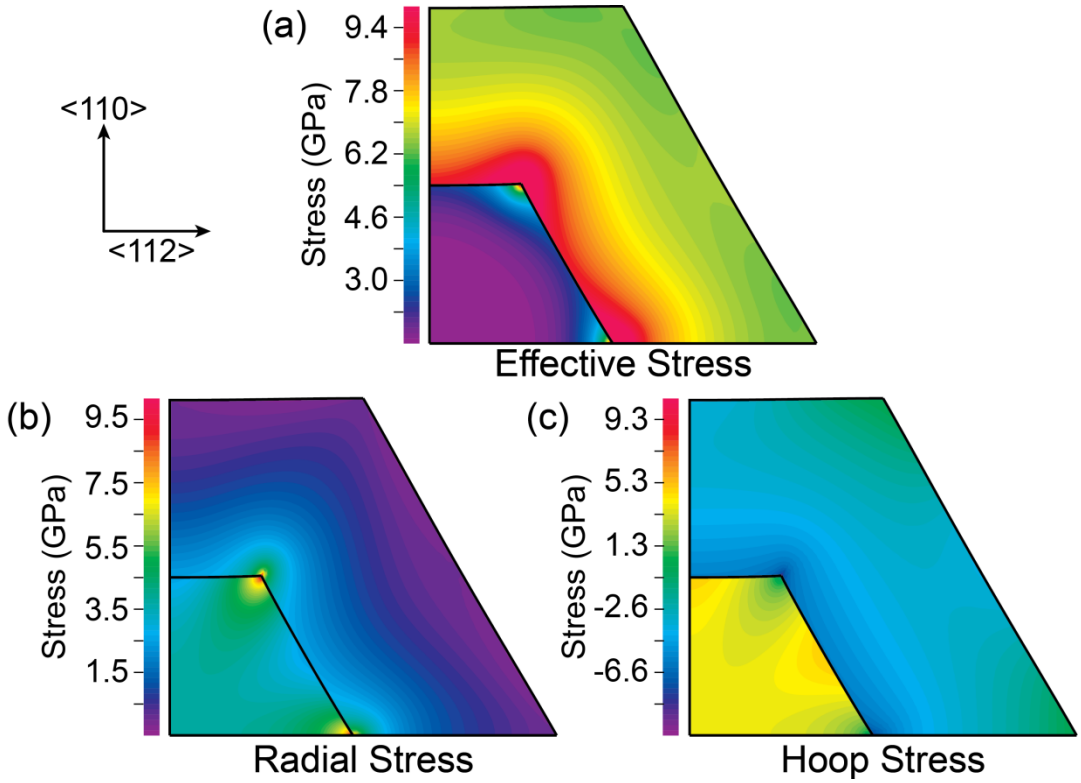

Figure 3-5. (a) Effective, (b) radial, and (c) hoop stress band plots for a 2D hexagonal nanowire cross-section.

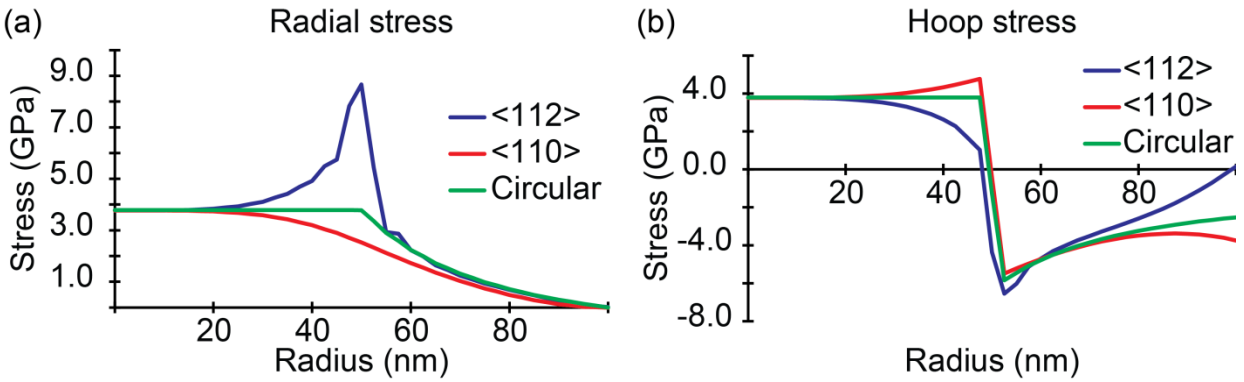

Figure 3-6. Plots of the (a) radial and (b) hoop stress along the two main directions of a hexagonal cross section compared to the stresses calculated for a circular section.

Additionally, while the hoop and radial stresses still exhibit some radial symmetry allowing for the continued use of quarter sections, differences in the stress field are now apparent along various directions, especially at the core-shell interface. For convenience, two directions corresponding to the crystallographic directions in GaAs will be defined and referred to throughout this study: the first direction from the center of the nanowire through the facet center will be the ⟨110⟩ direction, while the direction through the corner will be the ⟨112⟩ direction. These directions are chosen to match the observed geometries of nanowires used in this study and discussed in Chapter 6. A comparison (Figure 3-6) of the radial and hoop stresses along these directions with the stresses in a cicular structure shows that the most significant deviations occur at the heterointerface and nanowire surface. These deviations can be understood by considering the changes in geometry. The flat interface of a hexagonal section causes increases in hoop stress at the interface over that observed in a circular structure since there is more material to create stress in this direction. This is also why the hoop stress at the surface of the shell begins to become more negative. Likewise, the radial portion acts over a larger effective area, reducing the radial stress near the interface. In contrast to a facet, at a corner where there is less effective material to impose stress in the hoop direction, the hoop stress is observed to decrease at interface and relax to 0 GPa at the surface; however, the radial component shows a sharp increase at the interface before relaxing back to 0 GPa at the surface as the force in the radial direction is acting on an infinitely small area. While the increase in stress at the corner makes sense from a geometric point of view, the fact that the corner is perfectly sharp makes it liable to result in a singularity during the FEA calculation.

To investigate the nature of the stress fields at the interface corners, a series of finer meshes were created and the stress value at this node was calculated. It was observed that the stress increases with increasing number of elements used in the model. Plotting the stress in Figure 3-7 revealed that the increase is proportional to the logarithm of the number of elements clearly identifying this as a singularity [51]. This singularity is due to the sharp corner that results from the hexagonal geometry. Because radial stresses pull outward in all directions, the stress in the core of a circular core shell nanowire is constant as this force is distrbuted over an equal area in all directions. At a corner, however, this force is now acting on an infinitely small area leading to the observed singularity. This problem is easily corrected by rounding the corners

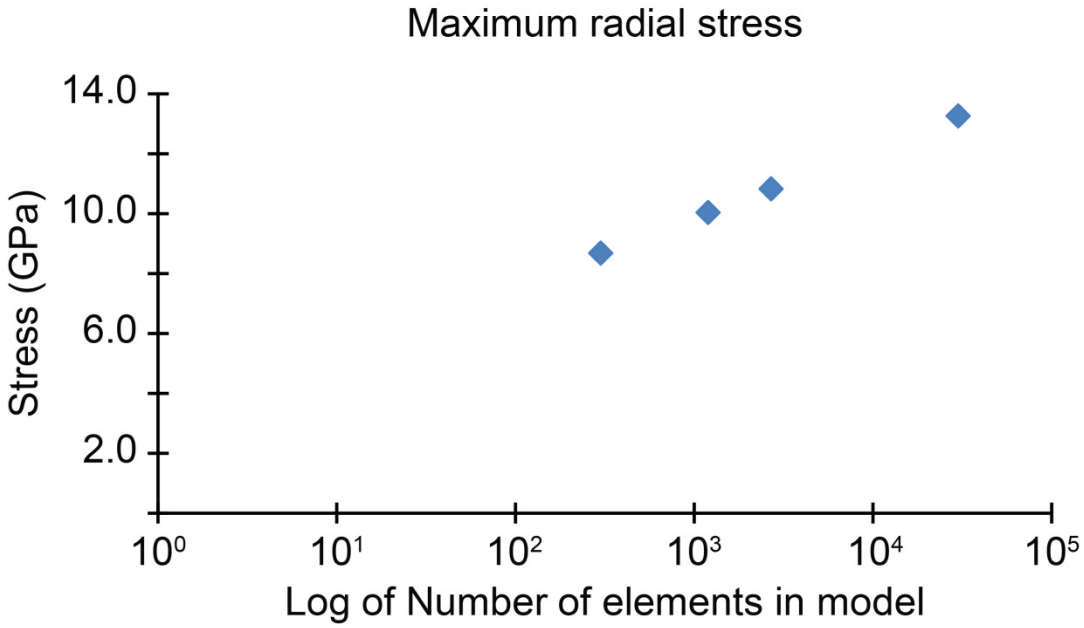

Figure 3-7. Semi-log plot of the maximum radial stress calculated for a core-shell nanowire at the heterointerface along the ⟨112⟩ direction as a function of elements in the model.

of the hexagon which – as we will show in Chapter 6 – is a more accurate representation of the physical system.

3.2.2.4. 3D hexagonal models

Finally it is important to examine how finite geometries along the growth axis will affect the stress profile of this core-shell structure. Since the structures used for experimental observation are not infinitely long, free surface effects will likely play a significant role in determining the final stress and strain fields. The thickness of the 3D hexagonal model is set at 80 nm, a typical

thickness observed for FIB-prepared TEM samples. The 3D models used the same isotropic materials constants shown in Table 3-2 and the same symmetric boundaries along the ⟨110⟩ and

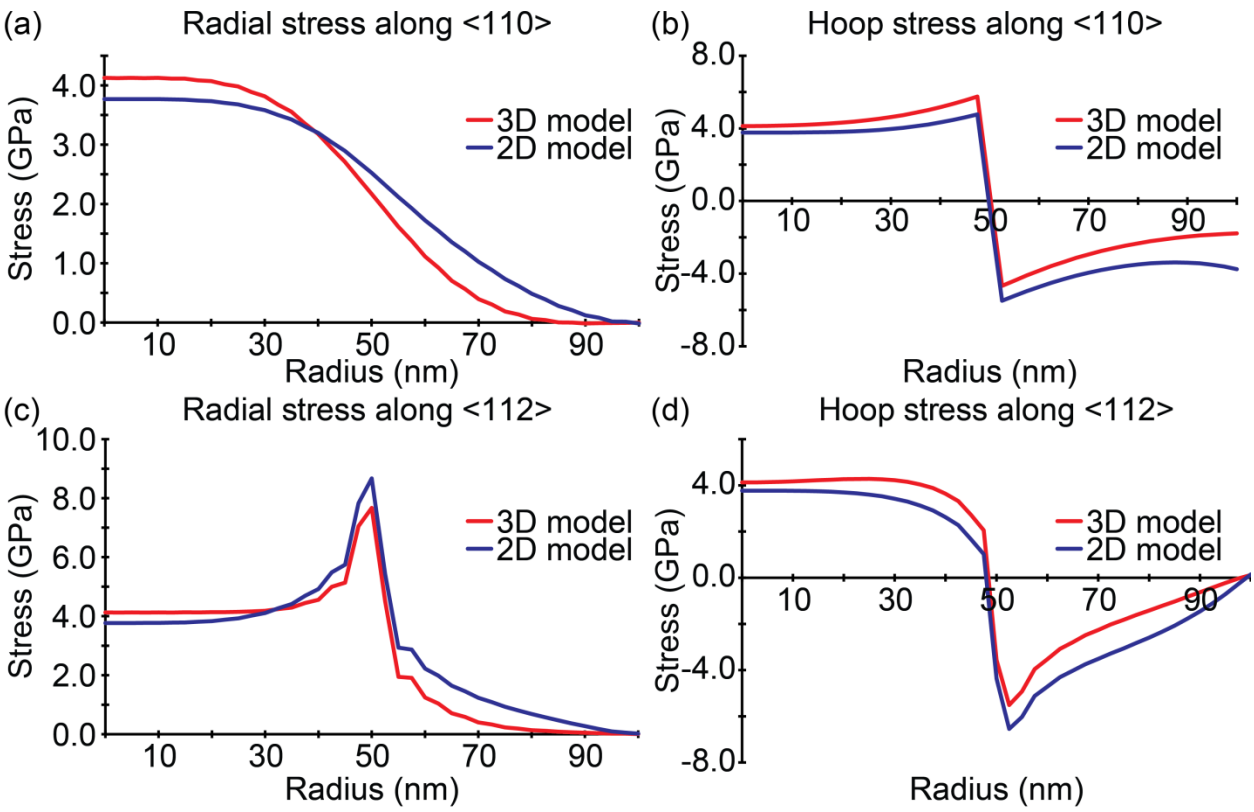

Figure 3-8. Comparison of the radial and hoop stress components along the <110> and <112> directions for 2D and 3D models.

⟨112⟩ directions. A third symmetric boundary is also created along the ⟨111⟩ direction. This boundary plane represents the midplane through the thickness of the nanowire cross section and assumes that the stress fields are symmetric in the front and back halves of the nanowire section. Plots of the hoop and radial stress curves (Figure 3-8) were obtained from the midplane of the 3D section where it most resembles the previous plane strain results of the 2D models. A quick glance of these plots shows clear similarities with definite differences that are arise from the creation of near free surfaces. The new surfaces allow for relaxation of axial stress that affects the radial and hoop stress components through a Poisson effect.

To this point it has been shown that the FEA method is able to reproduce exactly the analytical solution for the stress fields in a core-shell nanowire heterostructure given the same set of assumptions. Furthermore, as these assumptions are changed to better reflect the physical system of interest, the effects on the stress fields are seen to change in predictable and sensible

ways. While the final example discussed was very close to the actual system, further improvement can be made and will be discussed further in Chapter 6.

3.3. CBED simulation

Chapter 2 discussed how CBED can be a powerful tool for probing the local strain fields of a material. By themselves, however, CBED patterns are difficult to interpret and generally only provide qualitative information. In contrast, the FEA method allows for the exact calculation of strain fields but cannot be directly correlated to sample information contained in CBED images. While NBED and GP can be directly compared to FEA results, these techniques are not applicable to every sample as will be shown in Chapter 6. Therefore, it is necessary to identify another means by which these two sets of data can be compared. The following section will explore simulation of CBED patterns and show how calculated strain data from FEA can be used to generate series of simulated CBED patterns that can be directly correlated to experimental data.

The simulation of CBED patterns in perfect crystals or crystal with uniform strain fields has become almost routine thanks to well-developed tools such as the EMS program developed by Pierre Stadleman [58, 59]. These tools allow for precise measurement of lattice parameters, strain, accelerating voltages, etc. The general goal of electron diffraction simulation is to calculate the exit wave function of the electron beam after traveling through the sample. As discussed in Chapter 2, when the electron beam enters a sample inelastic scattering creates many diffracted beams that interact with the direct beam. These interactions will lead to the formation of CBED patterns and high resolution TEM (HRTEM) images. Therefore, calculation of this exit wave is extremely helpful in the interpretation of diffraction patterns and HRTEM images. Two main methods exist for exit wave calculation: the Bloch wave method and multislice calculations. Due to practical limitations of using multislice calculation methods, the Bloch wave method was chosen as the most suitable toolset for CBED simulation. In particular, all simulations are performed using the previously mentioned EMS program.

3.3.1. The Bloch wave method

The Bloch wave method seeks to calculate the electron exit wave function, ψ, by directly solving the time-independent Schrödinger equation:

$$\nabla^2\psi(xyz) + \frac{8\pi^2 me}{h^2}[E + \varphi(xyz)]\psi(xyz) = 0 \qquad (3\text{-}28)$$

where φ is the crystal potential, E is the accelerating voltage, m is the electron mass, and h is Plank's constant. By considering the crystal potential as a Fourier series, the wave function inside the crystal can be written as the sum of Bloch waves:

$$\psi(\boldsymbol{r}) = \sum_g C_g e^{[2\pi i(\boldsymbol{g}+\boldsymbol{k})\boldsymbol{r}]} \qquad (3\text{-}29)$$

where C_g are the Bloch coefficients, **k** is an arbitrary wavevector, and **g** is a reciprocal lattice vector. Combining Equations 3-28 and 3-29, yields the following equation:

$$\{k_0^2 - (\boldsymbol{k} + \boldsymbol{g})^2\}C_g + \sum_{h \neq g} U_{g-h}C_h = 0 \qquad (3\text{-}30)$$

with

$$U_g = \frac{2meV_g}{h^2} \qquad (3\text{-}31)$$

$$k_0 = \frac{2me(E + V_0)}{h^2} \qquad (3\text{-}32)$$

and V_g being the electron structure factor. Equation 3-30 can also be expressed in matrix form as:

$$\begin{bmatrix} k_0^2 - \boldsymbol{k}^2 & U_{-g} & U_{-h} & \cdots \\ U_g & k_0^2 - (\boldsymbol{k}+\boldsymbol{g})^2 & U_{g-h} & \cdots \\ U_h & U_{h-g} & k_0^2 - (\boldsymbol{k}+\boldsymbol{h})^2 & \cdots \\ \cdots & \cdots & \cdots & \cdots \end{bmatrix} \cdot \begin{bmatrix} C_0 \\ C_g \\ C_h \\ \cdots \end{bmatrix} = 0 \qquad (3\text{-}33)$$

This form of the equation allows for all the Bloch coefficients to be solved using matrix diagonlization. After solving for all C_i, the final wave amplitude of the exit wave can be calculated by

$$\phi_g(t) = \sum c \cdot C_g \cdot e^{2\pi i \lambda t} \qquad (3\text{-}34)$$

and the diffraction intensities for a crystal of thickness t by

$$I_g = \left|\phi_g(t)\right|^2 \qquad (3\text{-}34)$$

Looking at Equation 3-33, it can be seen that the size of the matrix – and consequently the time of the calculation – depends mainly on the number of beams, $\boldsymbol{g}$, included in the calculation.

Therefore, it is important to choose the optimal number of beams to produce the most accurate results without making computation times too lengthy. While the number of beams in a solution can generally be specified, there are a number of factors that affect the number of beams included in the calculation many of which are illustrated graphically in Figure 3-9. From Chapter 2, we remember that the only beams that are diffracted are those that satisfy the Bragg condition. This condition can be illustrated graphically as those reciprocal lattice points (relrods) that are intersected by the Ewald sphere. Therefore, by changing shape of the Ewald sphere, the number

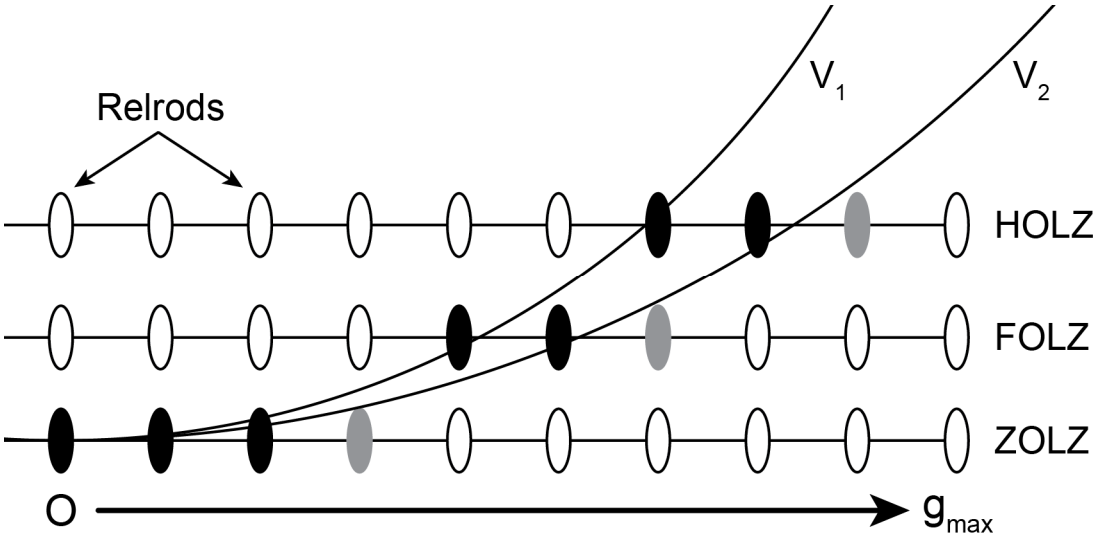

Figure 3-9. Graphical illustration of beams strongly excited (black ellipses) by the Ewald sphere and beams only weakly excited (gray ellipses)

of reflections in the calculation will also change. The curvature of the Ewald sphere is a function of accelerating voltage and increases with decreasing voltage (i.e. the radius decreases). As a result, increasing the accelerating voltage ($V_1 < V_2$) allows more reciprocal lattice points to intersect with the Ewald sphere. Figure 3-9 also illustrates that increasing the number of Laue zones (LZ) included in the calculation will naturally increase the number of beam in the calculation.

The final parameter to consider is the excitation error (s_g). As shown in Figure 3-9 and previously discussed in Chapter 2, not all relrods exactly intersect with the Ewald sphere; the excitation error is a measure of the deviation from the exact Bragg condition. Beams with a small excitation error are considered strongly excited (black relrods) while those with a larger error are

only weakly excited (gray relrods). By setting a maximum value of s_g, we can increase or decrease the number of beams considered strong or weak in the calculation.

Ideally, we would like to consider both strong and weak beams in our diffraction calculation; however, this may make calculation times too large. In his 1928 paper, Bethe showed that these weak beams could be excluded from the calculation while their interaction with the strong beams could still be included [60]. Let us first consider the simple case of four beams: two strong ($\boldsymbol{g_0}$ and $\boldsymbol{g_1}$) and two weak beams ($\boldsymbol{g_2}$ and $\boldsymbol{g_3}$). Using Equation 3-33 we can write the following 4×4 matrix

$$\begin{bmatrix} k_0^2-(\mathbf{k}+\mathbf{g_0})^2 & U_{0-1} & U_{0-2} & U_{0-3} \\ U_{1-0} & k_0^2-(\mathbf{k}+\mathbf{g_1})^2 & U_{1-2} & U_{1-3} \\ U_{2-0} & U_{2-1} & k_0^2-(\mathbf{k}+\mathbf{g_2})^2 & U_{2-3} \\ U_{3-0} & U_{3-1} & U_{3-2} & k_0^2-(\mathbf{k}+\mathbf{g_3})^2 \end{bmatrix} \cdot \begin{bmatrix} C_0 \\ C_1 \\ C_2 \\ C_3 \end{bmatrix} = 0 \qquad (3\text{-}36)$$

We can now consider the strong and weak beams separately by writing

$$\begin{bmatrix} k_0^2-(\mathbf{k}+\mathbf{g_0})^2 & U_{0-1} \\ U_{1-0} & k_0^2-(\mathbf{k}+\mathbf{g_1})^2 \end{bmatrix} \begin{bmatrix} C_0 \\ C_1 \end{bmatrix} = -\begin{bmatrix} U_{0-2} & U_{0-3} \\ U_{1-2} & U_{1-3} \end{bmatrix} \begin{bmatrix} C_2 \\ C_3 \end{bmatrix} \qquad (3\text{-}37)$$

and

$$\begin{bmatrix} k_0^2-(\mathbf{k}+\mathbf{g_2})^2 & U_{2-3} \\ U_{3-2} & k_0^2-(\mathbf{k}+\mathbf{g_3})^2 \end{bmatrix} \begin{bmatrix} C_2 \\ C_3 \end{bmatrix} = -\begin{bmatrix} U_{2-0} & U_{2-1} \\ U_{3-0} & U_{3-1} \end{bmatrix} \begin{bmatrix} C_0 \\ C_1 \end{bmatrix} \qquad (3\text{-}38)$$

where the Equation (3-37) represents the strong beams and the Equation (3-38) the weak beams. To eliminate the weak beams from the calculation but still include their interaction with the strong beams, we can use a process of elimination to combine Equations 3-37 and 3-38 and obtain a result written only in terms of the strong beam Bloch coefficients C_0 and C_1:

$$\left\{ \begin{bmatrix} k_0^2-(\mathbf{k}+\mathbf{g_0})^2 & U_{0-1} \\ U_{1-0} & k_0^2-(\mathbf{k}+\mathbf{g_1})^2 \end{bmatrix} - \begin{bmatrix} U_{0-2} & U_{0-3} \\ U_{1-2} & U_{1-3} \end{bmatrix} \right. \\ \left. \times \begin{bmatrix} k_0^2-(\mathbf{k}+\mathbf{g_2})^2 & U_{2-3} \\ U_{3-2} & k_0^2-(\mathbf{k}+\mathbf{g_3})^2 \end{bmatrix}^{-1} \begin{bmatrix} U_{2-0} & U_{2-1} \\ U_{3-0} & U_{3-1} \end{bmatrix} \right\} \times \begin{bmatrix} C_0 \\ C_1 \end{bmatrix} = 0 \qquad (3\text{-}39)$$

To simplify this equation we will replace ($\boldsymbol{k} + \boldsymbol{g_i}$) with k_0 – that is we will approximate the eigenvalue of the Bloch wave, *i,* as the incident wavevector k_0 inside the crystal resulting in the following equation:

$$\begin{bmatrix} k_0^2 - (\mathbf{k}+\mathbf{g_0})^2 & U_{0-1} \\ U_{1-0} & k_0^2 - (\mathbf{k}+\mathbf{g_1})^2 \end{bmatrix} \begin{bmatrix} C_0 \\ C_1 \end{bmatrix} - \begin{bmatrix} \frac{U_{0-2}U_{3-0}}{U_{3-2}} + \frac{U_{0-3}U_{2-0}}{U_{2-3}} & \frac{U_{0-2}U_{3-1}}{U_{3-2}} + \frac{U_{0-3}U_{2-1}}{U_{2-3}} \\ \frac{U_{1-2}U_{3-0}}{U_{3-2}} + \frac{U_{1-3}U_{2-0}}{U_{2-3}} & \frac{U_{1-2}U_{3-1}}{U_{3-2}} + \frac{U_{1-3}U_{2-1}}{U_{2-3}} \end{bmatrix} \begin{bmatrix} C_0 \\ C_1 \end{bmatrix} = 0 \quad (3\text{-}40)$$

Equation 3-40 shows how the contributions from weak beams are taken into account by modifying the strong beam potentials and eliminating the weak beam Bloch coefficients reducing the size of the matrix from 4×4 (Equation 3-36) to 2×2. These modified potentials are commonly referred to as Bethe potentials. The use of Bethe potentials has been shown to be an effective method of reducing computation time while still producing accurate results [61-63].

The equations developed and discussed in the previous section are the basis of the dynamical theory of electron diffraction. That is, they show how the crystal potentials, U_i, couple and interact with the Bloch waves via the Bloch coefficients, C_i. In our investigations we will also consider and use kinematic simulations of HOLZ line patterns which are useful for the initial identification and indexing of HOLZ patterns. Unlike dynamical simulations with account for multiple diffraction events and interaction of the beams, kinematic calculations consider only single diffraction events and are based solely on the crystal geometry and Bragg's law. The general process involves first, the determination of spots including in the zeroth order Laue zone (ZOLZ). Second, the radius of the N^{th} order Laue zone (first = FOLZ, second = SOLZ, etc.) where N is greater than zero. Finally, the intersection of the Laue zone ring with the spots in the ZOLZ pattern are recorded and matched with its corresponding line in the (000) direct beam. Using this simple approach, the positions of many HOLZ lines can be quickly determined and matched to experimental patterns making kinematic simulations the preferred method for HOLZ line indexing. A fuller description of this kinematic approach can be found in Fournier's 1989 paper [64].

3.4. Conclusions

This chapter has explored two key computational methods which will enable us to better understand, interpret, and quantify experimental data. The FEA method is a powerful tool that allows for the calculation of stress and strain fields in systems that would be intractable to solve analytically. Through the use of a mesh and matrix solution methods, strain fields in models with

complex geometries and multiple materials are easily calculated. The Bloch wave method for CBED pattern simulation provides a crucial link between theory and experiment. By calculating the exit wave function of an electron beam through a material, the effects of a strain field on the resulting diffraction pattern can be directly seen and compared to experimental results. In the following chapters, both of these methods will be combined with the experimental techniques described in Chapter 3 to quantify and map strain fields in semiconducting nanostructures providing new insights into material behavior and informing future device design and fabrication.

Chapter 4. Correlating Stress Generation and Sheet Resistance in InAlN/GaN Nanoribbon High Electron Mobility Transistors

This chapter reports the nanoscale characterization of the mechanical stress in InAlN/GaN nanoribbon-structured high electron mobility transistors (HEMTs) through the combined use of convergent beam electron diffraction (CBED) and elastic mechanical modeling. The splitting of higher order Laue zone lines in CBED patterns obtained along the [540] zone axis indicates the existence of a large strain gradient in the *c*-direction in both the planar and nanoribbon samples. Finite element models were used to confirm these observations and show that a passivating layer of Al_2O_3 can induce a tensile stress in the active HEMT layer whose magnitude is dependent on the oxide layer thickness, thus providing important ramifications for device design and fabrication.

4.1. Introduction

Due to their inherently one-dimensional structure and high surface-to-volume ratio, nanowires and nanoribbons offer promising routes toward integration of III/V materials on silicon[65] and realization of novel heterostructures not achievable by thin film techniques [7, 29, 66, 67]. The ability of nanostructured materials to efficiently relax stress at heterointerfaces is especially important for the realization of advanced electronic and optical devices and can be used to further tune device properties such as emission wavelengths[8, 66, 67] or electronic carrier characteristics such as mobility [6, 7]. At the same time, characterization of stress and strain in these nanostructures is inherently difficult; techniques typically used in bulk systems – such as X-ray diffraction and micro-Raman spectroscopy – lack the spatial resolution needed to probe stress on the nanoscale as discussed in Chapter 1. Convergent beam electron diffraction (CBED) is a technique that can be used to measure strains as low as 10^{-4} and with spatial resolutions on the order of 1 nm making it a powerful tool for stress/strain state characterization of nanostructured devices, as previously discussed in Chapter 2. This level of precision is achieved by tracking higher order Laue zone (HOLZ) lines resulting from the diffraction of electrons off high order lattice planes, which makes their position highly sensitive to changes in lattice parameters caused by strain. Traditionally, CBED has only been useful for characterizing regions of samples containing small homogenous strain fields [68, 69] due to the complex splitting of

HOLZ line patterns that are produced from a strain gradient [70]. However, recent work has shown that a combination of kinematic diffraction simulations and elastic mechanical modeling can be a powerful approach in determining the stress state of highly strained samples [71]. Chapters 4 and 6 will show how by tracking both the splitting and shifting of HOLZ lines, the stress state of the sample can be determined on the nanoscale.

4.2. InAlN/GaN nanoribbons for HEMT devices

Due to its wide bandgap and high electron mobility, GaN is an important materials system for the realization of high-frequency and high-power electronic device applications. Traditionally, an AlGaN barrier has been used for the fabrication of GaN-based high electron mobility transistor (HEMT) devices; however, due to the large lattice mismatch at the AlGaN/GaN interface, the performance and reliability of these devices is often limited by strain induced defects [72] or strain relaxation [18]. It has therefore been proposed that InAlN could be used as an alternative to AlGaN due to its ability to be grown lattice-matched on GaN while maintaining a high intrinsic polarization difference with GaN, necessary for a high charge density in the channel [20]. It has also been shown that the carrier concentration in an InAlN/GaN heterojunction can be enhanced through the application of a tensile stress [73], making it a promising candidate for piezodoping. Recently, nanoribbon structures were proposed as a novel route towards mitigating device performance degradation due to scaling effects through further confinement of electronic carriers [23, 24].

In studying nanoribbon structured InAlN/GaN HEMT devices, it was shown that the sheet resistivity of the devices decreased as the thickness of the passivating Al_2O_3 layer increased, and that significant improvement could be achieved over planar structured devices when the thickness of the Al_2O_3 layer was sufficient to cause a planarization of the oxide layer [Figure 4-1]. The significant decrease in sheet resistance was attributed to an additional tensile stress introduced by the passivating oxide layer, which could increase the electronic carrier concentration at the InAlN/GaN interface thereby lowering sheet resistance, although the exact mechanism has remained unknown. Therefore, to further enhance device fabrication and performance, understanding the stress generation mechanisms is critical for future tailoring of HEMT device performance. In this chapter, we use CBED combined with finite element analysis (FEA) to measure the evolution of stress in nanoribbon structured InAlN/GaN HEMTs. This new

understanding of stress in the device is then used to explain trends in sheet resistance that were observed as a function of passivating oxide thickness [24].

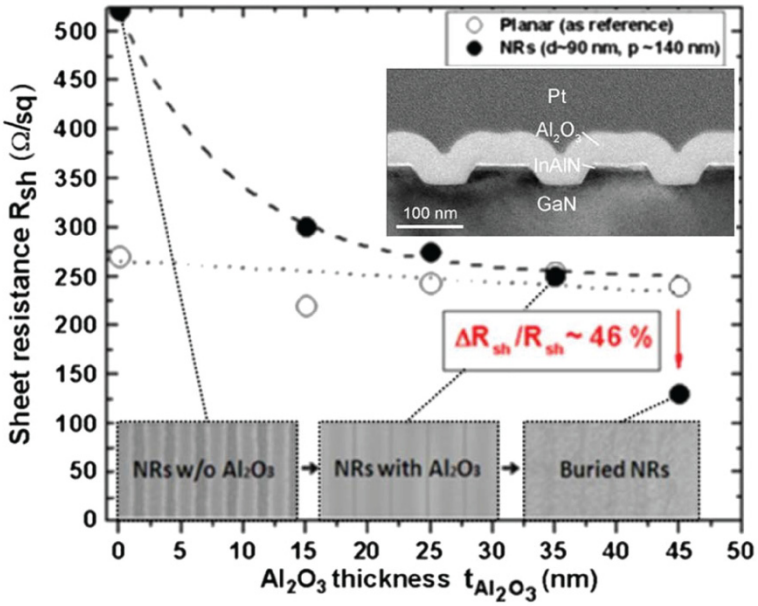

Figure 4-1. Sheet resistivity measurements of InAlN/GaN nanoribbon HEMT structures compared to planar structures as a function of Al_2O_3 thickness. Top inset shows a BF-TEM cross-sectional image of some typical ribbon structures [17].

4.3. Fabrication and characterization techniques

Nanoribbon HEMT structures were fabricated through a top-down process utilizing electron-beam lithography and dry etching techniques illustrated in Figure 4-2 and published elsewhere [24]. InAlN/GaN layers were grown on a SiC substrate using metal-organic chemical vapor deposition. The HEMT structure consists of a ~1.8 μm thick Fe-doped GaN layer grown on SiC, followed by the deposition of a ~1 nm AlN barrier layer, and finally a ~7 nm layer of $In_{0.17}Al_{0.83}N$ (nominal composition). Transmission electron microscopy (TEM) investigations were performed on as-grown layers that were subjected to standard device fabrication steps. The process begins with mesa isolation performed using electron cyclotron resonance reactive ion etching (ECR-RIE). Ti/Al/Ni/Au metal stacks were then deposited and annealed to form ohmic source and drain contacts. Nanoribbons were next defined between the ohmic contacts of a number of devices using electron beam lithography and fabricated using low-power ECR-RIE, while other devices retained their planar structure for comparison. A conformal layer of Al_2O_3 was deposited on the surface of all samples using atomic layer deposition (ALD) with various thicknesses ranging from 0 – 45 nm. TEM samples were obtained from the region between the

source and drain contacts using standard focused ion beam (FIB) techniques. A 2 µm thick Pt layer was deposited during FIB preparation to protect the HEMT layers from the damaging effects of the Ga beam during course milling at 30 kV. Final thinning of the sample was performed at 5 kV to ensure a high quality surface for TEM.

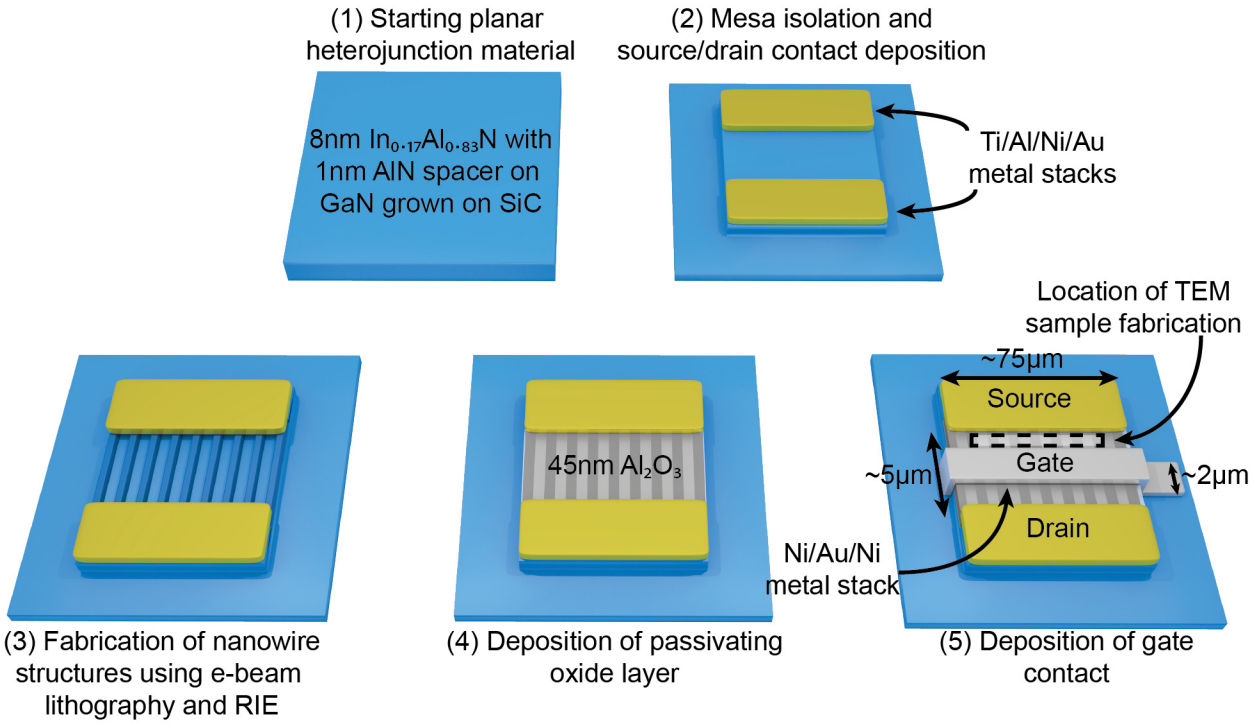

Figure 4-2. Schematic illustration of the processes involved in the fabrication of InAlN nanoribbon structures.

4.4. TEM investigations

TEM investigations were performed using a JEOL 2010F equipped with a field-emission electron source and operated at an accelerating voltage of 200 kV. Bright field (BF) images were obtained using a charge-coupled device (CCD) camera while dark-field scanning TEM (DF-STEM) images were acquired using an annular dark-field (ADF) detector. CBED patterns were obtained in STEM mode using spot size of approximately 1 nm and a convergence angle of 30 mrad. All diffraction simulations were performed using the JEMS software suite previously described [58, 59]. It should be noted that while the four index Miller-Bravais notation is commonly used to describe hexagonal systems such as GaN and InAlN, the standard three index Miller notation will be used throughout the following discussion of CBED due to the fact that the JEMS software suite uses this notation almost exclusively.

4.4.1. Bright-field TEM

As discussed in Chapter 3, the variation of diffraction conditions across a sample is a major source of contrast changes in BF-TEM. This allows for the detection of areas within a sample where the atomic arrangement, or lattice, is different. In single-crystalline samples, such as our GaN/InAlN HEMT structure, this change in lattice could be due to a change in lattice parameter or the presence of a strain field. Therefore, the analysis of BF-TEM images of the nanoribbon structures could provide preliminary information about the strain fields near the HEMT interface. It should also be noted that while diffraction contrast is dominant, changes in mass across a sample will also contribute to contrast difference.

Figure 4-3 shows cross-sectional BF-TEM images of several nanoribbon structures. The overall structure of the FIB prepared sample can be seen in these images with the protective Pt layer on top of the ALD deposited Al_2O_3. The regularly spaced ribbons are clearly visible having been etched out of the GaN substrate. On top of each ribbon is a thin layer of InAlN and AlN. Several different contrasts can be observed in these images and give some indication of what the strain fields look like. Well below each ribbon in the GaN substrate, the contrast is relatively flat and even; closer to the HEMT interface, however, a darker contrast is seen to extend several tens of nanometers below the interface. This dark contrast is most likely due to the strain generated at the interface and indicates a rapid increase in deformation near the heterointerface. Immediately above each nanoribbon a thin bright layer of contrast is observed. Because the ALD-oxide layer is amorphous, it is unlikely that this bright contrast is strain related. Using EDS (not shown), it was determined that this bright layer was due to a high concentration of C. While the source of this C is not clear, it could be due to improper cleaning of the surface after dry etching to form the ribbons and prior to oxide deposition.

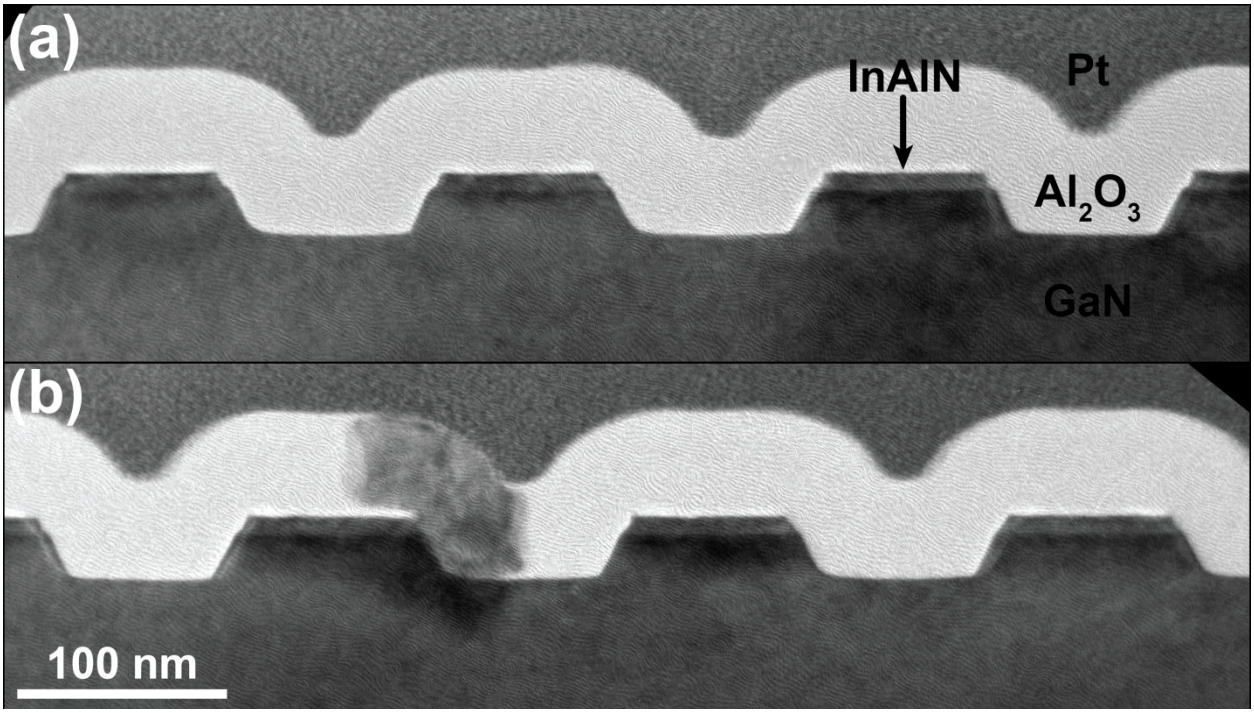

Figure 4-3. Cross-sectional BF-TEM images of several nanoribbon structures

Figure 4-3(b) shows a second interesting contrast. Above one of the nanoribbon structures, a large section darker contrast is observed within and throughout the amorphous oxide layer. High resolution TEM (HRTEM) images [Figure 4-4] of this area indicates that this portion of the oxide layer has crystallized due to interaction with the electron beam. Furthermore, due to its proximity with the GaN, the oxide forms a type of epitaxial relationship with the substrate as evidenced by the series of fast Fourier transform (FFT) images seen in Figure 4-4. This transformation to a crystalline material could have a significant impact on the strain state of the nanoribbon structure. Not only would a difference in lattice parameter between the GaN and Al_2O_3 induce new stresses, but the change in elastic constants could also lead to higher stresses in the HEMT region. Figure 4-3(b) does indeed show that the region of material underneath the crystalline oxide has a darker contrast than similar areas of other nanoribbons indicating the creation of new strain fields. Due to the difficulty in controlling the crystallization of the amorphous oxide in TEM, however, this study will seek to avoid its formation and instead focus on the stress created by the InAlN/GaN heterointerface only. Nevertheless, this observation does suggest novel methods of inducing stress in the HEMT structure through the use of a phase changing material. If the crystallization of the oxide could be better controlled, it would provide

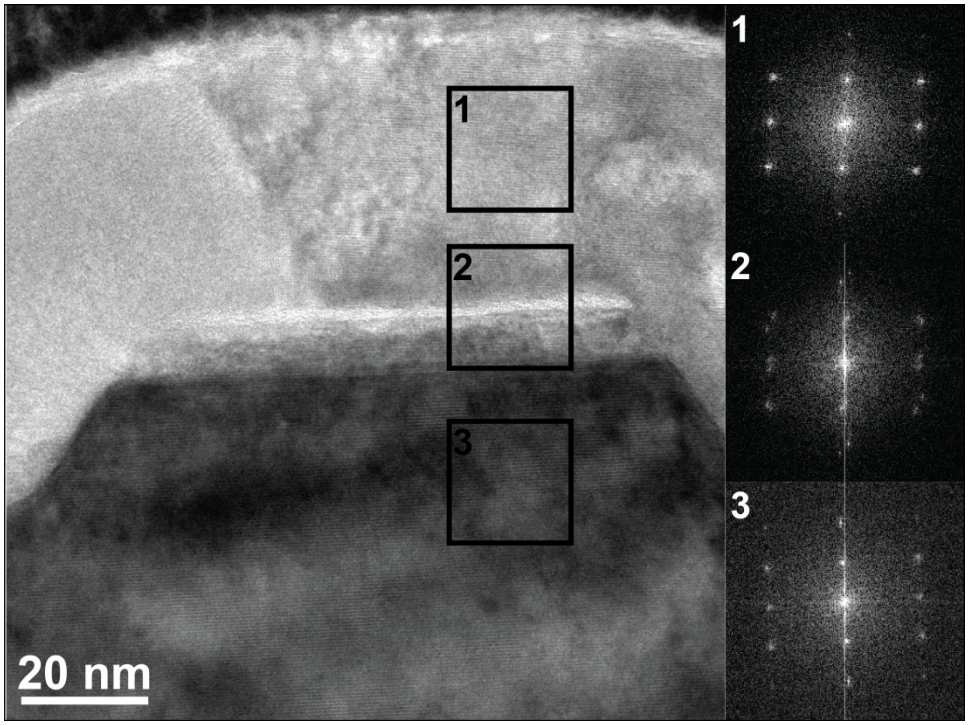

Figure 4-4. HRTEM image of a nanoribbon with a crystallized layer of oxide on top. The boxes number 1 – 3 demark the area of the sample from which the corresponding FFT images are obtained.

a straightforward method for inducing large stresses in the HEMT interface leading to higher carrier concentrations at the interface and improved device performance.

4.4.2. Strain analysis by CBED

While BF-TEM provides some general knowledge of strain fields associated with the heterointerface, direct characterization and quantization of the strain fields is still necessary for further device optimization. Therefore, we first employed CBED to measure local changes in stress state of the electron-transparent TEM samples fabricated from both planar and nanoribbon HEMT devices. Cross-sectional dark-field scanning TEM (DF-STEM) images of representative planar and nanoribbon structures [Figure 4-5(a) and (b) respectively] show the device structure consisting of the GaN substrate, InAlN HEMT layer, and 45 nm passivating Al_2O_3; we note that 1 nm AlN barrier layer is not visible at this magnification. Unlike in BF-TEM, the main contrast mechanism in DF-STEM is the changes in average atomic number across a sample. Therefore, materials with a higher average atomic number (e.g., GaN) will appear bright while those with low atomic number will appear dark (e.g., Al_2O_3). Strain and diffraction will still contribute to the contrast of the image as is evidenced by the slight increase in contrast near the HEMT interface in Figure 4-5.

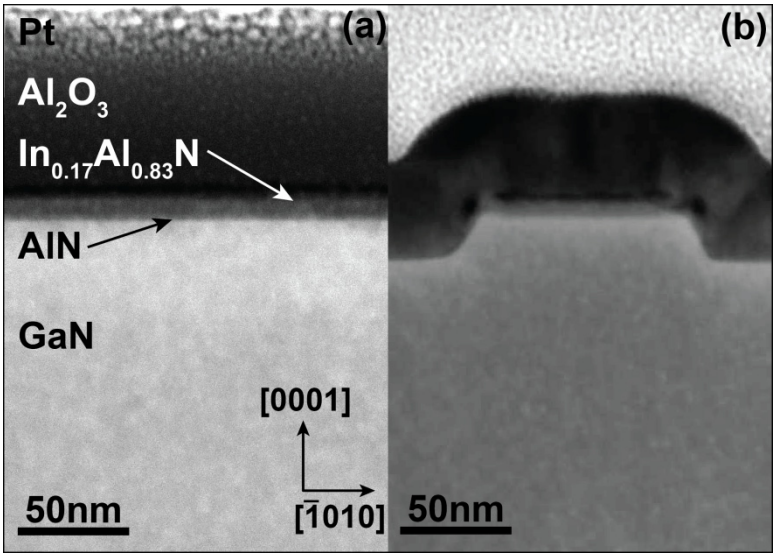

Figure 4-5. Cross-sectional DF-STEM images of representative (a) planar and (b) nanoribbon structures investigated in this study.

We measured the strain state of both planar and nanoribbon HEMT structures by recording CBED patterns in these samples at different distances from the InAlN/Al_2O_3 interface, as discussed below. The strain state of a thin TEM sample can be determined by analyzing both the position and width of individual HOLZ lines contained in the CBED pattern [74]; a non-uniform strain field – like the one created due to free surface relaxation – will cause HOLZ lines to broaden and split forming HOLZ bands whose width is directly related to the sample strain gradient along the direction of the electron beam [70]. The characterization of strain is best achieved using off-axis CBED patterns due to the dynamic diffraction effects that result from the interaction of various diffracted beams within the sample and are prominent along high-symmetry zone axes. Dynamic effects can be minimized by tilting the sample to a low-symmetry axis where fewer beams meet the appropriate diffraction criteria and produce a pattern that contains a high number of sharp, well-defined HOLZ lines.

In this study, the [540] zone axis was found experimentally as the most appropriate for CBED studies and was indexed using kinematic simulations. Dynamic simulations were performed to confirm the lack of significant dynamic diffraction effects and were also used to determine sample thickness with accuracy of approximately ±5 nm. Figure 4-6(a) shows an example of a typical experimental CBED pattern obtained along the [540] zone axis while Figure 4-6(b) shows a dynamical simulation of the same zone axis demonstrating a high level of agreement with few discrepancies. It is also important to note that the [540] zone axis is

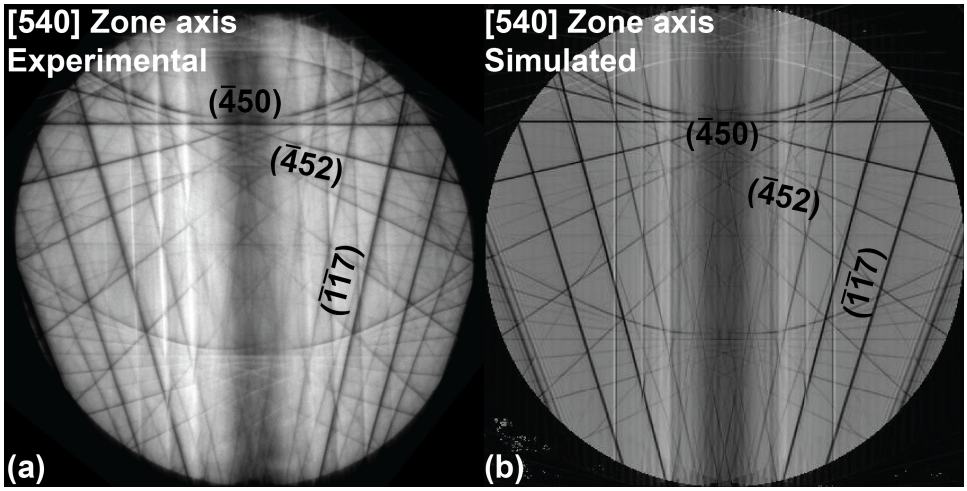

Figure 4-6. (a) Experimentally obtained and (b) simulated CBED pattern along the [540] zone axis in GaN with important HOLZ lines labeled

perpendicular to the growth direction [001]. This geometry results in some lines within the CBED pattern being highly indexed along the growth direction [e.g., ($\bar{1}\,\bar{1}$ 7)] and others with no component along the growth direction [e.g., ($\bar{4}$ 50)] as shown in Figure 4-6. As it will be shown shortly, this geometry will allow us to more easily identify the important strain components in the system.

Series of CBED patterns were obtained from both planar and nanoribbon samples in a line perpendicular to the InAlN/AlN/GaN HEMT interface beginning in the bulk and moving closer to the InAlN/Al_2O_3 interface [Figure 4-7(a) and (b)]. Far away from the interface (>100 nm), CBED patterns are observed to have well-defined, sharp HOLZ lines indicating a relaxed, strain-free region of the sample. Patterns from these regions were used to determine the thickness of each sample to be 70 nm and 90 nm for the nanoribbon and planar samples, respectively. Moving closer to the HEMT interface, HOLZ lines begin to split and broaden as shown by the evolution of the ($\bar{1}\,\bar{1}$ 7) line in Figure 4-7(c) and (d). Moreover, by examining the series of patterns from both the planar and nanoribbon samples, we observed that HOLZ lines that are highly-indexed in the *c*-direction, such as the ($\bar{1}\,\bar{1}$ 7), begin to split further away from the interface than the lines with low *c* indices, such as the ($\bar{4}$ 50) which shows no splitting throughout the series of CBED patterns. This finding indicates the existence of a significant strain gradient in the [001] direction. Comparing CBED patterns from the two samples, it can be observed that splitting begins further away from the HEMT interface in the planar sample

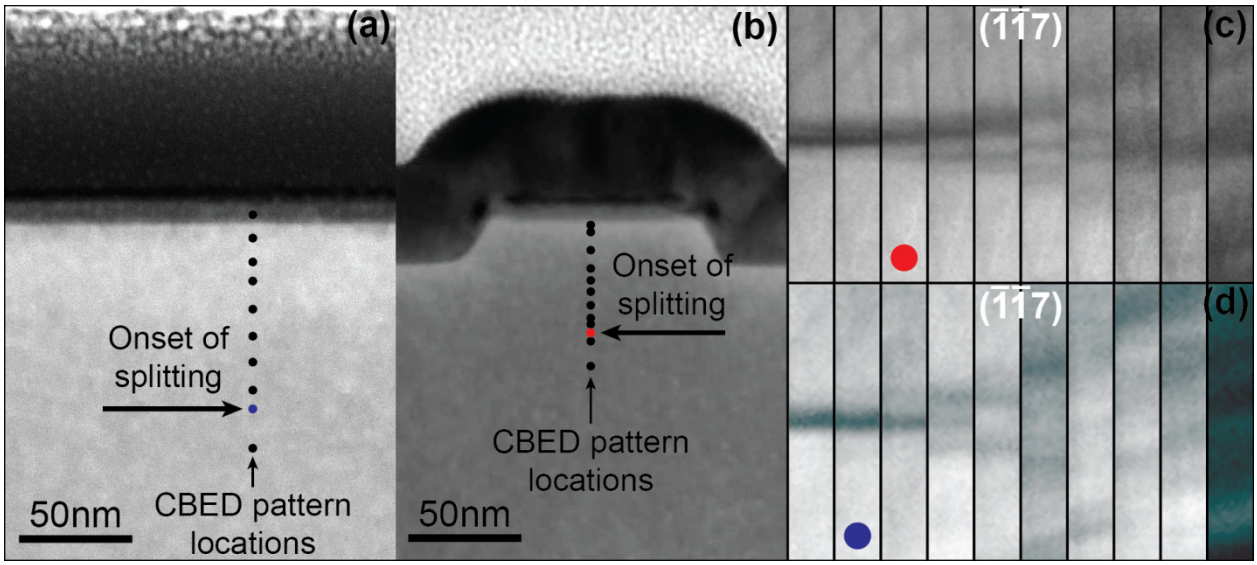

Figure 4-7. DF-STEM images of (a) planar and (b) nanoribbon HEMT structures showing the locations where CBED patterns were obtained. (c) and (d) show the evolution of the $(\bar{1}\bar{1}7)$ *HOLZ line throughout the series. The colored dots in (a) and (b) denote the onset of HOLZ line splitting as shown in the corresponding panels labeled in (c) and (d)*

compared to the nanoribbon sample, as indicated by the arrows in Figure 4-7(a) and (b); however, the origin of this difference cannot be fully understood from these patterns alone.

To quantify and compare the HOLZ line splitting observed in each sample, kinematic simulations were used to approximate the width of each HOLZ band using a free-surface total relaxation assumption shown schematically in Figure 4-8(a). If the surface of the deformed lattice is assumed to be fully relaxed but tilted away from its original orientation by some angle $\theta/2$, diffraction from the sample then can be approximated as occurring from two pieces of strain-free material – the front and back surfaces – tilted with respect to one another about the [$\bar{1}$ 010] direction as indicated in Figure 4-5 by a total angle of θ [71]. Experimental patterns obtained far away from the HEMT interface were first matched to kinematic simulations to determine experimental parameters such as effective accelerating voltage, angle of convergence, etc. Using these parameters, two simulated sets of HOLZ lines were then superimposed upon one another to approximate the splitting observed in the experimental images, as illustrated in Figure 4-8(b). The shift in the HOLZ line patterns corresponds to the angle of rotation θ between the two surfaces of the sample and gives an indication of the level of strain relaxation. This method was used to generate splitting profiles for both the planar and nanoribbon samples [Figure 4-9(a)]. While the overall trends appear similar in both planar and nanoribbon samples indicating

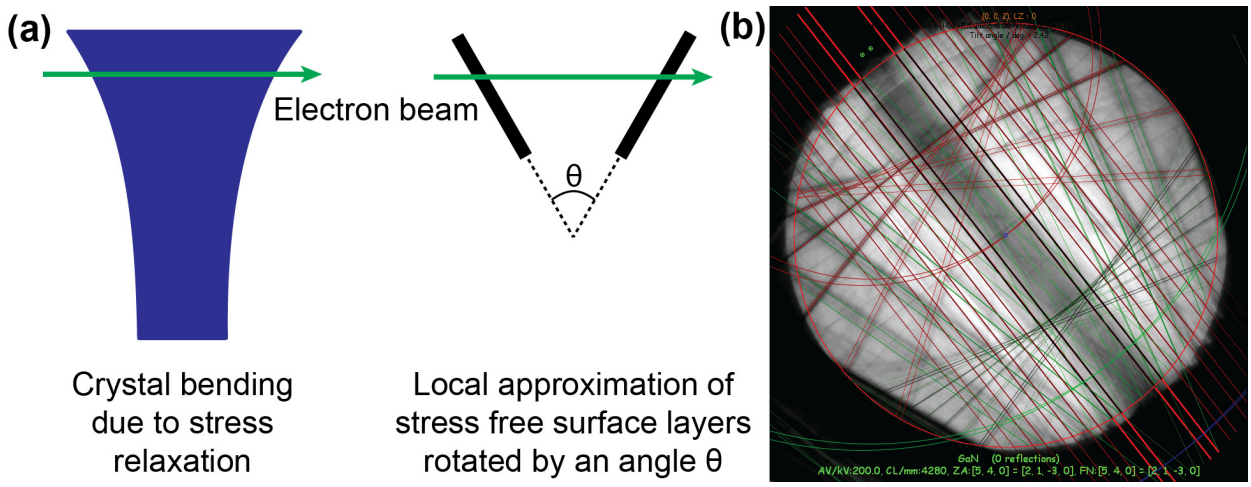

Figure 4-8. (a) Schematic illustration of the free-surface total relaxation assumption and the creation of a bi-crystal for the estimation of HOLZ line broadening shown in (b).

that the source of stress in both systems is the same, the magnitude of splitting in these two samples is different.

4.5. Finite element analysis of the HEMT structure

To understand these differences, we created 3D finite element models of the planar and nanoribbon TEM structures and calculated the stresses and strains resulting from the inherent lattice mismatch of each device layer. Figure 4-9(b) shows a schematic of the model consisting of a 200 nm fully-relaxed GaN substrate, 1 nm AlN barrier layer, and 8 nm $In_{0.17}Al_{0.83}N$ and 45 nm of Al_2O_3 corresponding to the samples used for CBED investigation. Orthotropic elastic constants used for the modeling were obtained from the experimental work summarized by Wright[75] and Vegard's rule of mixing was used to determine the elastic constants of the InAlN layer based on an In composition of 0.17%at. Similar to other studies[57], the lattice mismatch between each layer was modeled as a thermal expansion of each material with GaN as a reference and the stress in the system was assumed to be fully compensated elastically. Table 4-1 shows a summary of the elastic constants for the various materials used in the FEA analysis. Dimensions of each model were based upon those observed in TEM with the thickness obtained from dynamic CBED simulations.

Material	E_{11} (GPa)	E_{33} (GPa)	G_{44} (GPa)	G_{66} (GPa)	ν_{12}	ν_{13}	Lattice mismatch
GaN	324	356	105	123	0.323	0.198	0
$In_{0.17}Al_{0.83}N$	306	312	105	116	0.325	0.200	-0.0017
AlN	345	354	125	131	0.322	0.177	-0.0247
Al_2O_3	134	NA	NA	NA	0.22	NA	NA

Table 4-1. Summary of elastic constants used in FEA simulations of planar and nanoribbon HEMT structures.

4.5.1. Simulations of TEM thin films

To compare the FEA model with experimental results, splitting profiles were generated by measuring the angle of the model's deformed surface with respect to its original orientation.

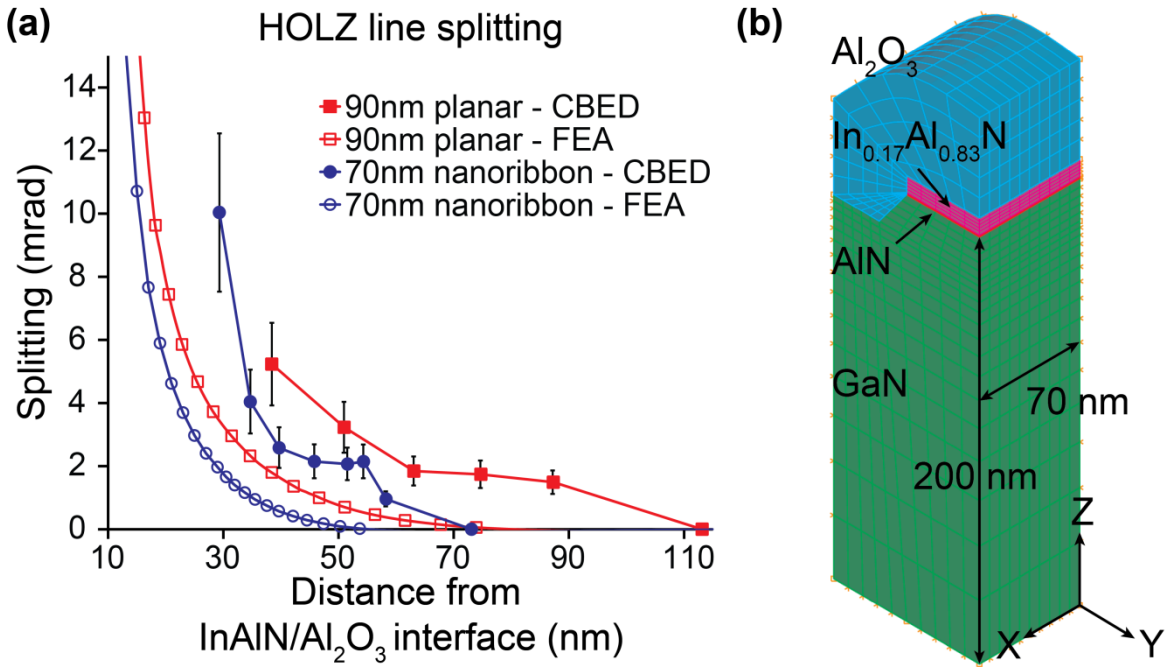

Figure 4-9. (a) Comparison of HOLZ line splitting approximations from both experimental series of CBED patterns and FEA calculations of planar and nanoribbon structures. (b) Illustration of the FEA model developed to simulate strain at the InAlN/GaN heterointerface of a nanoribbon structure.

These results are shown together with the experimentally measured splitting in Figure 4-9(a) and show that the FEA model correctly replicates the overall splitting behavior, but it consistently underestimates the magnitude of splitting observed experimentally. We suggest that this difference in magnitude could indicate a stress generated during the processing of the device structure that is not represented in the FEA model. Additionally, while no large regions of crystalline Al_2O_3 are observed, it is possible that small regions of crystalline material created by the electron beam could also induce additional stress in the system as previously suggested by BF-TEM. The model also highlights the importance of sample thickness showing that the difference between the planar (90 nm thick) and nanoribbon (70 nm thick) splitting profiles is due to the difference in sample thickness. This observation was also confirmed experimentally by obtaining splitting profiles from nanoribbon structures of differing thicknesses along a wedge-shaped sample in which stronger splitting behavior was observed to occur in thicker regions of the sample.

Besides splitting profiles, band plots of the strain components ε_{xx}, ε_{yy}, and ε_{zz} were also generated along a direction analogous to the electron beam path through the sample [Figure 4-10(a)]. These plots reveal the spatial distribution and magnitude of all three strain components and show that the variation of the ε_{zz} strain component is considerably higher than either the ε_{xx} or ε_{yy} components. Line scans of the strain components at 60 nm and 30 nm below the Al_2O_3/InAlN interface [Figure 4-10(b)] show that the total variation of ε_{zz} increases from 2.6×10^{-4} at 60 nm to 5.6×10^{-4} at 30 nm, which is 2 – 5 times greater than the variations observed for ε_{xx}

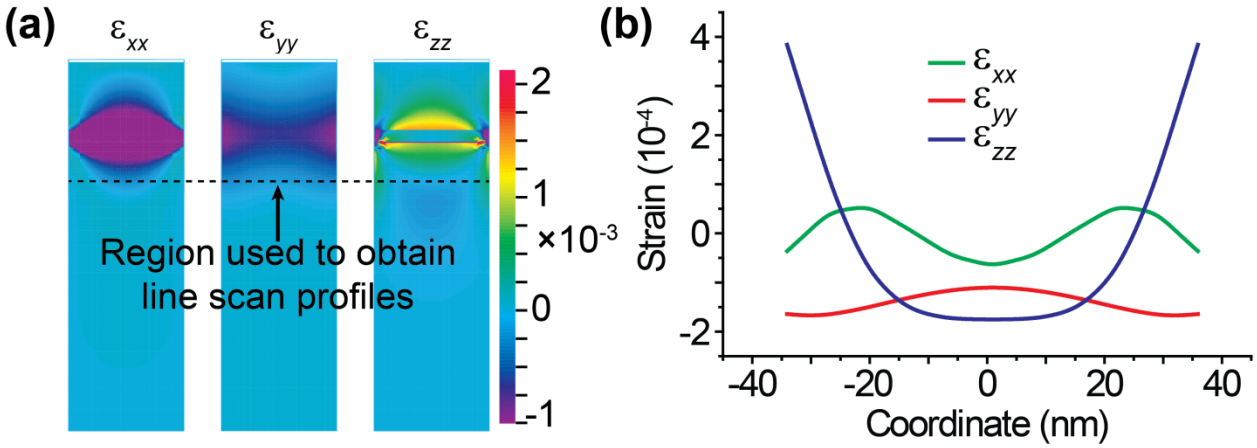

Figure 4-10. (a) Band plots of the three major strain components along the midplane of the FEA model. (c) Line scans of the strain components shown in (b) showing the variation along a path analogous to the beam direction.

(9.6×10^{-5} – 1.2×10^{-4}) and an order of magnitude greater than those for ε_{yy} (1.0×10^{-5} – 5.7×10^{-5}). The strong variation of the ε_{zz} strain component corroborates the CBED results and the observation that HOLZ lines highly indexed in the *c*-direction exhibit stronger splitting behavior.

4.5.2. Simulations of device-sized structures

Finally, using this FEA model, full device structures (as opposed to thin-film TEM foils described above) were modeled to investigate the role of nanoribbon fabrication and Al_2O_3 passivation on the stress state of the HEMT structure both along (σ_{xx}) and perpendicular (σ_{yy}) to the ribbon direction. It was observed from the model of the nanoribbon device that the largest variations in stress occurred along the σ_{yy} component, due to the fact that the greatest amount of stress relaxation will occur perpendicular to the newly created sidewall facets of the nanoribbon structure. The average σ_{yy} stress in the InAlN layer for both planar and nanoribbon structures is shown as a function of Al_2O_3 thickness in Figure 4-11. From these plots it can be seen that the

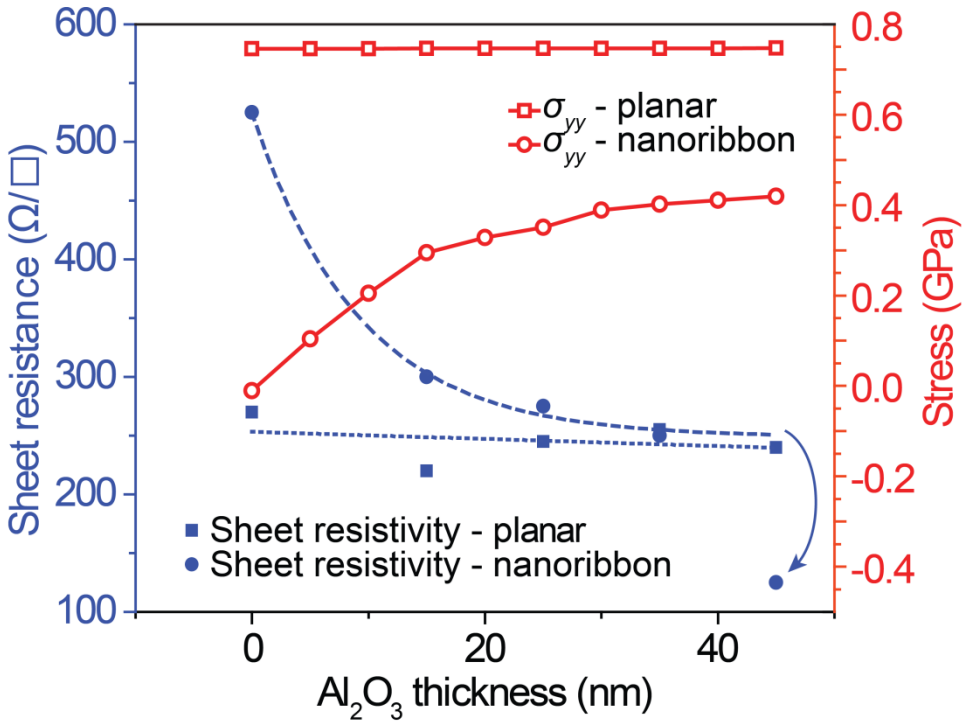

Figure 4-11. The average stress (plotted in red) in the InAlN layer is calculated from FEA for device sized structures and is plotted as a function of the thickness of the passivating oxide layer for both planar and nanoribbon structures. Sheet resistance data (plotted in blue) from our previous investigation is replotted for comparison. All lines are used as guides to the eye and emphasize the dramatic decrease in sheet resistance observed for the nanoribbon device at an Al_2O_3 thickness of 45 nm (indicated by arrow).

creation of a nanoribbon in a planar structure results in a compressive stress of approximately 10 MPa. The application of an oxide layer releases this compressive stress and introduces a tensile stress that increases up to 420 MPa as the thickness of the oxide covering the HEMT layers increases. The σ_{xx} component (not shown) exhibits a similar trend though the stress remains tensile and the total change in magnitude is smaller, varying only from 460 MPa with no passivating oxide layer to 623 MPa for a 45 nm thick layer. In contrast to the nanoribbon structures, the predicted stress, σ_{yy}, of the planar device is on the order of 745 MPa and only increases slightly with oxide thickness in a linear fashion [Figure 4-11]. The compressive strain that is observed in the unpassivated nanoribbon is the result of a new free surface that allows for relaxation of the biaxial tensile stress that is generated in the thin film due to mismatch between AlN and InAlN. Applying a layer of Al_2O_3 restricts the amount of relaxation along this free surface reintroducing a tensile stress that increases with increasing Al_2O_3 thickness.

These trends in stress observed for both the planar and nanoribbon structures correlate well with the observed sheet resistance trends of the sample presented elsewhere [24] and plotted in Figure 4-11. Due to its piezoelectric nature, a tensile stress has been predicted to increase the concentration of electronic carriers in InAlN while a compression stress will cause a decrease in concentration. Therefore, based upon the trends in stress observed for the nanoribbon structure, it can be predicted that the electronic carrier concentration for an unpassivated nanoribbon device will be relatively low, resulting in a high sheet resistance, and will increase with increasing oxide thickness thus lowering the measured sheet resistance. However, the FEA model does not explain the dramatic decrease in sheet resistivity that is observed for large thicknesses of oxide (>45 nm). This sudden decrease in resistivity could be the result of the oxide layer coalescing creating an increased tensile stress in the InAlN layer in a manner similar to what has been observed for the coalescence of Volmer-Weber grown thin films [76]. It also stands to reason that the nominal structure that was used in modeling the HEMT system is not the actual structure that exists prior to device processing. The various series of processing steps including several high temperature anneals, could change the composition of the active layers directly affecting the strain in the system. Furthermore, despite its great versatility and characterization powers, CBED is a time intensive technique that is not best suited for samples requiring routine characterization. The nature of acquiring and analyzing CBED patterns also makes mapping strain in 2D impractical. It will, therefore, be ideal to identify complimentary techniques that can more

quickly provide similar strain information on the nanoscale. In the next chapter, we will explore the use of nanobeam electron diffraction and geometric phase analysis and demonstrate the ability of these techniques to provide further insights into the strain state of the material and the effects device processing may have on the HEMT structure.

4.6. Conclusions

In conclusion, we have demonstrated in this chapter the combined use CBED and FEA to investigate the stress state of both planar and nanoribbon structured HEMT devices with nanoscale resolution. Kinematic simulations were used to measure amount of HOLZ line splitting in diffraction patterns obtained near the HEMT interface revealing a significant strain gradient along the [001] direction and generating profiles that could be compared to results from the FEA models, which suggest additional sources of stress not represented in our current models. Band plots and line scans of the ε_{xx}, ε_{yy}, and ε_{zz} strain components demonstrated the ability of the FEA model to correctly replicate the general splitting behavior observed experimentally. Finally, device structures were simulated to show the relationship between oxide layer thickness and stress state of the active InAlN HEMT layer which was then shown to be useful in explaining previously observed trends in sheet resistivity of the devices. Additionally, the techniques and methods used in this investigation can be applied to a much wider array of nanoscale materials in which stress and strain are traditionally challenging to characterize.

Chapter 5. Towards rapid nanoscale measurement of strain in III-nitride heterostructures

In this chapter, we report the structural and compositional nanoscale characterization of InAlN/GaN nanoribbon-structured high electron mobility transistors (HEMTs) through the use of nanobeam electron diffraction (NBED) and geometric phase analysis (GPA). The strain distribution in the HEMT layer is quantified and compared to the expected strain profile for the nominal structure predicted by finite element analysis (FEA). Using the experimental strain results, the actual structure is determined and used to refine the FEA model. The improved fit of the model demonstrates that GPA and NBED provide a powerful platform for routine and rapid characterization of strain in III-V semiconducting device systems leading to insights into device evolution during processing and future device optimization.

5.1. Introduction

The InAlN/GaN system has previously been introduced in Chapters 1 and 4 as well as its importance in the fabrication of high-power, high-frequency optoelectronic devices. Their high direct-band gaps and carrier mobilities make these materials ideal candidates for the realization of HEMT. In the previous chapter, we also demonstrated how the fabrication of nanoribbon structures in the channel region of an InAlN/GaN HEMT device allowed for the enhancement of device operation through strain engineering. Through the use of CBED and FEA, stress in the active layers of the InAlN/GaN HEMT nanoribbon structured device was directly correlated to sheet resistivity data [77]. These results demonstrated the promise of strain engineering of these devices making the nanoscale characterization of strain a primary concern for future optimization. However, while these results showed CBED to be a powerful technique for the local characterization of strain having high spatial resolution on the order of 1 nm and strain sensitivities as high as 10^{-4}, CBED was shown to be a time consuming technique and requiring a significant amount of data analysis and simulation to properly interpret the results. It is consequently not suitable as a routine technique for strain quantification. Techniques that can provide strain information more readily with less data processing are therefore needed. Such a platform for strain quantification will be important not only for the InAlN/GaN system presented

in this investigation but for a larger range of III-V nanostructures that are continually becoming more prominent in the design of advanced optoelectronic devices.

In this chapter, we explore the use of two complementary transmission electron microscopy (TEM) techniques for the characterization of strain in InAlN/GaN nanoribbon structured HEMTs and show that they provide a platform for rapid strain investigations in III-V nanostructured devices: nanobeam electron diffraction (NBED) and geometric phase analysis (GPA). Energy dispersive X-ray spectroscopy (EDS) was used to provide complementary information about the HEMT layer compositions. The results are compared to one another in their ability to measure both the magnitude and shape of the strain field around the HEMT layers. FEA simulations of the strain fields were generated based on the information from the strain measurement techniques to reveal significant deviations in the HEMT device from the nominal structure. Together, these techniques reveal the importance of understanding structural changes during device fabrication and demonstrate the methods that can be used to characterize strain at the nanometer scale.

5.2. Experimental setup and characterization techniques

Nanoribbon HEMT structures were fabricated through a top-down process previously described in Chapter 4 and elsewhere [24, 77]. The nanoribbon structures consist of a ~1.8 μm thick Fe-doped GaN buffer layer grown on SiC along the ⟨0001⟩ direction, a ~1 nm AlN spacer layer, and finally a ~7 nm barrier layer of $In_{0.17}Al_{0.83}N$ (nominal composition). As-grown layers were subjected to standard device fabrication steps including mesa isolation and ohmic contact fabrication at high temperature (870^{o} C). Nanoribbons were then defined between the source and drain contacts of a number of devices using electron beam lithography and fabricated using low-power electron cyclotron resonance reactive ion etching. Ribbon structures were fabricated and imaged along the $[11\bar{2}\,0]$ direction with [0002] and $[0\bar{1}\,10]$ being the growth and in-plane direction, respectively. A conformal passivation layer of Al_2O_3 was deposited on the surface using atomic layer deposition with thicknesses ranging from 0 – 45 nm. TEM samples were obtained from the region between the source and drain contacts using a FEI Strata 400 focused ion beam (FIB). An approximately 2 μm thick tungsten layer was deposited during FIB preparation to protect the HEMT layers from the damaging effects of the Ga beam during course milling at 30 kV. Final thinning of the sample was performed at 8 kV to ensure a high quality

surface for TEM (less than 10 nm surface amorphous layer [78]) while maintaining the parallel sides of the TEM sample that are optimal for strain mapping. Figure 5-1 shows a typical example of the nanoribbon structures examined with a magnified image of the HEMT structure seen in the inset. All experiments in this chapter were performed at the MINATEC campus of the CEA in Grenoble, France.

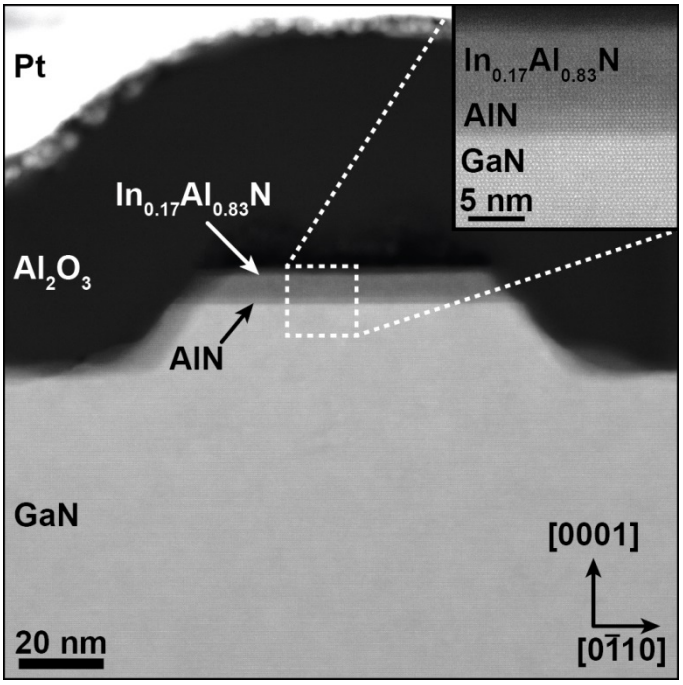

Figure 5-1. HAADF-STEM image of a typical nanoribbon structure studied in this investigation with the important HEMT layers labeled with their nominal compositions. A detail image of the HEMT layers is shown in the top inset while the bottom inset shows a schematic illustration of multiple nanoribbon structures in cross-section.

5.2.1. Nanobeam electron diffraction

As discussed in Chapter 2, NBED is a TEM based technique that analyzes changes in diffraction patterns obtained from strained and unstrained regions of the sample. In contrast to CBED which uses a converged electron beam to produce HOLZ line patterns, NBED uses a highly focused parallel beam of electrons to produce spot patterns from local regions of the sample. Additionally, NBED patterns are typically obtained along a low-index zone axis which will reduce the projection effects observed in CBED due to the tilting away from the major zone axis. Due to the parallel nature of the nanobeam, the diffraction pattern along a low-index zone axis will be free of dynamic effects that appear in CBED patterns.

With the proper choice of condenser aperture and lens arrangements spot sizes of 3 to 5 nm with low convergence angles can be readily achieved. Both the spot size and convergence angle play an important role in determining the spatial and strain resolution of the obtained data. As it would be expected, a larger spot size means a lower spatial resolution as the resultant diffraction pattern is generated from a larger volume of material. Therefore, to achieve the highest spatial resolutions, smaller spot sizes are desirable. Smaller spot sizes can be readily achieved with increased convergence angles (high convergence angles in CBED allow for spot sizes of 1 nm); however, as convergence angles increase, the discrete spots of the diffraction pattern begin to broaden creating a CBED pattern. These broader spots will decrease the strain resolution through an increase of dynamical effects and the presence of HOLZ lines. As a general rule, a convergence angle less than 1 mrad is needed for the accurate determination of diffraction spots [79]. Therefore, the hardware of the TEM – specifically the condenser lenses and apertures – becomes important in determining the final spatial and strain resolutions achievable. Using very small condenser apertures (1 μm), spot sizes on the order of 10 nm with convergence angles of 0.14 mrad have been achieved [79]; however, this small of an aperture must be custom made and limits the intensity of the probe. It has also been shown that with the use of a third condenser lens, a 5 nm probe with a convergence angle of 0.5 mrad can be formed using a 50 μm aperture increasing spatial resolution and probe current while maintaining high strain sensitivity (6×10^{-4}) [44, 80].

NBED's greatest advantage over CBED is the fact that much less data processing is required to determine strain values from an NBED pattern than from the higher order Laue zone (HOLZ) line patterns that are acquired from CBED. In this study, strain is determined using the method described by Béché *et al.* [44]. Spots in each NBED pattern are first located and their precise positions calculated by fitting each spot with a 2D Gaussian function. Spots are then manually chosen and their *g*-vectors (g_1 and g_2, for example) are placed into the reciprocal matrix $\boldsymbol{G}$.

$$\boldsymbol{G} = \begin{bmatrix} g_{1x} & g_{2x} \\ g_{1y} & g_{2y} \end{bmatrix} \tag{5-1}$$

The distortion matrix, $\boldsymbol{D}$, can then be calculated by

$$\boldsymbol{D} = (\boldsymbol{G}^t)^{-1}\boldsymbol{G}_0^t - \mathbb{1} \tag{5-2}$$

where $\boldsymbol{G_0}$ is the reciprocal matrix of the NBED pattern measured in the reference material and $\mathbb{1}$ is the identity matrix. Having calculated $\boldsymbol{D}$, the strain ($\boldsymbol{\mathcal{E}}$) and rotation ($\boldsymbol{\Omega}$) matrices are calculated by

$$\mathcal{E} = \frac{1}{2}(\boldsymbol{D} + \boldsymbol{D}^t) \qquad (5\text{-}3)$$

$$\boldsymbol{\Omega} = \frac{1}{2}(\boldsymbol{D} - \boldsymbol{D}^t) \qquad (5\text{-}4)$$

Using this method, it has been demonstrated that strains can be measured with an accuracy on the order of 10^{-4} [44]. In this investigation, NBED patterns were acquired using a probe-corrected FEI Titan operated at 300 kV. Patterns were obtained using a 5.5 nm probe with a semiconvergence angle of 0.5 ± 0.05 mrad along the [11$\bar{2}$0] zone axis.

5.2.2. Geometric phase analysis

As previously described in detail in Chapter 2, GPA is another technique suitable for nanoscale strain characterization in which an atomically resolved image is separated into amplitude and phase images through the selection of specific *g*-vectors in Fourier space [45, 46]. The phase image can then be used to generate a strain map by analyzing the variation in phase with respect to a defined, unstrained reference area. GPA of both high resolution TEM (HRTEM) and lattice resolved scanning TEM (STEM) images have been shown to be useful in quantifying strain in nanostructures with spatial resolutions of a few nanometers [48]. However, STEM images offer an advantage over HRTEM for GPA as they are less sensitive to variations in sample thickness and can be used for samples that would generally be too thick for HRTEM analysis. From these techniques, it has been shown that strain can be measured in devices with spatial resolutions in the range of 1 – 5 nm with standard deviations of 0.15% - 0.32% for total strains as low as 1.4% [48]. Lattice-resolved high angular annular dark field (HAADF) STEM images for GPA and EDS line scans were acquired using a double C_S-aberration corrected FEI Titan Ultimate TEM operated at 200 kV. Lattice resolved images were acquired with the scan direction oriented along the [0002] growth direction, and subsequently the [0$\bar{1}$ 10] in-plane direction to eliminate scanning artifacts that arise in GPA strain maps obtained from STEM [48].

5.3. Strain analysis by nanobeam electron diffraction

NBED analysis was first performed by scanning a 5.5 nm nearly parallel electron beam [Figure 5-2(a)] across the HEMT structure. We obtained three line profiles, each consisting of one hundred NBED patterns, from three different ribbon structures [inset of Figure 5-2(c)]. By comparing each pattern along the line scan to the reference pattern [Figure 5-2(b)], strain values were calculated from the shifts of the diffraction spots as described above. Figure 5-2(c) shows the three studied ribbon structures and their corresponding strain profiles. The profile indicates

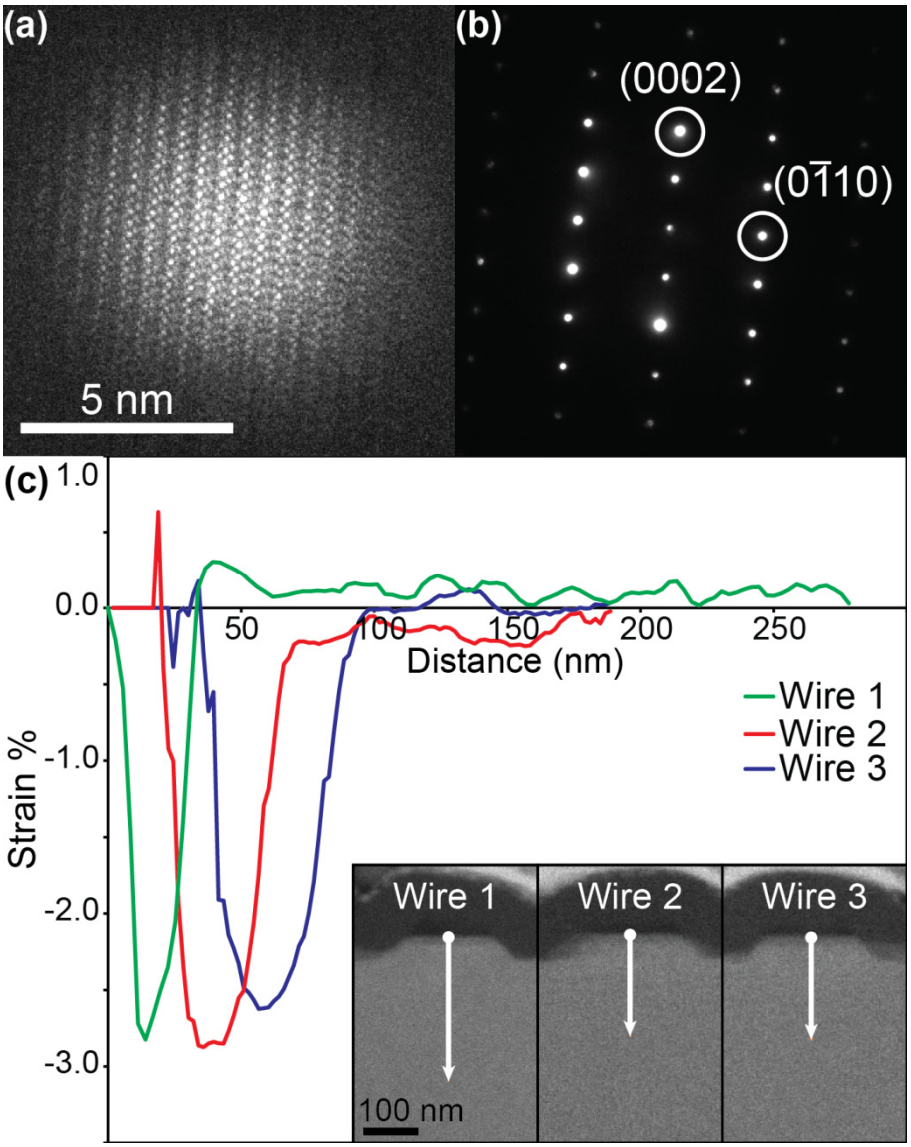

Figure 5-2. A 5.5 nm probe shown in (a) was used to produce NBED patterns along the [11$\bar{2}$0] zone axis, such as the reference pattern seen in (b). The growth-direction strain profiles obtained from NBED for the nanoribbon HEMT structures seen in the inset are presented in (c).

an average maximum strain in the HEMT layer of -2.7% ± 0.1% relative to the GaN substrate. While this strain value seems quite high for a material assumed to have no plastic relaxation, it should be remembered that this strain value is measured with respect to the GaN substrate and not the relaxed state of the HEMT layer. Based on our previous discussion of Lagrange strain in Chapter 3, we can calculate a material strain of -0.47%. However, the Lagrange strain will be a more convenient value to use to compare experimental and FEA results and will therefore be used throughout this discussion.

The strain profiles obtained from NBED have slightly larger full-widths at half-max (FWHM) (11 nm for Wire 1) compared to the thickness of the HEMT layer measured from lattice-resolved STEM images [Figure 5-2(d)]. This broadening of the profiles is most likely due to convolution of the 5.5 nm probe with the sample. This convolution occurs simply due to the size of the probe. Close to the heterointerface, the probe will sample both strained and unstrained material returning and averaged result. This averaging will act to broaden the strain profile by artificially increasing the strain signal in the material close to the heterointerface. Alternatively, sample drift could also provide a source of profile broadening as the FWHM is observed to increase – about 16 nm for Wires 2 and 3 – with longer acquisition times in the HEMT layers. Each line scan consists of 100 NBED patterns each taken with the acquisition time. As a result, the total time to obtain a line scan of NBED patterns is constant regardless of the length of the line. Therefore, for shorter lines (like those for Wires 2 and 3) the probe will move more slowly and thereby exaggerating any sample drift that might be present during the acquisition.

5.4. Strain analysis by geometric phase analysis

While NBED is ideal for providing highly precise measurements of the strain in the HEMT structure, it is generally limited to linescans as mapping often requires lengthy acquisition times and can be limited by sample drift. Therefore, to obtain an overview of strain throughout the whole structure, GPA was used to produce strain maps from lattice resolved HAADF STEM images. GPA strain maps of the HEMT structure were produced using a custom software package developed by Jean-Luc Rouvière based the methods discussed in Chapter 2 and elsewhere [46]. The process is outlined in Figure 5-3. First, a fast Fourier transform (FFT) [Figure 5-3(b)] image was generated from the HAADF image [Figure 5-3(a)]. By multiplying the FFT image by Gaussian masks, two non-collinear *g*-vectors were selected in order to calculate

strain maps in both the growth and in-plane directions. The spatial resolution of the resulting GPA map will be dependent on the size of the Gaussian mask used to select each *g*-vector. This can be seen if we consider the use of a Gaussian function in reciprocal space of the form:

$$\tilde{F}(g) = \exp\left(\frac{-(g-g_i)^2}{2\sigma^2}\right) \qquad (5\text{-}5)$$

where g_i is the center of the Gaussian function. The radius is therefore about $r_{rec} = 3\sigma$. The multiplication of a Gaussian in reciprocal space is equivalent in direct space to a convolution by the inverse Fourier transform of $\tilde{F}(g)$, $F(g)$ given by

$$F(x) = \sqrt{2\pi}\sigma \exp(-2\pi^2\sigma^2x^2)\exp(-2\pi g_i x) \qquad (5\text{-}6)$$

Therefore, the region in direct space which is being averaged is given by $r_{dir} = 3/2\pi\sigma$. If we then calibrate our image in pixels this equation becomes

$$r_{dir} = {}^{3N}/_{2\pi\sigma_p} \qquad (5\text{-}7)$$

where N is the size of the image in pixels and σ_p is now also measured in pixels. Equations 5-5 through 5-7 show how by changing the size of the Gaussian mask, we can control the size of the area over which the strain is convoluted, or averaged, in our GPA calculation. This area of averaging is what we will define here as spatial resolution. While higher spatial resolutions are generally desirable, higher resolution GPA strain maps are more susceptible to noise. In general, the minimum r_{dir} is given by $2d$ where d is the period of the direct space signal (lattice spacing). Therefore, it is good practice to generate several GPA maps of varying spatial resolution. The benefits of this practice will be demonstrated shortly.

In our calculations of strain, we used the (0002) and ($0\bar{1}$ 11) vectors as they have the highest intensities in the FFT image and thus reduce the noise in the strain map. From each *g*-vector, raw amplitude and phase images were calculated as shown in Figure 5-3(c) – (f) as described in Chapter 3. Each phase map is used to calculate a displacement field. By defining a reference area, the displacement maps can be used to calculate the strain in both the in-plane and growth directions across the whole image. While the amplitude image does not contribute to the strain calculation, it is important to note that GPA strain maps can only be interpreted if the amplitude is sufficient. From Figure 5-3(e) and (f) it can be seen that the amplitude throughout most of the sample is sufficiently high enough to produce interpretable strain maps but steeply

drops off above the HEMT layer meaning that any strain information in this area is unreliable. Finally, two strain maps were produced in the growth direction [0002] [Figure 5-3(g)] and the in-plane direction [$0\bar{1}\,10$] [Figure 5-3(h)] with spatial resolutions of 3 nm. For more details concerning the GPA calculation the reader is referred to Chapter 2 of this text and to literature [45, 46].

Figure 5-3(g) shows the strain along the growth direction and indicates a distinct change in the strain at the HEMT layers. While the noise in the GaN layer seems relatively low, the noise in the strained HEMT region is much more pronounced with some regions indicating levels of strain on the order of -10% relative to the GaN. The source of this noise, however, is not apparent from this strain map. One possibility is that the HEMT layer contains a significant number of defects which will contribute to the noise. Along the in-plane direction [$0\bar{1}\,10$], however, no discernible change in the lattice spacing between the substrate and HEMT layers was observed [Figure 5-3(g)]. This important observation indicates that the HEMT layer is in perfect epitaxy with GaN substrate and is under a tensile stress given the negative strain along the growth direction as dictated by the Poisson relationship. If the HEMT layer had been fully relaxed due to the formation of defects, a similar negative strain would have been observed in the in-plane direction [48]. Therefore to investigate the nature of this noise and better measure the strain along the growth direction, strain maps of varying spatial resolutions were produced.

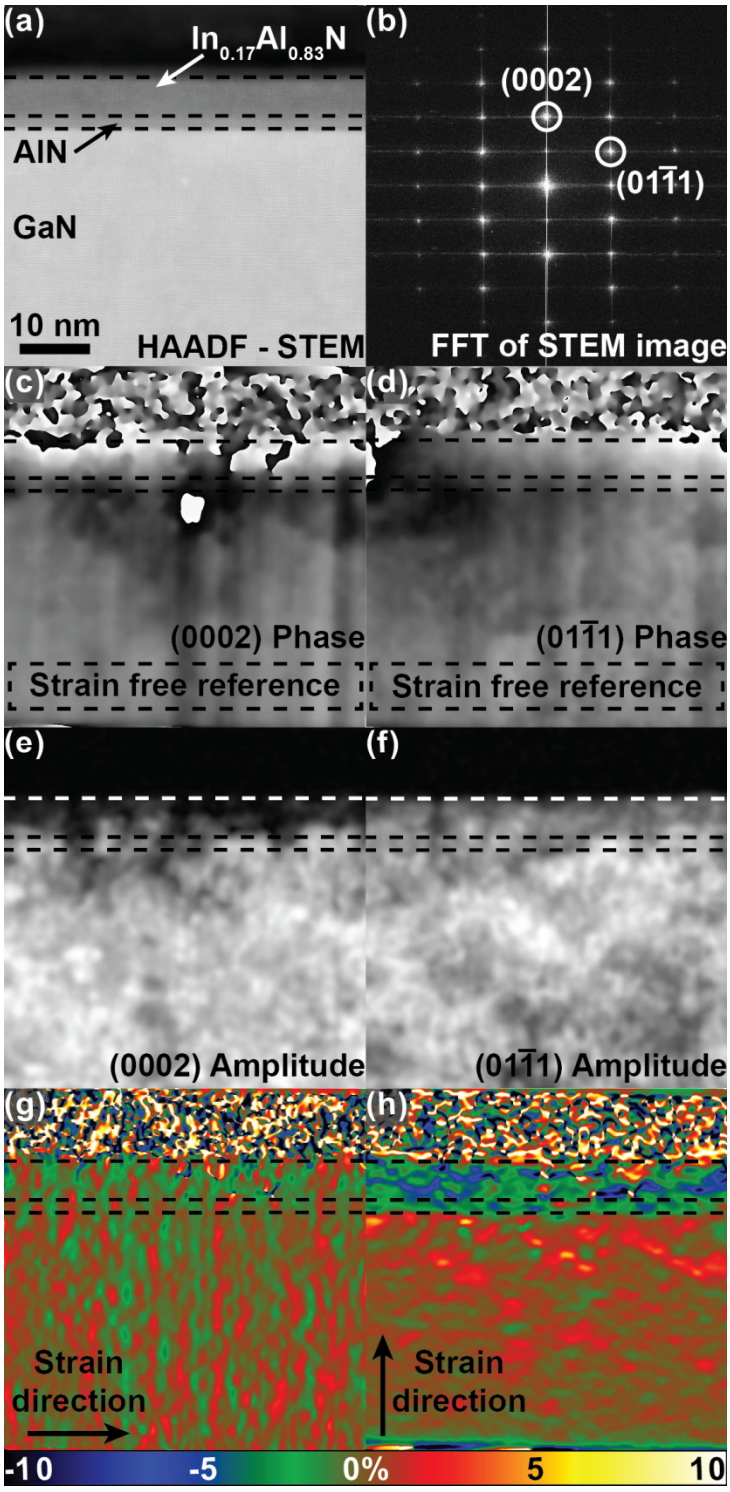

Figure 5-3. (a) HAADF STEM image of HEMT structure used to create GPA strain maps. The g-vectors (0002) and (0$\bar{1}$ 11) are first selected from a FFT image (b). Raw phase and amplitude images are calculated from each vector and shown in (c) – (f). Strain maps are calculated for both the growth direction (g) [0002] and the in-plane direction (h) [0$\bar{1}$ 10] with the scale shown to the far right.

As previously discussed, producing strain maps of varying spatial resolution allows for the best determination of both the shape and magnitude of a strain field within a structure [48]. Therefore, strain maps with spatial resolutions of 5 nm and 2 nm [Figure 5-4(a) and (b), respectively] were produced from the same HAADF image [Figure 5-3(a)] using different sizes of Gaussian mask to the select the *g*-vectors, as described earlier. Line profiles [Figure 5-4(c)] integrated over the whole field of view were extracted from each map as indicated in Figure 5-4(a) and show that at lower resolutions the noise in the strain profile is greatly reduced, leading to an improved measurement of strain magnitude in the HEMT layer, whereas higher resolution maps exhibit higher levels of noise but are more suitable for resolving the sharp change in strain value at interface between the GaN and HEMT layers. Therefore, from the strain maps generated with a 5 nm spatial resolution, an average strain value of -2.7% is obtained in the HEMT layer, in agreement with NBED measurements, with a root-mean-squared (RMS) value of 0.5%

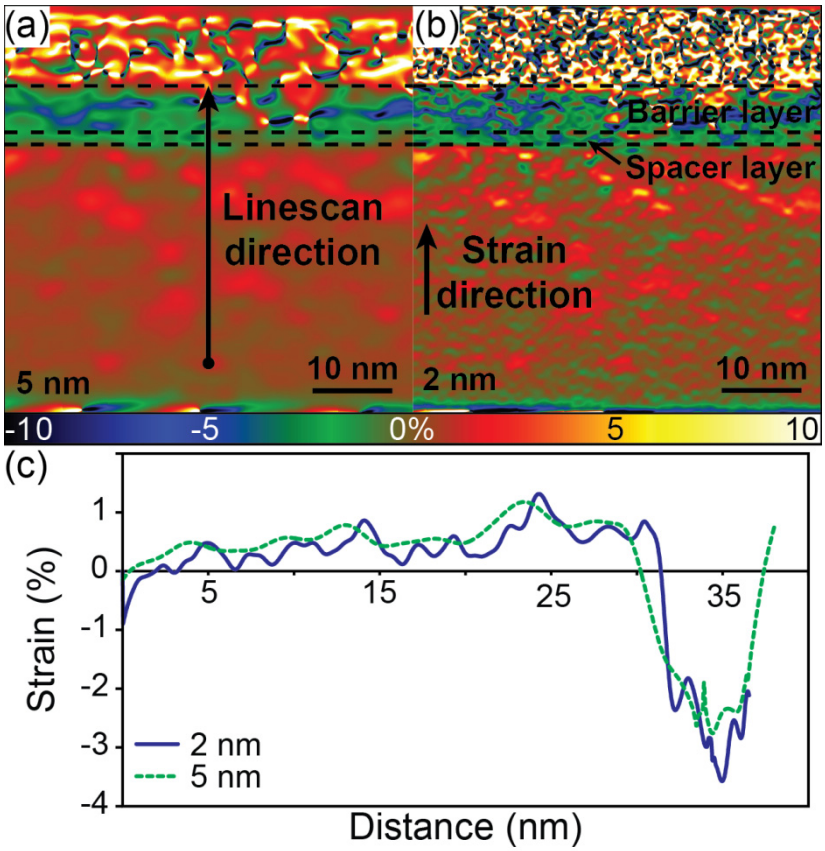

Figure 5-4. Growth-direction strain maps with spatial resolutions of (a) 5 nm and (b) 2 nm generated from the HAADF STEM image shown in Figure 5-3(a) with the strain scale indicated at the bottom. (c) Linescans are obtained from each image as indicated in (a) and integrated over over the whole field of view.

measured in the bulk while the 2 nm spatial resolution map indicates the sharp nature of the change in strain at the interface.

Both of these images, however, still exhibit the high levels of noise associated with the HEMT layers. Therefore, in order to determine the cause of this noise we examined the lattice-resolved STEM image in these areas. The image is examined first by calculating a strain map over the image and overlaying it on top of the STEM image [Figure 5-5(a)]. Examining the lattice in regions of high noise shows that the atomic columns in these areas are much more blurred than the bulk of the sample [Figure 5-5(b)]. This blurring could be the result of large deformations that occur at the HEMT layer as demonstrated by our previous CBED measurements (Chapter 4). Additionally, this deformed region could be more sensitive to FIB milling resulting in regions of amorphized material. Examining regions of the HEMT layer where the atomic columns are not blurred, we measure average strain values of -2.7% in agreement with our previous results.

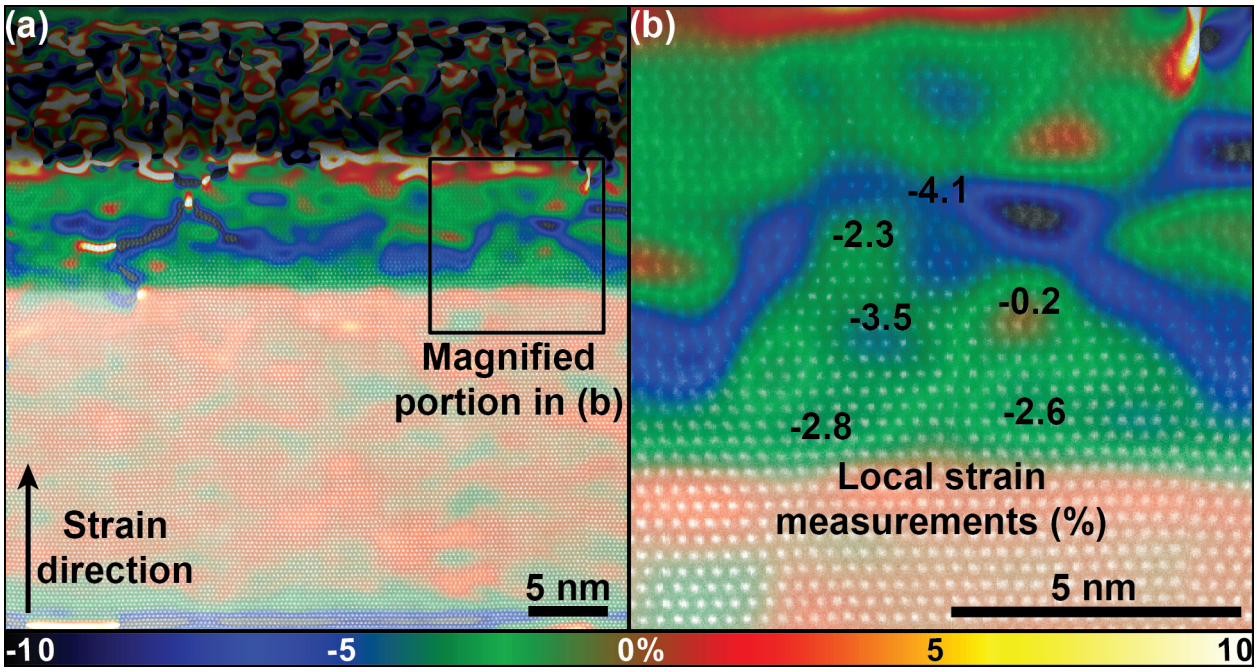

Figure 5-5. (a) Overlay of a GPA strain map on a lattice resolved STEM image.(b) A magnified portion of the HEMT region indicated by the box in (a) showing the measured strain values in percent at those locations.

5.5. Finite element analysis

Finally, we compared as-obtained line scans from the GPA strain maps and NBED to the strain profile calculated based on the FEA simulations of the nominal HEMT structure and observed they differ significantly in both the magnitude and shape [Figure 5-6(a)]. FEA simulations based on the nominal structure exhibits a double peak structure with a strain (relative to GaN buffer) of -5.26% in the spacer layer and -1.62% in the barrier layer, whereas experimental results exhibit a single peak with a value of -2.7% throughout the whole structure. To investigate origin of this discrepancy, we note that the contrast in the HAADF image (Figure 5-6, inset) does not correspond to the nominal composition of the GaN/AlN/$In_{0.17}Al_{0.83}N$ layers (the middle AlN spacer layer is brighter than the top $In_{0.17}Al_{0.83}N$ barrier layer despite the fact that the average atomic number of the barrier layer is higher and hence should produce a brighter image) [81]. This inversion of contrast suggests that intermixing of layers most likely occurred during the high temperature device fabrication steps, as previously mentioned.

By using linear elastic theory as discussed in Chapter 3, we estimated that the In composition needed to achieve a strain value of -2.7% in the InAlN barrier layer relative to the GaN buffer layer should be 12% at [80]. To experimentally verify this estimate, we obtained EDS line scans over the thickness of the barrier and spacer layers which reveal significant differences in composition compared to the nominal values (Figure 5-7). Figure 5-7(a) shows the raw intensity of the Al, Ga, and In signals starting in the passivating Al_2O_3 layer and ending just below the spacer layer in the GaN buffer layer. These plots suggest that some Ga from the buffer layer and In from the barrier layer may have diffused into the spacer layer. Figure 5-7(b) displays the quantification of those points within the HEMT structure performed using the built-in quantification tools of the TIA software package. These results support the 12%at In predicted in the barrier layer by linear elastic theory and also show a concentration of Ga in the spacer layer of approximately 30%at though Ga concentrations in the barrier layer are negligible.

Using these new composition values, the FEA model was modified to consist of a 1.5 nm spacer layer of $In_{0.05}Ga_{0.30}Al_{0.65}N$ and a 5.5 nm $In_{0.12}Al_{0.88}N$ barrier layer. This refined model provides a significantly improved fit with the experimental results exhibiting a strain of -2.54% in the spacer layer and -2.66% in the barrier layer [Figure 5-6(b)]. However, we note that the FEA model still contains discrepancies such as sharp corners that are most likely the result of chemical grading in the actual structure or convolution with the electron beam that is not captured by our model. Taken together, our results indicate that there is significant drop in In composition in the barrier layer and understanding its origin will prove vital in future device optimization. While it has been shown that a tensile stress, like that seen in the present HEMT structure, can increase carrier concentrations in the GaN channel,[21] further decreases in In

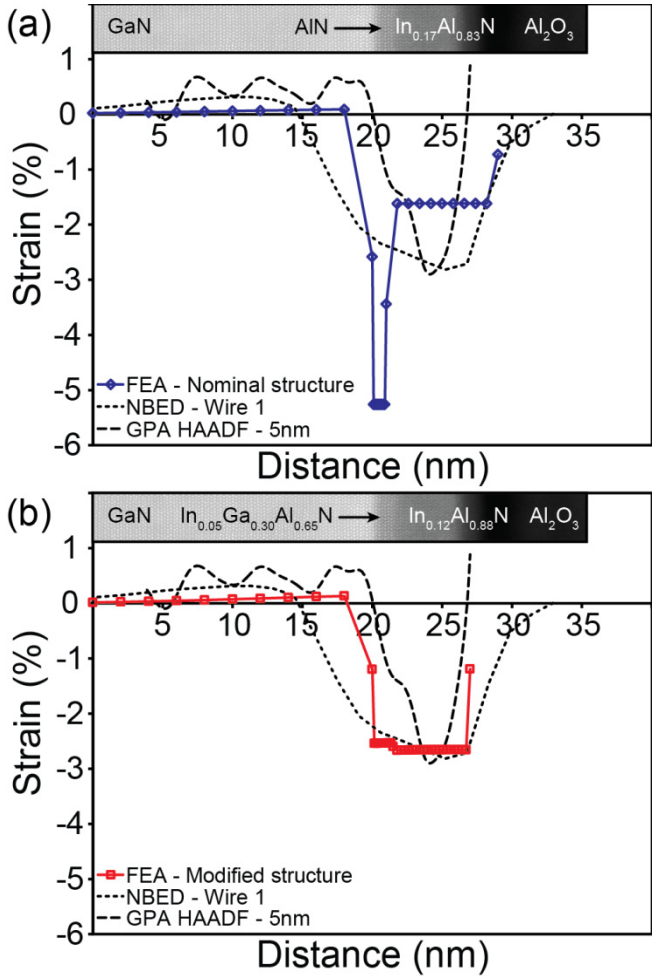

Figure 5-6. A summary of strain profiles generated using GPA, NBED, and FEA simulations for both the (a) nominal and (b) calculated chemistries. The inset shows a scaled cross section of the HEMT structure.

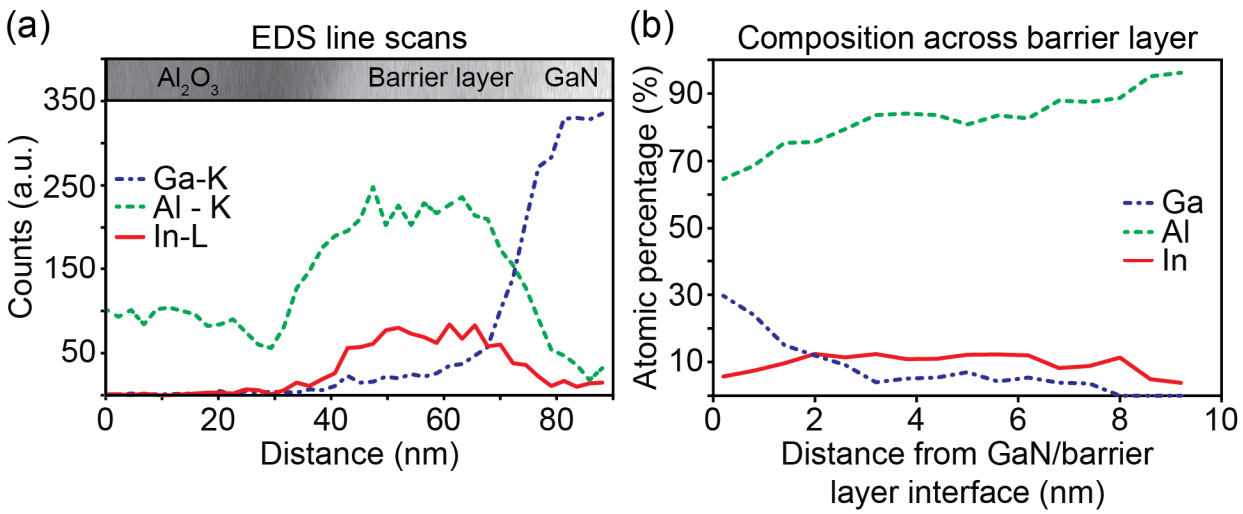

Figure 5-7. Summary of EDX linescan data obtained from the HEMT structure showing (a) the intensity profiles for Ga, Al, and In. The quantified results throughout the barrier and spacer layers are shown in (b).

composition could create strains high enough to induce defect formation. Moreover, these results highlight the importance of strain characterization in any layered system where changes in layer composition will have effects on the strain state of the system. As it has been discussed, these changes that may occur during processing can have significant effects on the properties and performance of the final device. By understanding how the strain state changes and how it can be controlled, novel routes to tune device characteristics can be achieved through strain engineering.

5.6. Conclusions

Based on the results from this chapter and the previous chapter, we can identify the strengths and weaknesses of each strain characterization technique. Table 5-1 summarizes some of the more important figures of merit of each characterization technique used in this study including spatial and strain resolutions, level of data processing required to interpret results, requirements on the sample for proper imaging, and what kind of data can be produced. From this summary, we can now begin to identify which technique will be the best suited to our specific application based on the situation's constraints. For example, in the following chapter we will seek to characterize strain in III-V semiconducting core-shell nanowires. Due to the complex, 3D heterointerface it is unlikely that the heterostructures will contain any strain free reference material. Therefore, we can say that CBED will be the most suitable technique for this situation.

Technique	Spatial resolution	Strain resolution	Data processing required	Need of reference area	Sample requirements	Result type
CBED	1 nm	10^{-4}	High	Not required	~ 200 nm thick	Profile
NBED	3 nm	1×10^{-3}	Moderate	Required on sample	< 200 nm thick	Profile
STEM-GPA	2 nm	5×10^{-3}	Low	Required in image	< 100 nm thick	Map

Table 5-1. Summary of strain characterization techniques used in this investigation highlighting their various strengths and weaknesses

In this chapter, GPA and NBED were used to measure and map the strain in InAlN/GaN nanoribbon structured HEMT devices providing insights to changes that occur on the nanometer scale within the device during fabrication. NBED was shown to accurately measure the magnitude of the strain in the HEMT structure but suffered loss of spatial resolution and broadened strain profiles due to beam convolution and sample drift. While GPA was better at producing an accurate shape of the strain profile, it was more sensitive to out-of-plane deformations creating increased levels of noise in the strain measurement. Nevertheless, these two methods present a powerful set of tools for the rapid characterization of strain in compound semiconductor nanostructured systems that present significant challenges for standard bulk characterization techniques.

Furthermore, while this chapter and the previous chapter have focused on devices of a simple planar geometry, the understanding of strain is no less important for the fabrication and use of more complex 3D heterointerfaces that are common in structures such as core-shell nanowires. The following chapter will demonstrate how the techniques developed and explored in these past two chapters can be readily applied to the nanoscale mapping of strain in core-shell nanowire heterostructures providing new insights and opportunities for device design.

Chapter 6. Quantification of stress and strain in GaAs based core-shell nanowire heterostructures

In this chapter we extend the previous discussion of heterointerface strain characterization to the case of a heterointerface that is wrapped upon itself in the form of a core-shell nanowire heterostructure. We demonstrate that this unique geometry creates novel, and sometimes unexpected, behavior of the strain fields. More importantly, by using a combination of convergent beam electron diffraction and finite element analysis, this behavior can be predicted demonstrating both the power of electron microscopy as a platform for nanoscale strain characterization and the reliability of FEA continuum models to accurately calculate complex strain fields

6.1. GaAs/GaAsP nanowire heterostructures

As it has already been discussed in Chapter 1, GaAs is a widely used and studied material for advanced opto-electronic applications. Its direct wide bandgap (1.42 eV) make it an ideal material candidate for LED, solar cell, and high-power applications. Additionally, the ability to alloy GaAs with other materials such as Al, In, and P creates a highly flexible and tunable system allowing for the careful selection of specific materials properties. By alloying GaAs with these other materials one can span a wide range of band gap energies. In particular, AlGaAs has been a key material for the fabrication of GaAs-based high electron mobility transistors, LEDs, and lasers due to its higher bandgap and the fact that it is virtually a lattice matched material – approximately 0.1% mismatch for pure AlAs – resulting in relatively stress-free devices. The nature of this strain-free interface has allowed for the relatively straightforward fabrication of GaAs/AlGaAs heterostructured nanowires with shell compositions as high as 90%wt. Al [29].

On the other hand, GaAsP has a much larger lattice mismatch with GaAs in general with a maximum mismatch of -3.7% for pure GaP. Therefore, while GaAsP is less widely used as a cladding layer for GaAs, it is commonly used as a strain compensation layer in the fabrication of InGaAs quantum well solar cells. InGaAs has a larger lattice parameter than GaAs resulting in a compressive stress inside the InGaAs film. By alternating layers of InGaAs and GaAsP, the overall stress state of the structure can be balanced resulting in fewer defects and an overall more efficient device [82]. In a nanowire geometry, the GaAs/GaAsP system presents a more

interesting case than the lattice matched GaAs/AlGaAs system due to the ability to engineer strain in the system as well as the inherently higher stability of GaAsP. Several studies have shown the ability of GaAsP to effectively passivate GaAs nanowires, thus increasing their photoluminescence intensity and even allowing for the creation of single nanowire lasers [27, 32].

As previously discussed, the inherently high surface to volume ratio of nanowires allows for the fabrication of heterostructures infeasible in a thin film, planar geometry. Due to the efficient elastic relaxation, thicker films of greater mismatch can be achieved. For example, while the critical thickness of GaP thin films grown on GaAs is only 2 nm [83], defect-free GaAs/GaP core-shell nanowires have been realized with shell thicknesses of 25 nm [10] – more than 10× the planar critical thickness. This ability to fabricate novel structures opens up possibilities of using strain to engineer the material's optical and electrical properties for specific applications. Strain engineering in core-shell nanowires has already been demonstrated as a means to modify band gap[84] and carrier mobilities [7]. However, the unique geometry of these nanostructures could significantly affect the fabrication and operation of strain-engineered devices. Because the heterointerface is no longer planar, it can no longer be assumed that the stress and strain fields will be homogenous along any given direction. One study of In incorporation in GaN/InGaN core-shell nanowires suggested that the observed increase of In concentration in the nanowire shell could be result of the highly efficient relaxation of strain in the shell [11]. Therefore, the ability to quantify strain fields of core-shell nanowires with both high spatial resolution and high strain sensitivities will be vital to the future development of strain engineered nanostructures. In the following sections, I will show how advanced TEM techniques couple with various modeling techniques to enable strain field characterization with both high spatial and strain resolution.

6.2. Nanowire heterostructure fabrication and structural characterization

In choosing a shell material it will be important to consider its scientific interest and importance, its potential for strain engineering, and its ease of fabrication and integration with our current MOCVD tools. For all of these reasons, GaAsP was chosen as the best candidate. Because GaP has a 3% lattice misfit with GaAs, higher levels of strain can be more easily engineered at the heterointerface compared to AlAs, which has a maximum misfit of only 0.1%. GaAsP also

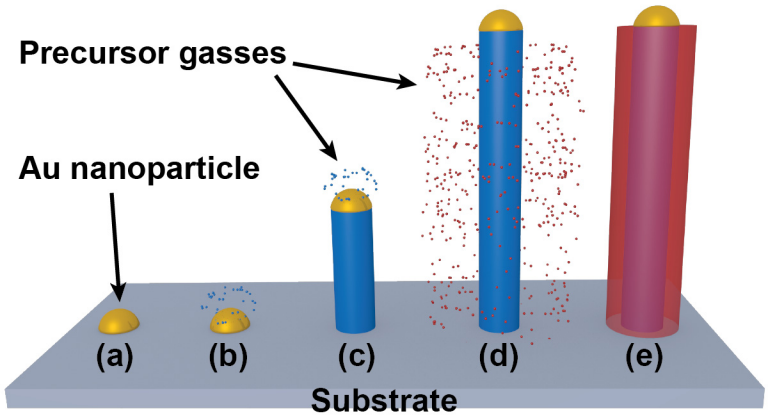

Figure 6-1. Schematic illustration of steps of core-shell nanowire growth consisting of (a) deposition of Au nanoparticles, (b) nanowire nucleation, (c) nanowire growth, (d) shell deposition, (e) resulting final structure.

presents a more robust fabrication process as P does not interact with low levels of O, which can lead to oxidation during and after shell deposition.

GaAs/GaAsP nanowires were grown using a two primary step growth process illustrated in Figure 6-1 and consisting first of a GaAs core nanowire growth followed by a shell deposition. Particle mediated core growth was carried out using the well-studied vapor-liquid-solid (VLS) mechanism. At the proper growth temperature, gaseous precursor materials will preferentially decompose and incorporate into the mediating particle (such as Au). Once the concentration of the precursor in the particle reaches saturation, layers of solid nanowire material will nucleate and grow at the nanoparticle-substrate interface. As this process continues, the mediating particle is pushed up by the growing nanowire. Once the desired core length is achieved, the growth conditions are changed so that a vapor-solid (VS) mechanism is favored over the VLS mechanism. As a result of this change in growth conditions, precursor materials will begin to deposit on the sidewalls of the nanowire forming a shell in a process identical to standard semiconductor thin film growth via MOCVD.

All nanowire growths were performed on GaAs substrates with a [111]B surface normal. Prior to growth, all substrates were cleaned using a standard triple rinse procedure consisting of three, 10 min sonicated rinses in acetone, methanol, and deionized (DI) water. Substrates were then blown dry using compressed air. Dried substrates were coated with a 1% poly-l-lysine aqueous solution for 10 min, rinsed, and dried. Finally, Au nanoparticles were drop-cast on the

substrates: small drops of dilute, aqueous solutions of Au nanoparticles were placed on the substrate and allowed to rest for 10 min. The substrates were then rinsed and blown dry.

Prepared substrates were loaded into a horizontal-flow MOCVD reactor. Exchange and loading of the prepared substrates was performed inside a glove box with continuously flowing dry nitrogen. Substrates were placed directly on a graphite susceptor that was used to directly heat the substrates using an infra-red heating lamp assembly. Unless otherwise noted, all growths consisted of four parts: a high temperature anneal, core growth, shell deposition, and cool down. Samples were fist annealed at a temperature of 600^{o}C for 10 min under flowing arsine to remove any native oxide on the substrate surface. This step also allows the Au seed particles to melt and alloy with the substrate surface causing the seed particles to form an epitaxial relationship with the substrate, ensuring vertical nanowire growth. It was found during the course of refining the growth process that the quality of a nanowire growth (evidenced by the percentage of vertical wires) is greatly dependent on the substrate cleaning and preparation and the cleanliness of the glove box environment during sample loading. After annealing, the reactor temperature was lowered to 420^{o}C for nanowire core growth. GaAs cores were grown using a TMGa flow of 16 μmol/min and an arsine flow of 150 μmol/min resulting in a V/III ratio of 9. Wires were grown for a total of 10 min achieving an average length of 12 μm. Core growth was then suspended by stopping the flow of TMGa, and the reactor temperature was increased to 725°C for shell deposition. TMGa was flown at a rate of 8 μmol/min while AsH_3 and PH_3 were flown at rates of 1267 μmol/min and 1234 μmol/min, respectively, resulting in a V/III ratio of 331. After a 5 min shell deposition, the samples were cooled to room temperature inside the reactor chamber. The flow of group V precursors was continued until below a temperature of 350^{o}C to prevent degradation of the nanowire sidewall surface.

After the growth, wires were characterized using a combination of electron microscopy techniques. Overall morphology and growth quality was assessed using SEM while TEM was used for a more detailed analysis of wire quality, including crystalline quality and chemical composition. The most promising samples for strain analysis were then prepared for cross-sectional analysis. Entire fields of wires on the substrate were first flattened and aligned using a mechanical rolling method similar to other approaches described in literature [85]. Using a scanning electron microscope equipped with a FIB, groups of nanowires were then milled into ~100 nm thick cross-sections suitable for TEM analysis. Prior to FIB milling, nanowires were

coated with protective layers of amorphous carbon and platinum to ensure the milling process did not result in amorphization of the nanowire shell or core [78]. While this method of nanowire cross-sectional preparation has a relatively low yield, it was determined to be the best technique to ensure repeatability of TEM and CBED measurements on individual nanowire cross-sections.

Figure 6-2 shows SEM images of the resulting core-shell nanowires. These images not only show the overall high quality of the growth – evidenced by the high percentage of vertical growth – but also indicate a high level of strain in the nanowires. In both the tilted and top-down views [Figure 6-2(a) and (b), respectively], many of the nanowires are observed to be bent in a similar manner, which can be attributed to asymmetric strain fields in the core-shell structure [86]. Cross-sectional TEM of the nanowires shows that the asymmetry is most likely the result of non-uniform shell growth. Figure 6-3(a) shows an annular dark-field (ADF) STEM image of a typical GaAs/GaAsP nanowire cross-section. Besides clearly showing the core-shell nature of the structure, this image also demonstrates the non-uniform shell growth – evidenced by the thicker shell along the lower left facet of the nanowire cross section in Figure 6-3(a) – that was observed across many other nanowires.

It is also interesting to note the areas of bright contrast seen at each corner of the shell in Figure 6-3(a). As discussed in Chapter 2, the contrast in ADF-STEM is sensitive to changes in chemical composition, such that elements of higher atomic number Z yield brighter contrast. This sensitivity is due to enhanced Rutherford scattering of electrons to high angles by heavy elements, which is proportional to Z^2. However, EDS maps [Figure 6-3(b – d)] show that the brighter corners actually have a higher concentration of P relative to the average shell

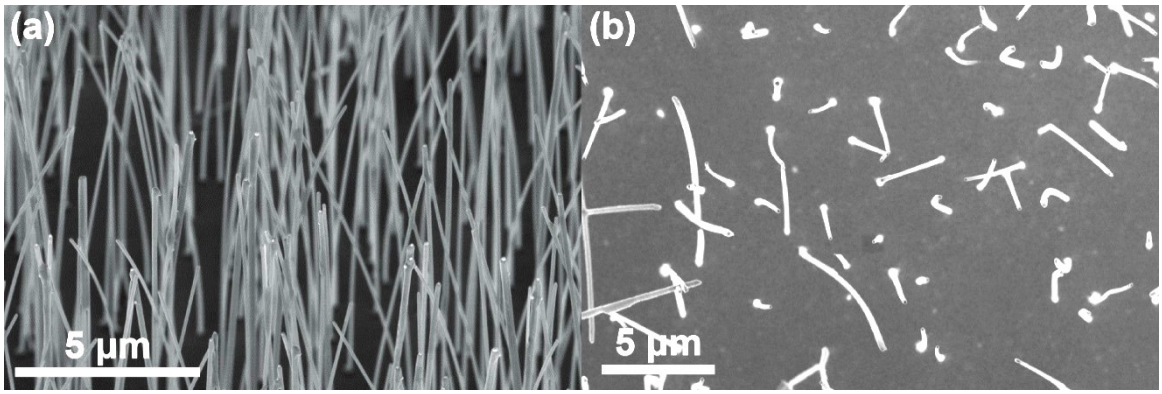

Figure 6-2. SEM images of GaAs/GaAsP core-shell nanowires. (a) was obtained at a 45° to the surface normal while (b) shows a top down view of the sample.

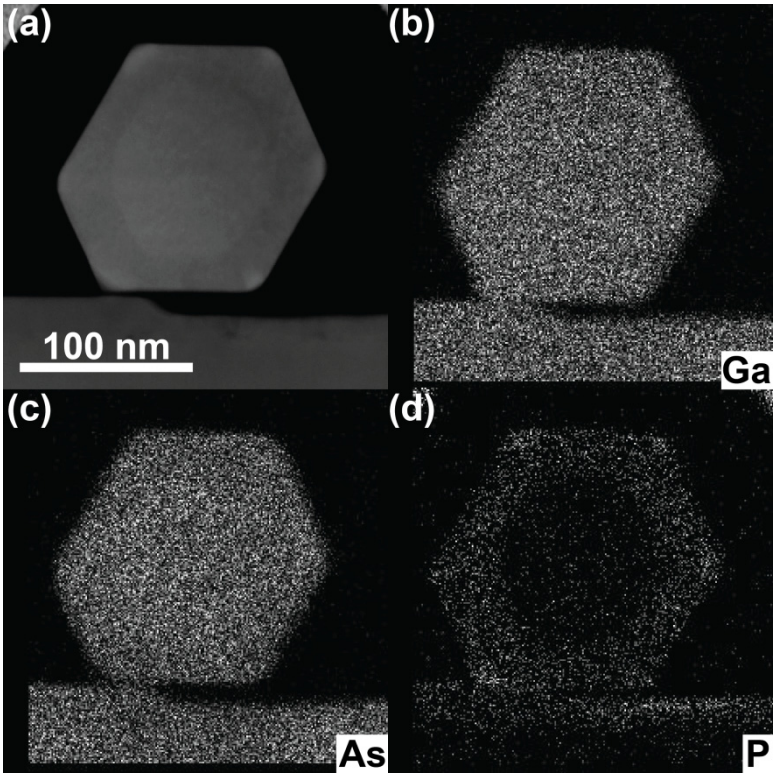

Figure 6-3. (a) ADF-STEM image of a typical GaAs/GaAsP core-shell nanowire cross-section. (b – c) EDS maps of Ga, As, and P signals.

concentration (the average concentration of P in the shell is estimated at 10%at, while the concentration at the corners is almost 30%at), which would yield darker contrast in ADF-STEM images based purely on the chemical composition (Z_{As} = 33 and Z_P = 15). Therefore, the bright STEM contrast observed in the corners must be the result of local lattice deformation due to stress relaxation. The higher P concentration at the corners is most likely the result of in-diffusion after shell growth during cooling in a PH_3 environment. Additionally, corners will be the most efficient sites for strain relaxation which could make them preferred sites for P incorporation. Similar behavior has been observed in the fabrication of GaN/InGaN core-shell nanowires [11].

6.3. Evaluating strain characterization techniques

In considering which strain characterization technique will be most useful – GPA, NBED, or CBED – one characteristic of core-shell nanowires makes CBED the obvious choice. In Chapter 5, NBED and GPA were both used to quantify and map the strain in nanostructured InAlN/GaN HEMT devices. To properly use these techniques, however, a strain-free reference area of the

sample must be located relatively close to the strained interface. In a core-shell nanowire, it can be reasoned – and later shown by FEA – that there is no strain-free area within the wire due to the heterointerface being wrapped around itself. CBED, on the other hand, provides a direct measurement of the local strain fields with no need of a reference area, thus making it the technique of choice for strain analysis in this particular scenario. However, prior to performing a full CBED study, it will be important to assess the suitability of each system to this type of analysis. As with the GaN based systems discussed in Chapter 4, this means that suitable zone axes will need to be determined near each of the growth axes – [111] for GaAs/GaAsP. Not only will these zone axes need to be properly indexed, but dynamic simulations must be performed to determine the extent of HOLZ line interaction in order to determine the usability of each axis for study.

As described in Chapter 4, CBED studies for the determination of lattice parameter and strain, in general, require the use of a low symmetry zone axis with minimized HOLZ line interaction. However, care must also be taken to choose a zone axis that also minimizes any projection effects as a consequence of tilting away from the nanowire growth axis. As previously described, the GaAs nanowire cores used in this study exhibit a zinc-blende structure and predominantly grow along the [111] zone axis. Therefore, suitable zone axes are best found by tilting toward other axis of high symmetry. This method of finding a suitable axis takes advantage of prominent Kikuchi lines that can act as a map in reciprocal space and ensure the repeatability of finding the same zone axis across multiple wires and experimental sessions.

Two axes [Figure 6-4] were found experimentally and indexed using the JEMS software[59] suite described in Chapter 3. The first zone axis shown in Figure 6-4(a) was identified as [556] and it lies approximately 5^{o} off the [111] zone axis towards the [001] zone axis. In this pattern it can be seen that there is a large number of sharp, well-defined HOLZ lines with little dynamic interaction. While this speaks well for the possibilities of using this zone axis for strain field characterization, all of the HOLZ lines seen in the pattern have relatively equal contribution from each primary direction because the [556] zone axis lies near [111]. One of the key attributes of the CBED patterns used to characterize strain fields in the InAlN system discussed in Chapter 4 was the fact that some HOLZ lines were highly indexed in the c-direction (i.e. [117]) while others were not (i.e. [450]). This allowed for the observation of large strain

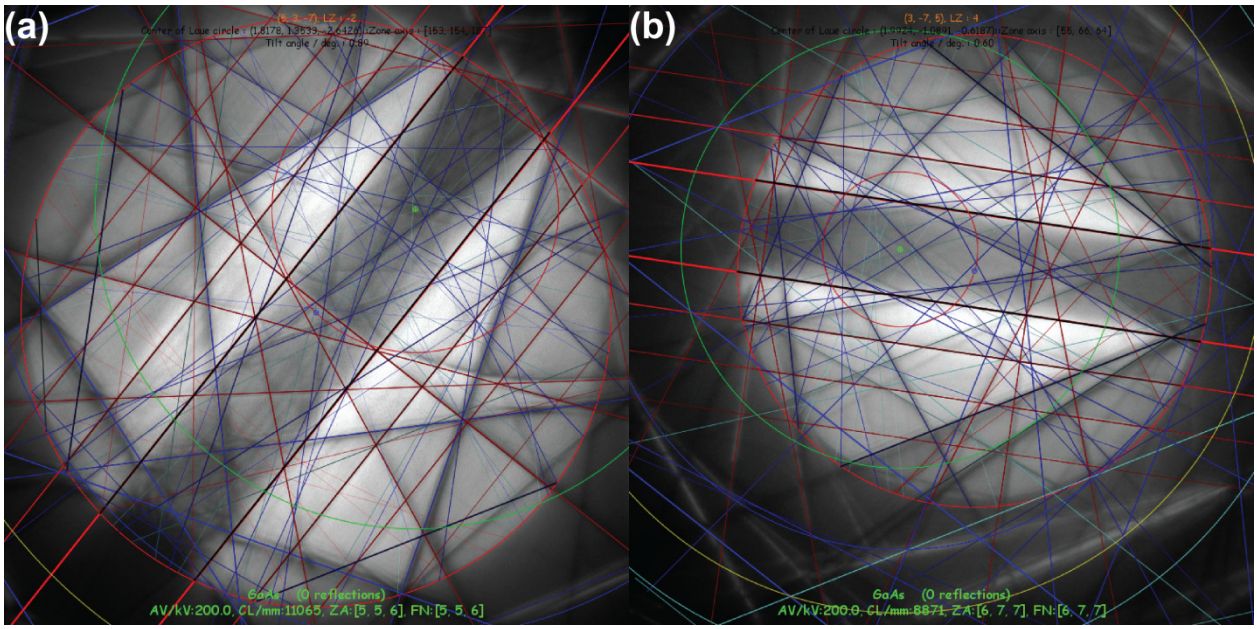

Figure 6-4. Representative images of the (a) [556] and (b) [677] zone axes identified in GaAs near the [111] zone axis and shown to be suitable zone axes for CBED study.

field variations along the [001] growth direction which correlated well with FEA simulations of the system. In the InAlN system, these dichotomized HOLZ lines were the result of using the [540] zone axis that is orthogonal to the growth direction. In the GaAs nanowires, however, it is not possible to use such a zone axis making the separation of strain components more challenging. While a second zone axis was identified for possible use – the [677] which lies approximately 4^{o} off the [111] towards the [001] zone axis – it does not provide any specific advantage over the [556] and therefore was not considered throughout the remainder of this investigation.

6.4. Characterizing strain in GaAs/GaAsP core-shell nanowires

As described in Chapter 2, CBED is a powerful technique for the characterization of strain in crystalline materials providing both high spatial and strain resolution. This is possible due to the fact that CBED patterns are formed from a converged electron beam. The converged nature of the beam not only creates a small spot size allowing for probe sizes on the order of 1 nm, but also allows for diffraction from planes not orthogonal to the beam direction and from high-order planes, which are extremely sensitive to small changes in lattice parameters.

After cross-sectional TEM sample preparation by FIB, GaAs/GaAsP nanowires were imaged in a JEOL 2010F equipped with an annular dark field detector for image acquisition and

a CCD camera for CBED pattern acquisition. Patterns were formed using an accelerating voltage of 200 keV, a condenser aperture size of 100 μm, and a convergence angle of approximately 30 mrad. Ideal nanowire cross-sections chosen for study exhibited a high degree of symmetry (i.e. uniform shell thickness) as seen in Figure 6-5(a). Figure 6-5(b) shows a typical example of a CBED pattern obtained along the [556] zone axis in GaAs/GaAsP, as previously described. As this image shows, this zone axis provides a number of prominent HOLZ line with minimal interaction. Two pairs of lines that proved to be the most useful in our analysis were the $\{\bar{6}\,42\}$ and $\{5\bar{1}\,\bar{3}\}$ lines. These lines were observed to maintain a good level of contrast across the entire nanowire allowing for the best analysis of HOLZ line broadening and shifting. CBED patterns were obtained in STEM mode, which allowed for the simultaneous acquisition of STEM images and CBED patterns. CBED patterns were then obtained by focusing the electron probe at a certain position on the nanowire cross-section as shown schematically in Figure 6-5(a). Series of patterns were acquired along lines radiating from the center of the nanowire towards the corner and facet surfaces, resulting in over 150 patterns obtained from an individual structure. Each series was then analyzed to compare and identify trends in HOLZ line splitting and

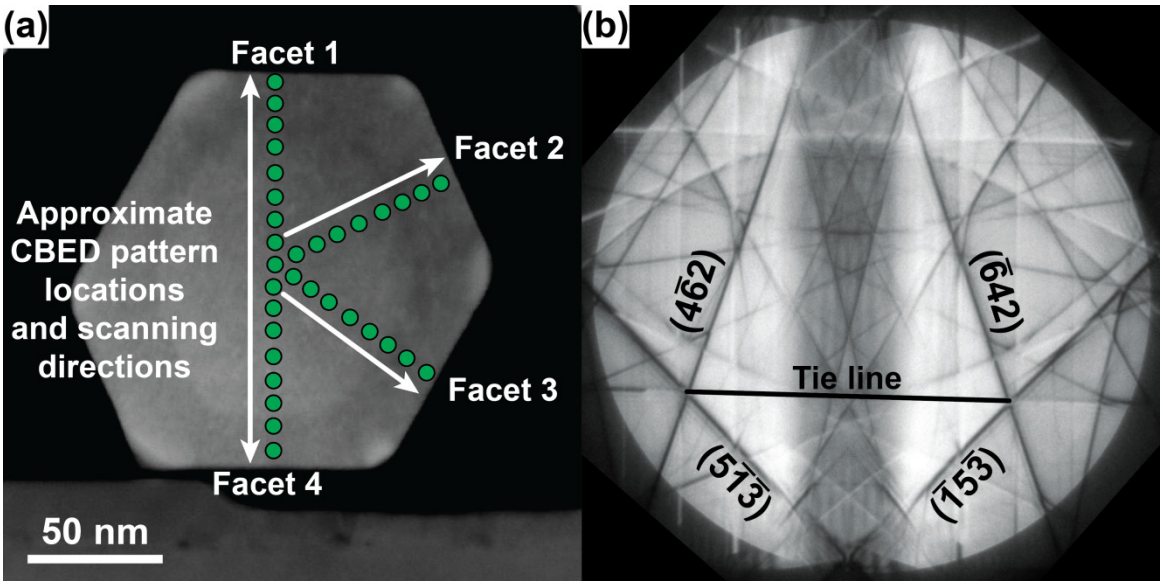

Figure 6-5. (a) ADF-STEM image of GaAs/GaAsP nanowire cross section showing approximate locations where CBED patterns were obtained. (b) Typical CBED pattern obtained along the [556] zone axis in GaAs/GaAsP core-shell nanowire with two pairs of prominent lines labeled – the $\{\bar{6}\,42\}$ and $\{5\bar{1}\,\bar{3}\}$ lines.

shifting. For the sake of this discussion, facets were numbered as indicated in Figure 6-5(a) with Facet 1 at the top and counting clockwise.

6.4.1. HOLZ line splitting

As demonstrated in Chapter 4, the analysis of HOLZ line splitting can be a powerful tool to directly probe the out of plane deformation that a sample experiences due to strain relaxation at a free surface. In our analysis of the InAlN/GaN HEMT structures, this was done by assuming that the surface of the sample is fully relaxed. This assumption allowed the HOLZ line broadening to be approximated using two kinematic CBED simulations. Finally, by measuring the separation of the two kinematic simulations, the relaxation of the sample could be directly measured and compared to FEA simulations. This same approach was used during our initial investigation of the GaAs/GaAsP heterostructures. Figure 6-6(a) shows the regions of the sample where two CBED line scans were acquired – one line extending from the center to the facet surface and another extending to the corner surface. Each line scan consisted of up to 25 individual CBED patterns. Figure 6-6(b) shows the evolution of the ($\bar{6}$ 42) HOLZ line along each acquisition line. It can be seen from this series of images that there is differing behavior along each line. Going towards the facet surface, the ($\bar{6}$ 42) line shows very little broadening. Even at the surface, where the most relaxation is expected, the ($\bar{6}$ 42) line maintains a seemingly constant width. Going towards the corner surface, however, the evolution of the ($\bar{6}$ 42) line is very different. Near the

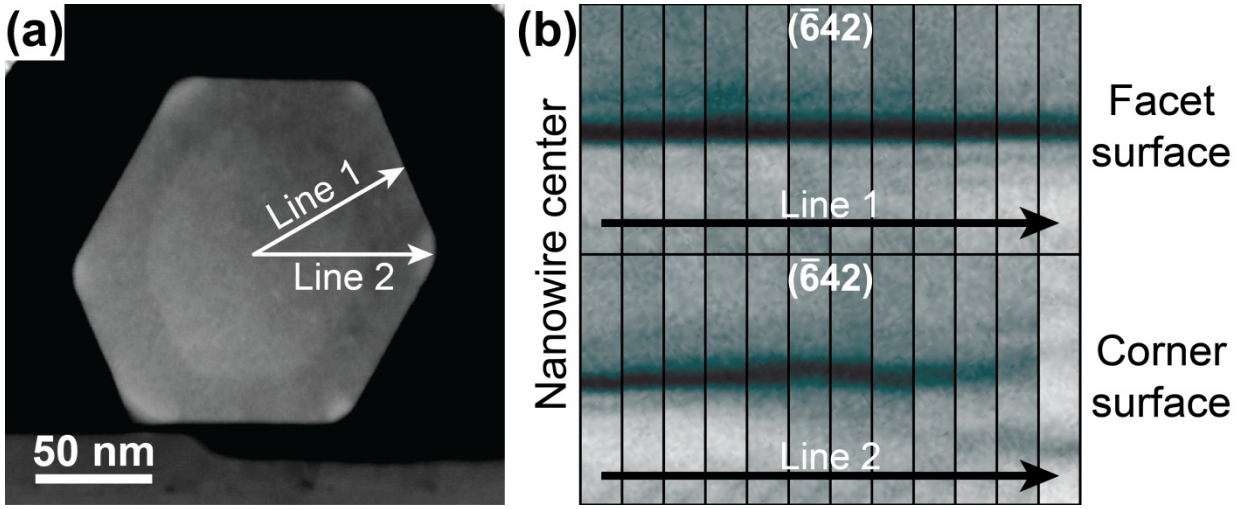

Figure 6-6. (a) DF-STEM image of GaAs/GaAsP core-shell nanowire with arrows indicating the locations where CBED patterns were obtained. (b) The evolution of the ($\bar{6}$ 42) HOLZ line is shown with images on the left being obtained from the center of the nanowire cross-section and those on the right at the corner and facet surface.

center the same width and contrast is observed; closer to the corner surface, the line loses some contrast and broadens slightly with a second fringe appearing below the primary line. Right at the surface, there is a rapid splitting of the line, as seen in the last two panes of Figure 6-6(b) indicating a high level of deformation very near the surface. This observation also agrees with the bright contrast observed at the corner surfaces in ADF-STEM images, as previously discussed in Section 6.2.

Additionally, CBED patterns near the corner surface exhibit a non-symmetrical type of splitting – that is, symmetric pairs of lines such as the ($\overline{6}$ 42) and (4$\overline{6}$ 2) do not split in the same

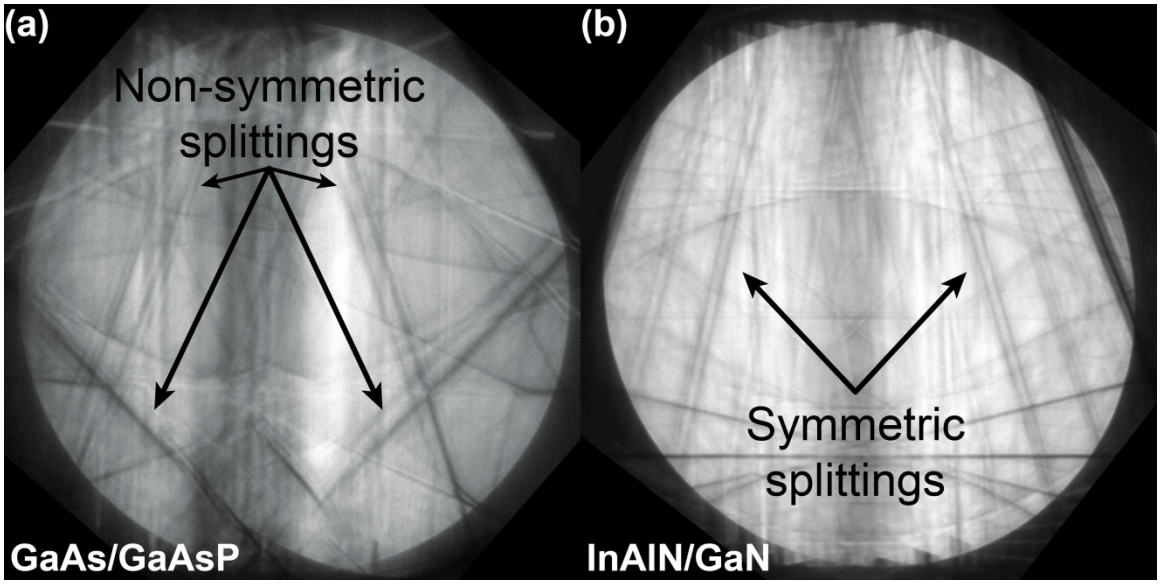

Figure 6-7. Comparison of CBED patterns obtained from (a) a GaAs/GaAsP core-shell nanowire and (b) a InAlN/GaN HEMT structure showing examples of non-symmetric and symmetric HOLZ line splitting respectively.

way. Figure 6-7 shows two examples of CBED patterns that exhibit non-symmetric [Figure 6-7(a)] and symmetric [Figure 6-7(b)] HOLZ line splitting. The non-symmetry seen in the GaAs/GaAsP heterostructures could be caused by a non-symmetric strain field through the thickness of the sample resulting from the non-homogenous nature of the strain fields and projection effects. In the case of the InAlN/GaN HEMT structure, small tilts away from the primary zone axis have a smaller effect due to the homogenous nature of the strain fields created by the planar interface leading to more symmetric splitting of the HOLZ lines. In the surface total relaxation assumption used in Chapter 4, it was also assumed that deformation at the free surface was occurring in an orthogonal direction to the growth direction allowing the splitting to

be characterized by a single variable, θ. This assumption is shown to be valid for the InAlN/GaN structures by the fact that the (450) line does not split. In the GaAs/GaAsP system, however, the non-symmetric splitting points to the fact that this kind of assumption does not hold up. The deformation in this case is more complex geometrically and cannot be characterized by a single variable, making it difficult to extract meaningful information from the HOLZ line splitting.

Besides the non-symmetric line splitting, the increased composition of P at the nanowire corners is observed to have a significant impact on the presence of HOLZ line splitting. Due to the inhomogeneous nature of the P incorporation, the splitting behavior of HOLZ lines from separate corners of a single nanowire cross-section is seen to vary greatly. It is therefore more useful to concentrate the analysis on the nanowire facets that are, in general, more uniform. While little splitting was observed along the facets, Figure 6-6(b) does suggest the presence of HOLZ line shifting that would result from more uniform changing strain fields; therefore, by tracking the position of the HOLZ lines, we can garner information about the nature of this change.

6.4.2. HOLZ line shifting

HOLZ line shifting is best measured by considering the movement of lines of interest relative to other lines. Therefore, a tie line is created between the intersection points of the ($4\bar{6}\ 2$) and ($5\bar{1}\ \bar{3}$) lines and the ($\bar{6}\ 42$) and ($\bar{1}\ 5\bar{3}$) lines, as shown in Figure 6-5(b). By measuring the length of this tie across a series of CBED patterns, the relative shift of the HOLZ lines can be determined. Series of CBED patterns were obtained along lines radiating from the center towards the surface of four facets – labeled Facet 1 through Facet 4 in Figure 6-5(a). The tie line length was then calculated and measured using the HANSIS software[87]. The tie line length of each CBED pattern was then plotted as a function of the distance from the facet surface where each pattern was obtained. Figure 6-8 shows the plots of tie line length versus distance for line scans taken along the four facets. Looking at these plots, key similarities and differences are observed. Firstly, each plot seems to have two distinct regions which correspond to the core and the shell due to the fact that the transition between these regions occurs around 22 nm – the thickness of the GaAsP shell. The only exception is Facet 4 [Figure 6-8(d)], which shows a transition around 18 nm. This difference could be due to projection effects when tilted to the [556] zone axis or drift of the sample during CBED acquisition.

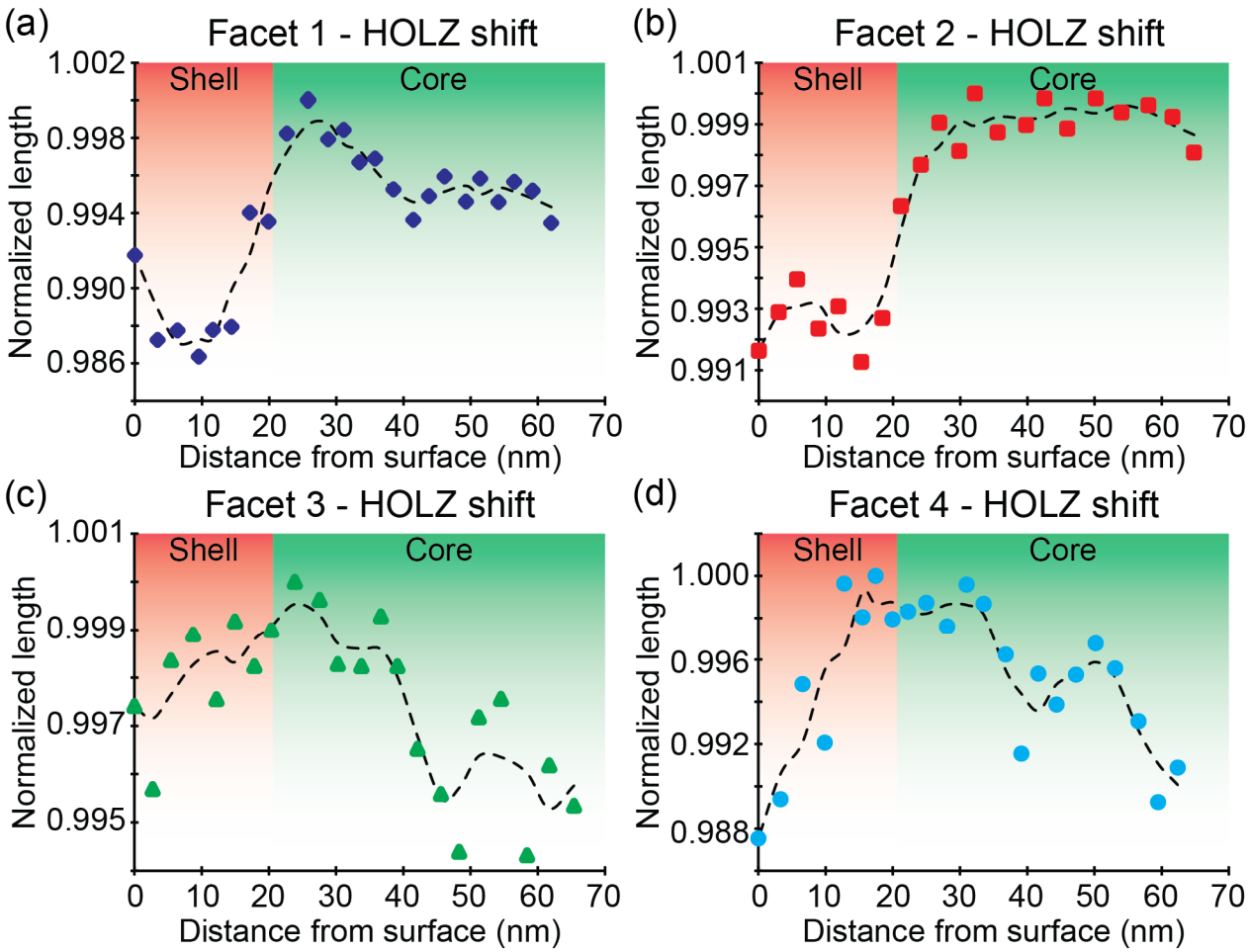

Figure 6-8. Plots of the {4$\bar{6}$ 2}/{5$\bar{1}$ $\bar{3}$ } tie line length versus distance from the facet surface for Facets 1 – 4. Dotted lines are a guide to the eye only and shading shows approximate transition between core and shell.

More important are the differences observed among the plots for different facets. While each plot has a core and shell region, the behavior within each of these regions varies from scan to scan. While Facet 2 shows relatively little change across the core region, Facets 3 and 4 show a gradual increase towards the interface throughout. Facet 1, on the other hand, begins flat and increases closer to the core-shell interface. Likewise, the shell behavior is observed to vary as well with some increasing and others decreasing. While it is difficult to directly extract the magnitude or direction of a strain field from these plots, they do point to the non-symmetric nature of the strain fields around the nanowire. Because no two plots are the same, it is likely that each facet will exhibit unique HOLZ line shifting behavior. This conclusion, at first, seems counterintuitive given the symmetries of the geometry and the zinc-blende crystal structure; however, the nature of the strain fields and the lack of symmetry will become clearer as we

develop the FEA model. Measurements of the HOLZ line shifting from Facets 5 and 6 were attempted; however, due to the thicker shell at Facet 5 and the degradation of the C protective layer around the nanowire the data collected was unreliable. The importance of considering the amorphous C coating will become more evident in our discussion of the FEA results.

These experimental results demonstrate the ability of CBED to probe the local strain state of core-shell nanowire heterostructures as seen in the unique HOLZ line shift profiles along each facet. These unique profiles suggest a lack of radial symmetry that might be hypothesized given the geometry and crystalline symmetries. Despite these insights, a quantitative analysis of the strain fields will require us to formulate a proper FEA model and determine the best method of comparing it to our experimental results. The following sections will discuss not only the development of an FEA model, but also how Bloch wave simulations can be used to correlate the model and experimental results.

6.5. Finite element analysis and Bloch wave simulations

In our discussion of strain in the InAlN/GaN HEMT structure in Chapters 4 and 5, it was shown how HOLZ line splitting could be directly correlated to an FEA model of the system using the free-surface total relaxation assumption. Additionally, experimental strain profiles obtained using NBED and GPA could also be directly compared to strains generated from the FEA calculation. Unfortunately, due to the non-symmetric nature of the HOLZ line splitting observed and the unsuitability of NBED and GPA to characterize strain in this core-shell system, neither of these methods will be able to correlate the experimental HOLZ line shifting data to the FEA model. However, the fact that almost no HOLZ line splitting is observed along the facet directions does enable us to assume that there is little variation in the strain field through the thickness of the sample at any given point – that is, the strain field does not vary along the growth direction. This assumption will allow us to simulate CBED patterns using a Bloch wave method which can then be correlated to the experimental results.

6.5.1. The FEA model

The standard geometry used for the FEA models was based on the nanowire cross-section seen in Figure 6-5(a), though the thicker shell along Facet 5 was not taken into account in order to generalize the model and simplify the process of creating multiple versions of the standard

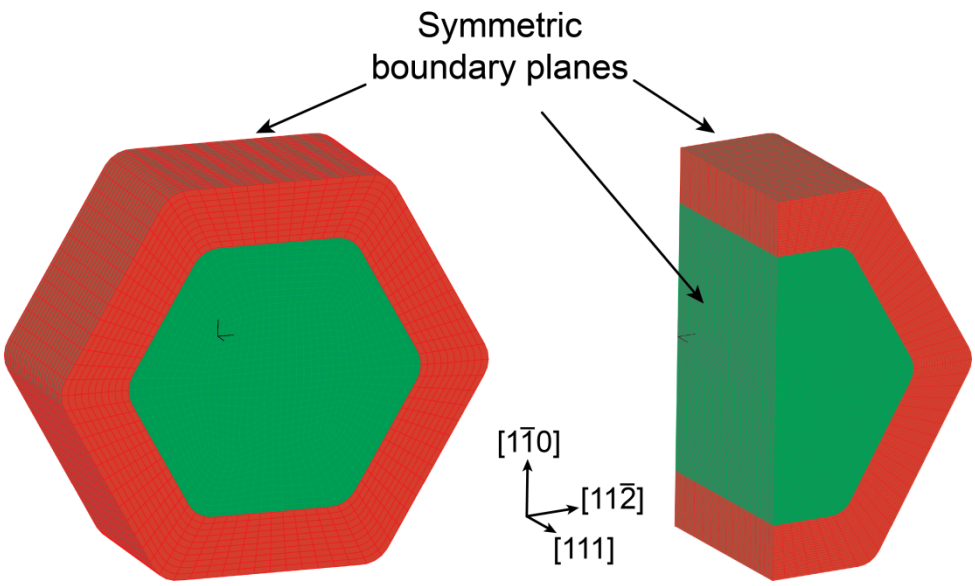

Figure 6-9. Examples of the geometries used in the FEA analysis of GaAs/GaAsP core-shell nanowires showing both whole and half sections.

geometry. In general, the model [Figure 6-9] consists of a GaAs core with a radius of 54 nm and a 22 nm thick GaAsP shell. Corners of the hexagonal core and shell were filleted with a 10 nm radius. The thickness of each model was 75 nm though a symmetric boundary (no normal displacement) on the back plane of the model creates a virtual thickness of 150 nm – the thickness of the wire cross section as measured by CBED. Using this type of boundary condition on the back surface assumes that the stress and strain fields are symmetric about the mid-plane of the nanowire cross section. This is a reasonable assumption as non-symmetric forces would lead to an unstable structure. Similarly, some models consisted of only half a cross-section with a symmetric boundary plane along the [1$\bar{1}$ 0] axis as illustrated in Figure 6-9. In fact, in designing the FEA model it was observed that a full hexagonal model with only one symmetric boundary plane was inherently unstable causing the calculation to fail at finer mesh densities. Therefore, to achieve the desired mesh, half-hexagonal models proved necessary as the second boundary plane provided additional stability. This stability issue could also be solved by surrounding the full-hexagonal model with a confining medium as will be discussed in detail shortly.

Figure 6-9 also shows that facet normal directions are designated as ⟨110⟩ type – as observed experimentally – while corner directions were ⟨112⟩ type and the growth direction [111]. To preserve the symmetry of the mechanical properties in GaAs, orthotropic axes were defined. Therefore, in the following discussion the axes designated as 1, 2, and 3 correspond to

the crystallographic directions of [100], [010], and [001] respectively. In like manner, the GaAs and GaAsP materials were defined as orthotropic materials with cubic symmetry and elastic constants *E*, *G*, and *v* shown in Table 6-1. Besides their elastic constants, materials were given a pseudo-thermal expansion coefficient. As in our analysis of the InAlN/GaN system, this coefficient is used to create the lattice misfit between the materials. In all cases, GaAs is used as the basis and therefore has a coefficient of 0. The elastic constants for $GaAs_{0.9}P_{0.1}$ were calculated using Vegard's rule and the elastic constants for GaAs [55] and GaP [88]. In addition to the two materials of the core-shell heterostructures, some models also employed a surrounding amorphous carbon material to take into account the electron-beam deposited carbon layer around the nanowire. Due to its amorphous nature, this material was described as an isotropic material with elastic constants *E* [89] and *v* and no expansion coefficient.

Material	E (GPa)	G (GPa)	v	Lattice mismatch
GaAs	85.92	59.6	.310	0.00
$GaAs_{0.9}P_{0.1}$	179.86	123.94	.308	-0.0036
Amorphous C	67	NA	.300	0.00

Table 6-1. Elastic constants and pseudo-coefficients of thermal expansion for materials used in FEA models.

All models were meshed using 27-node brick elements. A high mesh density was used in order to best approximate the spatial resolution of the experimental CBED results and is typified by the two examples in Figure 6-9. Mesh density was highest around regions of high deformation – namely the shell – while regions like the protective carbon layer used a relatively coarse mesh. Typical calculation times for these high density meshes were on the order of 3 – 5 h depending on whether a half or full-hexagonal model was being employed. FEA modeling and calculation was performed using the ADINA software package.

6.5.2. Bloch wave simulations

After the FEA calculation, strain values were extracted from the FEA model along lines running through the thickness of the model emulating the path an electron beam traveling through the sample. The strain values were then averaged to provide information about the local strain state

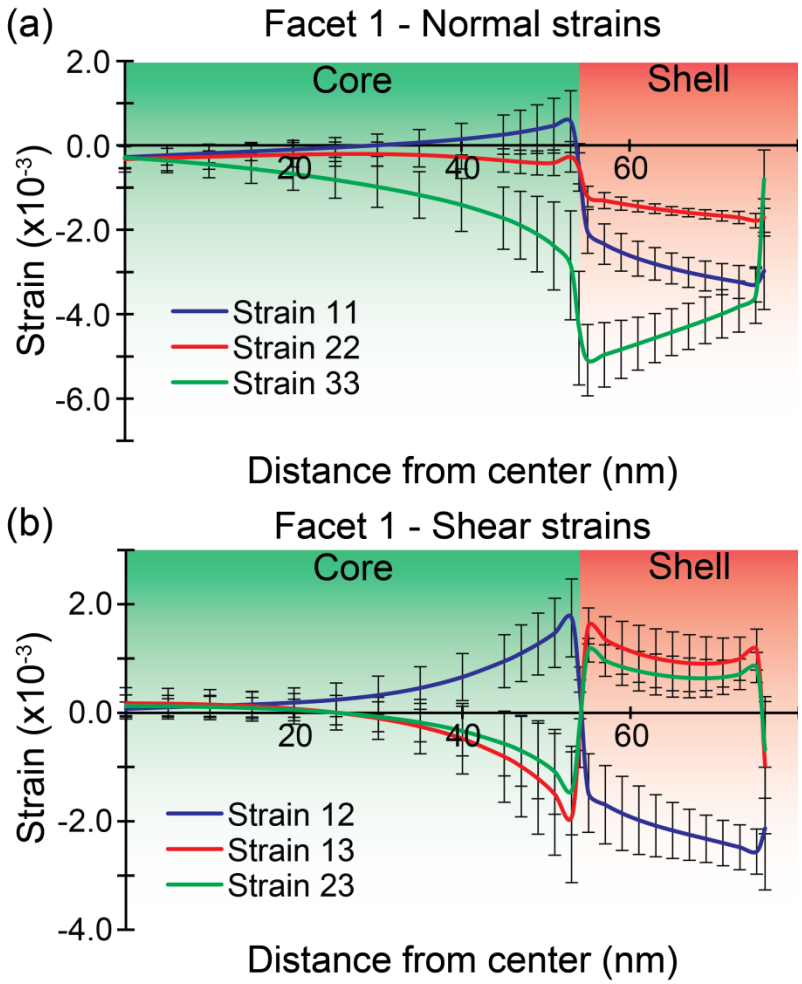

Figure 6-10. Examples of strain data extracted from FEA model. Plots showing the average (a) normal strains and (b) shear strains for through-thickness lines at specified distances from the nanowire center.

at that point of the model. Columns of the line-average strains were collected creating virtual line scans radiating from the center towards the various facets in a fashion analogous to the collection of CBED linescans demonstrated in Figure 6-5. Figure 6-10 shows two examples of the resulting data plots. Each point on these lines represents the average strain along a line – oriented along the [111] direction – running from the front surface of the model to the back plane of the model and lying a certain distance away from the nanowire center towards the facet surface. The error bars at each point represent the standard deviation of the strain along line-average and give an indication of the strain variation at that location. Like the experimental data, each of these plots is seen to exhibit core and shell regions with differing behavior among each strain component. Even the change in variation follows different trends for each strain component, creating a complex picture of the strain state. While these plots give some indication of how the strain

fields behave, they are in general not very intuitive, neither can they be easily compared to our experimental data. Therefore, an additional analysis step will be required.

This additional step is the simulation of CBED patterns based on the strain values extracted from the FEA calculation. Since CBED patterns are directly affected by changes in the crystalline lattice, a comparison of experimental CBED patterns and CBED patterns simulated based on an input lattice under a specified strain state could help to identify the actual strain field that resulted in the experimental pattern. Using the average of the strains, a local "average" unit cell is created and used as the basis for a Bloch wave simulation of a CBED pattern. Normal strains are used to calculate the lattice parameters *a, b,* and *c* using the following equation:

$$a = a_0 + \varepsilon a_0 \qquad (6\text{-}1)$$

where a is the lattice parameter of the "average" unit cell, a_0 is the reference lattice parameter of GaAs, and ε is the appropriate average strain value. Similarly, the unit cell angles α, β, γ and were found to play a major role in determining the behavior of HOLZ line shifting within the core and shell regions and were determined by the following equation using a small angle approximation:

$$\alpha = \frac{\pi}{2} - \gamma' \qquad (6\text{-}2)$$

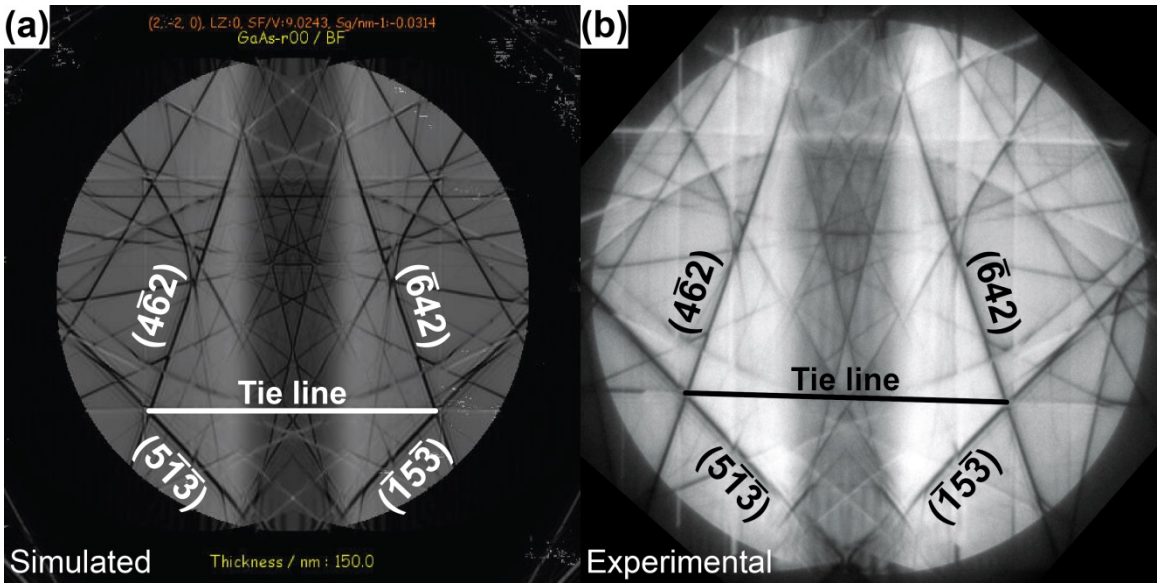

Figure 6-11. Comparison of a typical (a) simulated and (b) experimental CBED pattern with significant lines labeled.

where γ' is the appropriate average shear strain value. The resulting average unit cell was then used as the input for a Bloch wave simulation of a CBED pattern. This process was repeated for each average-line in the line scan towards a particular facet. Each Bloch wave simulation assumed a sample thickness of 150 nm – as experimentally determined – and included 30 strong reflections in the calculation while weak reflections were accounted for using a generalized Bethe approximation previously described in Chapter 3. All Bloch wave simulations were performed using the JEMS software package. Figure 6-11(a) shows an example of a typical simulated CBED pattern compared to an experimental pattern shown in (b) and demonstrates the ability of the Bloch wave method to accurately reproduce most of the important features observed in the experimental pattern. The resulting CBED patterns were then analyzed in the same manner as their experimental counterparts in which the length of the $\{\bar{6}\,42\}/\{1\bar{5}\,3\}$ tie line is measured and plotted as a function of distance away from the facet surface.

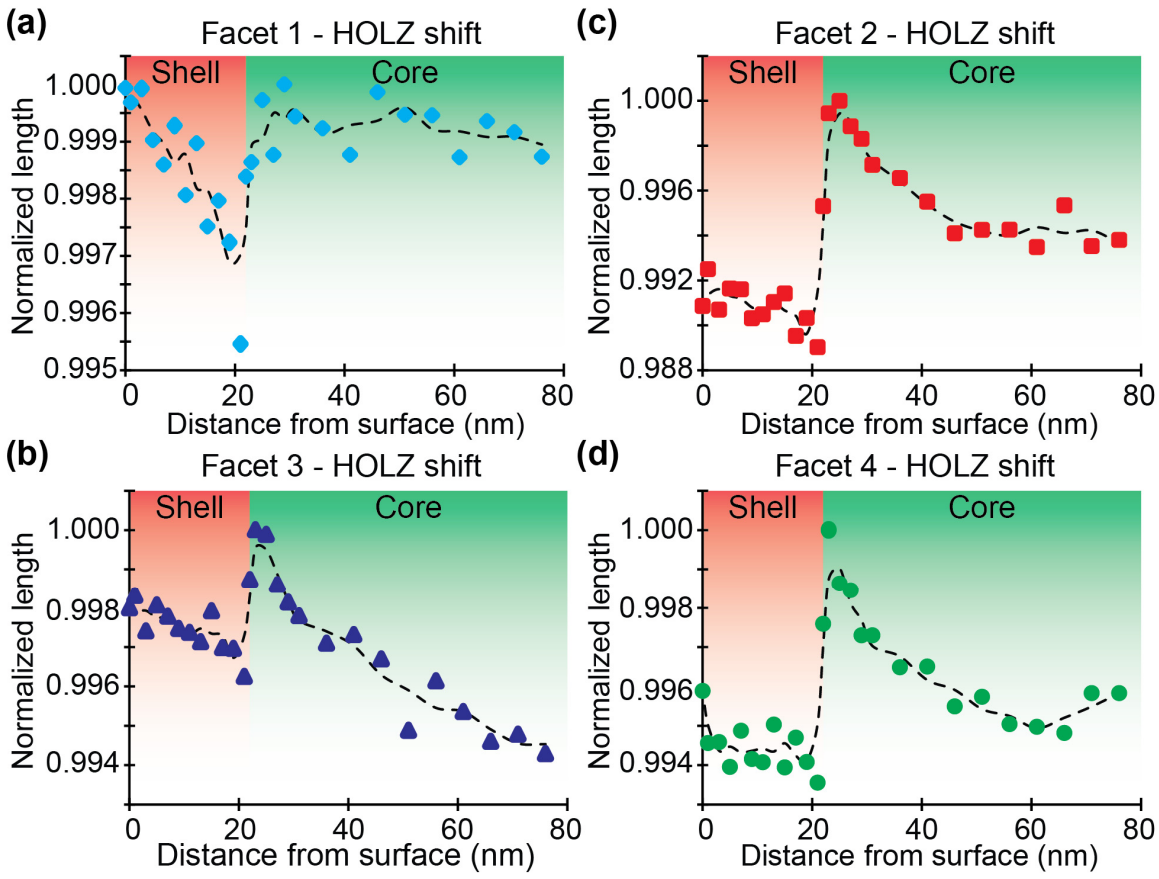

Figure 6-12. HOLZ line shift profiles from series of simulated CBED patterns based on initial FEA investigation of half-hexagonal, core-shell heterostructures. Dotted lines are guides to the eye only.

6.5.3. The initial model

The initial case investigated consisted solely of a core-shell, half-hexagonal model with no surrounding carbon. Figure 6-12 shows plots of measured HOLZ line shifting obtained from series of simulated CBED patterns based on the strain information calculated from this initial FEA model. Comparing these plots to the experimental data [Figure 6-8], we see that the simulated series of plots exhibits the same core and shell regions and that the variation within the core region seems to follow fairly well with what is observed experimentally. Additionally, it is seen that no two facets behave the same suggesting the unique nature of the strain fields along each facet. Unlike the core regions, the behavior of the shell regions seems to deviate more strongly with both the magnitude of change and the overall trends being different. This discrepancy suggests that there is most likely some other factor acting on the shell to change its behavior leading to the natural conclusion that the amorphous carbon coating could play a significant role in dictating the wire's relaxation.

6.5.4. Effects of surrounding media

Based on the initial results, the second iteration of the model included a surrounding layer of amorphous carbon modeled as a semi-infinite isotropic material. While the carbon coating is experimentally only 50 – 100 nm thick, FEA calculations indicated that strain fields did not propagate significantly beyond this boundary making this assumption more reliable. Figure 6-13 shows band plots of the normal and shear strain components at the front surface of a GaAs/GaAsP core-shell heterostructures surrounded by a carbon coating. These plots directly

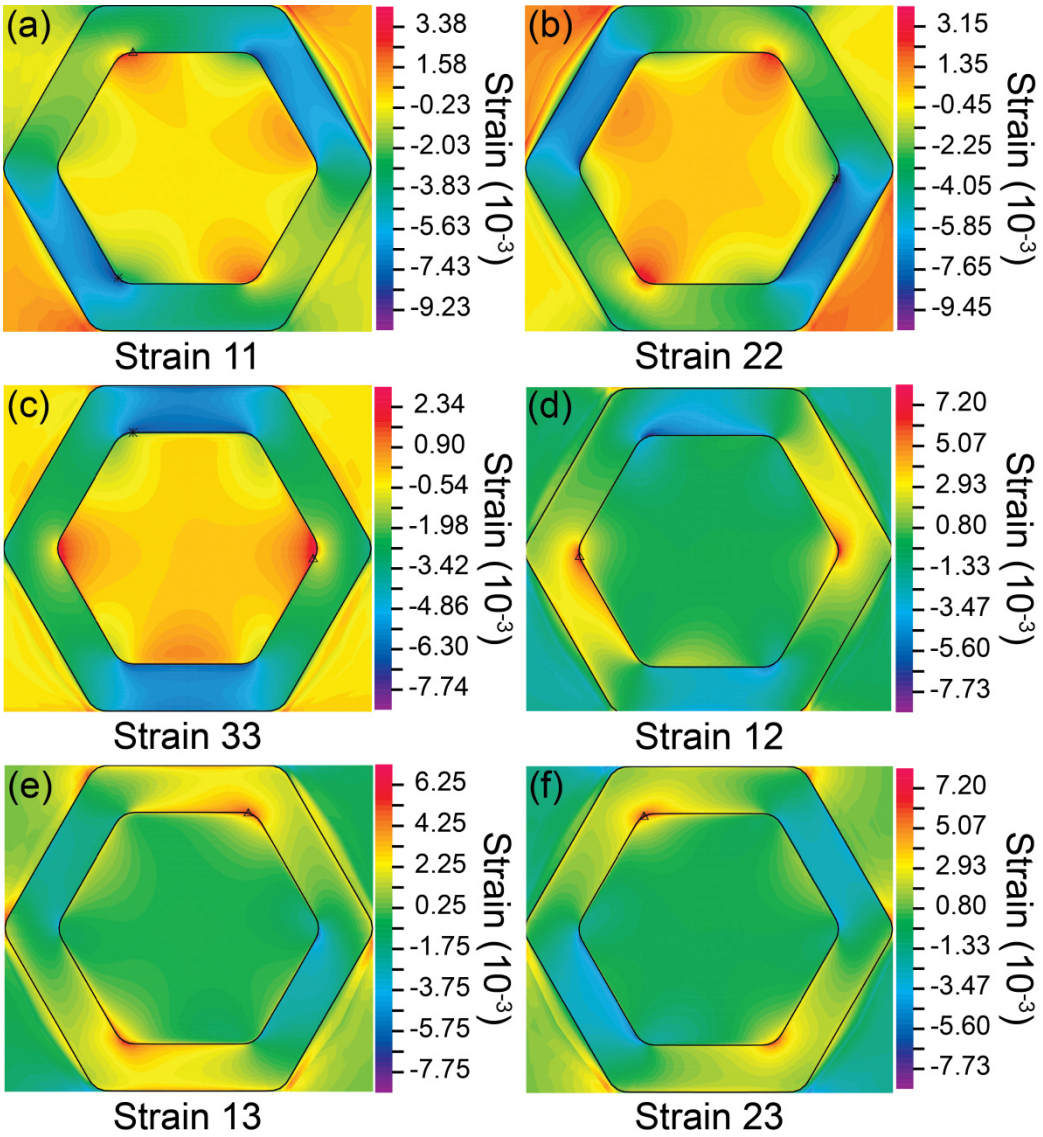

Figure 6-13. Band plots of the (a) – (c) normal and (d) – (e) shear strain components calculated for a core-shell nanowire heterostructures surrounded by a carbon coating

show the low symmetry of the strain fields suggested by the experimental HOLZ line shifting with any given component having at most a two-fold rotational symmetry. Therefore, the combination of strain fields along any facet will be unique leading to unique HOLZ line shifting behavior. While this lack of symmetry may seem counterintuitive, it must be remembered that axes along which these strain components have been defined correspond to the crystallographic directions [100], [010], and [001]. Indeed, if we instead plot the stress or strain using a cylindrical coordinate system aligned to the growth axis, much of the symmetry we would expect is recovered as shown in Figure 6-14. This Figure shows that plotting the strain along cylindrical

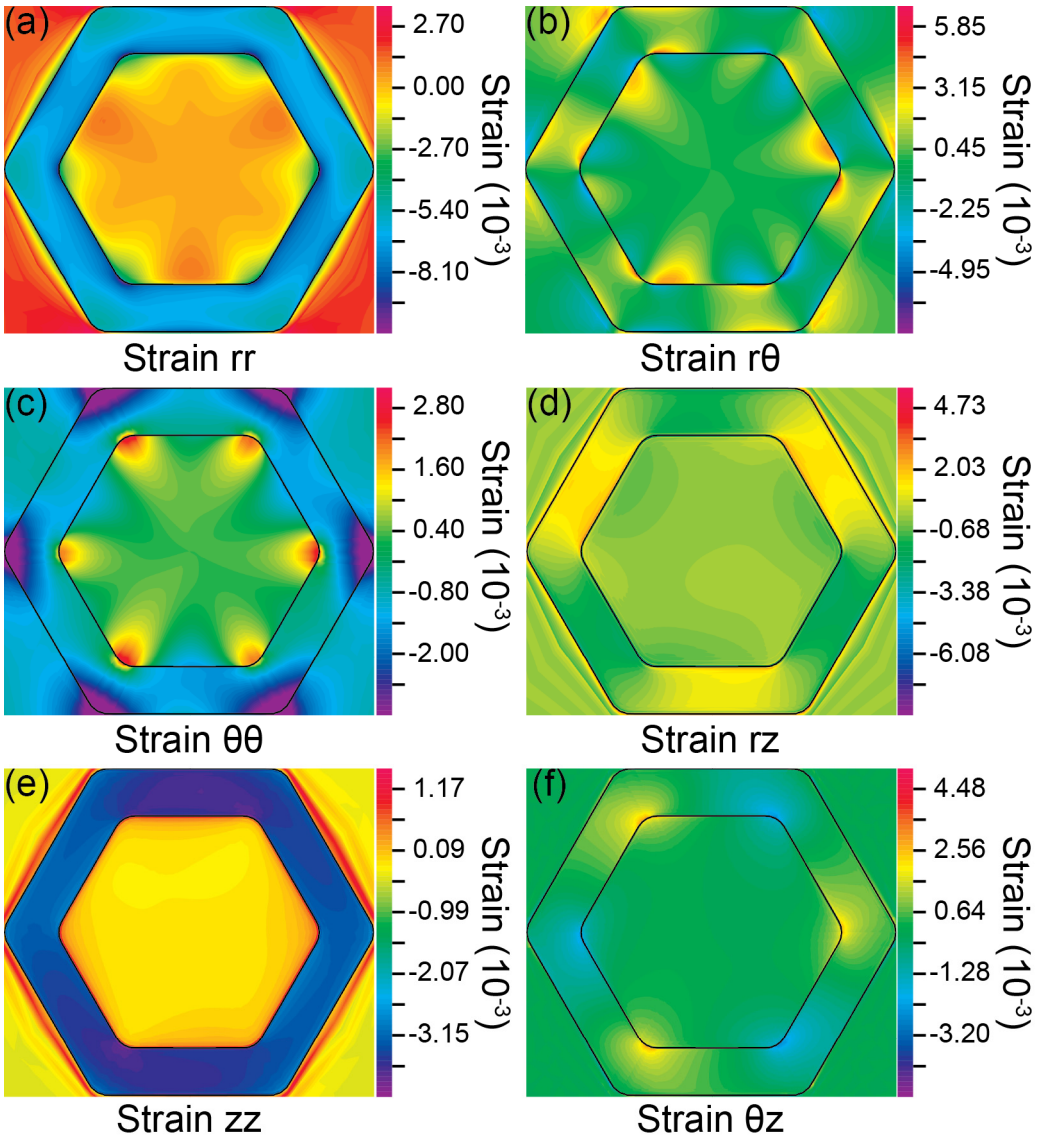

Figure 6-14. Band plots of the (a) radial, (b) hoop, (c) axial, and (e – f) shear components of strain for a core-shell nanowire surrounded by an amorphous carbon coating.

coordinates produces strain fields that exhibit a three-fold symmetry in accordance to the symmetry of the zinc-blende crystal structure along the [111] axis. While the plots in Figure 6-14 convey the strain state of the system more intuitively, the strains plotted in Figure 6-13 are more useful as they can be used as the basis for a second round of CBED simulations.

Using this carbon-coated model, a second iteration of CBED simulations was performed. Figure 6-15 shows a comparison of the simulated HOLZ line shift plots (black dots) of a few facets to the experimental data (colored markers) presented earlier. These simulated plots demonstrate importance of the carbon layer by the superior agreement with experiment than the previous iteration of FEA. Not only does the simulated data exhibit core and shell regions, but the shell regions also show markedly different behavior than previously observed that better correlates to experimental trends. Of particular note is the comparison of simulated Facet 2 with

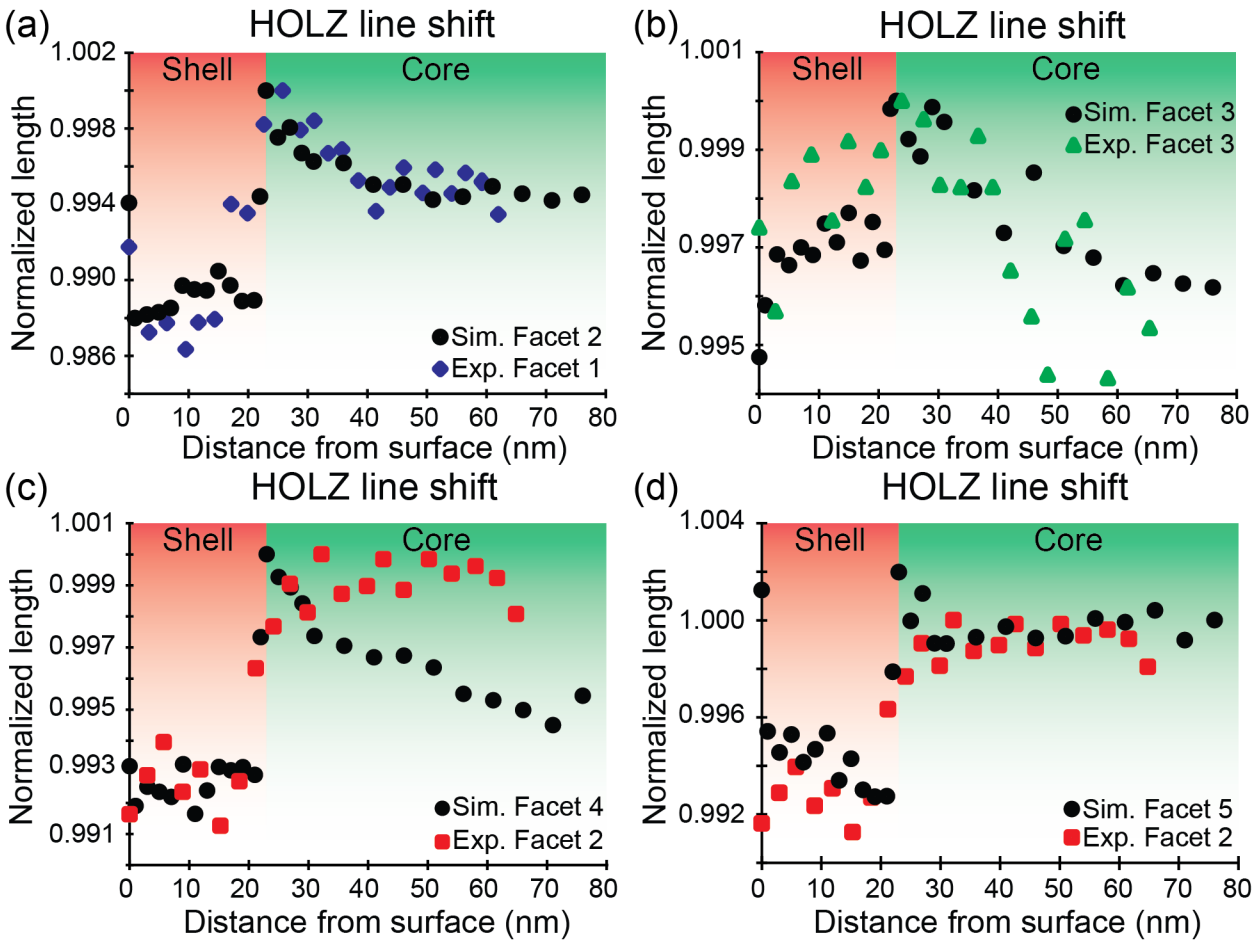

Figure 6-15. Comparison of second-iteration simulated HOLZ line shift plots (black dots) to experimental HOLZ line shift data (colored markers) for some facets.

experimental Facet 1 [Figure 6-15(a)]. Not only do the core and shell regions show a remarkable agreement in magnitude and shape, but the final data point of the simulated series also suggests that the sharp decrease in tie line length seen at the facet surface in the experimental data might not be a simple outlier. In fact, this first experimental data point would seem to indicate that the CBED pattern was indeed obtained from the very top 1 nm of material at the facet surface. The fact that this sharp decrease is not observed in other experimental plots could be due to loss of spatial resolution and projection effects (not suffered by Facet 1) caused by tilting, or more simply that not all facets exhibit this kind of behavior. It should also be noted that this type of behavior is also not present in all of the simulated patterns, as evidenced by simulated Facet 4 [Figure 6-15(c)]. However, out of all six facets simulated only two – Facets 3 and 4 – did not exhibit this initial sharp decrease in tie line length at the facet surface.

Looking at the other facets we can see similar levels of agreement between simulated and experimental plots. Figure 6-15(b) shows an impressive agreement between simulated and experimental Facet 3 in both shape and magnitudes. The high level of noise in the experimental data of Facet 3 could be due to projection effects. If we assume that Facet 1 suffered the least from projection effects, geometry would dictate that Facets 2 and 3 would suffer the most. Experimental Facet 2 presents an interesting case in that its overall appearance seems to agree with simulated results, however, matching it to a specific simulated facet is difficult. While the general shape and magnitude of change between core and shell regions seems right, behavior within each region is more difficult to match to any of the simulated profiles. The best match may be with simulated Facet 5, with discrepancies at the core-shell interface explained by loss of spatial resolution due to tilting.

The fact that the physical nanowire cross-section does vary from the FEA model in a few important respects must also be considered. First is the non-uniform shell thickness at Facet 5. The additional shell material will lead to higher levels of stress on this side of the nanowire affecting the surrounding facets. This additional stress could be a reason why no match could be made for experimental Facet 4 [Figure 6-8(d)], which lies right next to Facet 5, yet Facet 1 which lies further away can be matched to a simulated profile nearly perfectly. In addition to the non-uniform thickness, Figure 6-3(a) also demonstrates that the protective carbon layer does not completely surround the nanowire. In fact, Facet 4 is almost completely free of carbon material,

which has a significant impact on the strain behavior in the shell. Finally, we could also consider that the geometry of the core is not fully correct. ADF-STEM images suggest that there may be some amount of facet rounding. While the model does include fillets at the corners, the facets are assumed to be perfectly flat and sharp at the interface. Creating a more round interface (perhaps by in diffusion of P during shell growth) would certainly change the strain fields at that interface. Simulations of core-shell heterostructures with a circular core do indeed show how the strain fields would change. Figure 6-16 shows how a circular core would lead to flattening of the strain fields in the core. This would naturally lead to less variation of HOLZ line splitting in the core

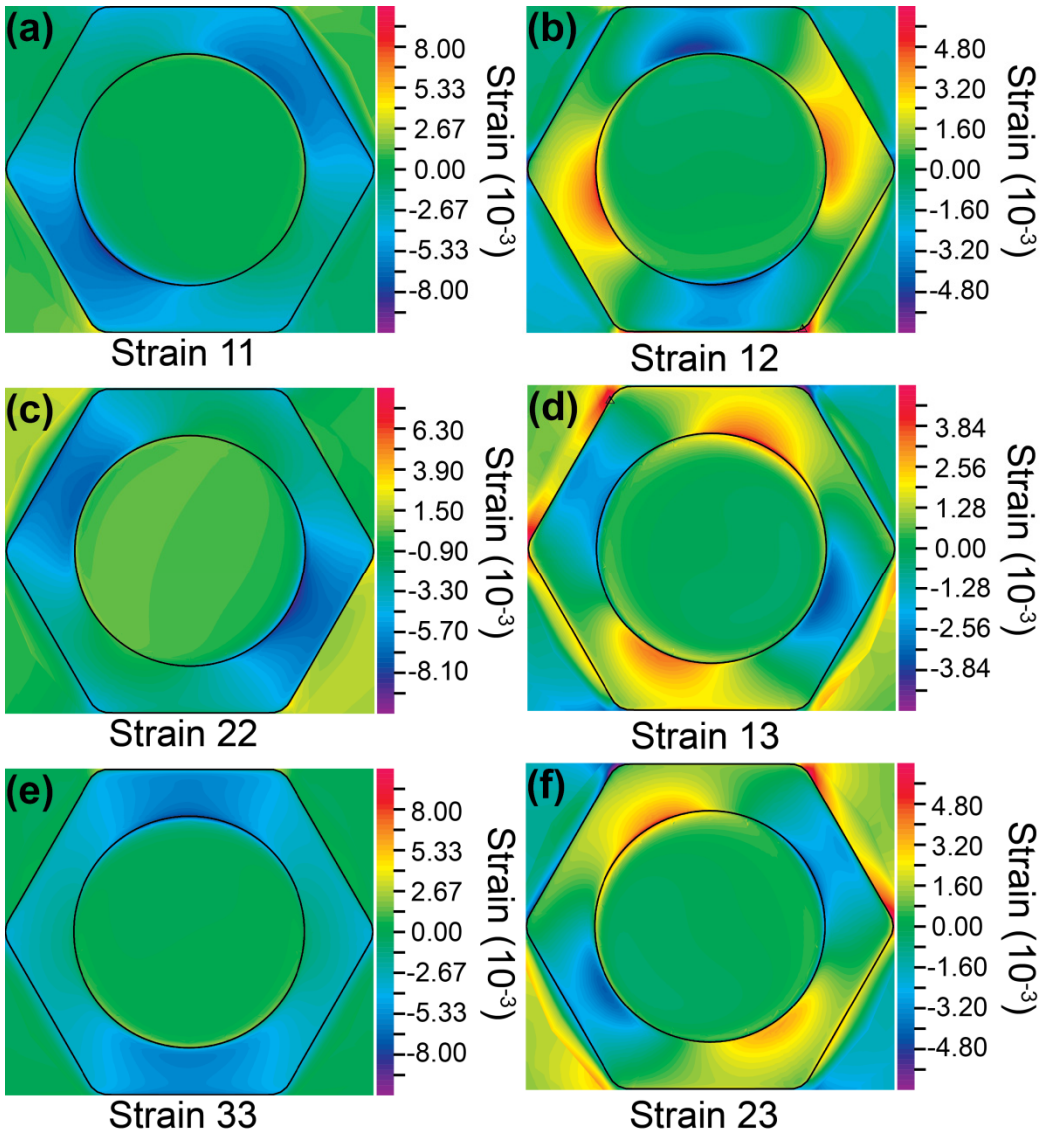

Figure 6-16. Band plots of (a) – (c) normal and (d) – (f) shear strain components of a core-shell nanowire heterostructures with a circular core.

region. While strain fields in the shell are mostly the same, it is observed that the circular core seems to spread out the strain fields in the shell instead of keeping them more confined as seen in Figure 6-13.

A more difficult question that arises when comparing simulated and experimental data is that of facet order. Comparing the two sets of data shows that the best matches are experimental Facet 1/simulated Facet 2 and experimental Facet 3/simulated Facet 3. However, by placing these two facets together, it becomes impossible to match any other facets in an order that agrees with the experimental results. Possible causes could be discrepancies between the model and physical system already mentioned (shell thickness, carbon coating, etc.). Alternatively, it could be that the assumption that the front and back halves of the nanowire cross section are symmetric is wrong. If these two halves are indeed not symmetric, the average strain at any point in the nanowire could be significantly different than what has been calculated here.

As seen in throughout this discussion, small changes in the predicted fields lead to significant changes in the predicted HOLZ line shifting. In turn, the predicted strain fields are seen to be highly dependent on many factors including chemistry, geometry, and local environment. Therefore we believe that, despite the discrepancies mentioned, the matching of experimental and simulated results (Figure 6-15) demonstrate the ability of CBED to accurately measure and map the strain fields in geometrically complex heterostructures such as the GaAs/GaAsP core-shell nanowires analyzed in this investigation.

6.6. Conclusions

Semiconducting nanowires provide a promising and exciting platform for the fabrication of advanced novel optoelectronic devices. Many of these devices will undoubtedly be based on core-shell heterostructures that offer a number of advantages such as surface state passivation and the ability to strain engineer the core material. However, to fully take advantage of these structures it will be vital to understand how strain fields vary throughout the heterostructures, as they could have profound effects on both the fabrication and operation of final devices. This chapter has demonstrated how the combination of electron diffraction simulation techniques enables the mapping of strain fields throughout a core-shell nanowire cross section. By

measuring the shift of HOLZ lines as a function of position we reveal the non-uniformity of the strain fields and demonstrate the ability of CBED to probe the local strain fields of core-shell nanowire heterostructures with nanometer-scale spatial resolution. By comparing these results to those generated from FEA calculations, we can not only get a quantitative understanding of the varying strain field components but also a better understanding of what factors affect the strain fields in the heterostructures. This understanding can be used in the rational design and fabrication of novel heterostructures with specific strain engineering goals, thus opening up new opportunities to take advantage of the promising capabilities semiconducting nanowire heterostructures.

Chapter 7. Conclusions and future work

Strain engineering of semiconducting materials is already standard practice in the design of planar devices. By breaking the symmetry of the crystal structure, the electronic band structure can also be modified allowing for the tuning of band gap energies and electronic carrier mobilities, making strain a key tool for enhancing device performance. As device lengths continue to scale to smaller and smaller sizes, the use nanostructured semiconducting materials will continue to become more important for the realization of advanced optoelectronic devices. Nanostructures not only offer a host of benefits due to electronic confinement in two or more dimensions, but their inherently large surface-to-volume ratio enables them to efficiently relax large strains. This efficient relaxation enables the fabrication of defect-free heterostructures between highly mismatched materials and it presents new opportunities for novel forms of strain engineering. These benefits are especially important for III-V materials systems that exhibit a wide range of lattice constants and are an important materials platform for light emitting devices as their band gap energies also cover the range of visible light.

To optimize the strain in an individual nanostructure, however, the stress and strain fields of that nanostructure must be characterized. Standard techniques for strain characterization in bulk materials, unfortunately, do not possess the spatial resolution needed for such characterization. Methods such as nanobeam XRD, μ-Raman spectroscopy, and photoluminescence have, at best, spatial resolutions on the order of ~100 nm and therefore provide only average values of stress and strain across ensembles of nanostructures. Additionally, the complex geometries of many nanostructured heterointerfaces such as core-shell nanowires mean that stress and strain fields will likely vary across the structure having significant ramification on device fabrication and operation. Such small scale variations are completely missed by these bulk scale techniques.

It was therefore the goal of this thesis to explore and develop the techniques needed to characterize and quantify stress and strain fields at the heterointerface in individual III-V nanostructures with high strain sensitivity and nanoscale spatial resolution. To this end, we identified several TEM based techniques that are best suited to meeting these high demands for characterization. These techniques included convergent beam electron diffraction, nanobeam electron diffraction, and geometric phase analysis. By combining these techniques with relevant

analytical and finite element models, we demonstrated the ability to quantify strain fields in both InAlN/GaN nanoribbon HEMT devices and GaAs/GaAsP core-shell nanowires.

InAlN/GaN nanoribbon HEMT devices were the subject of our strain investigation in chapters 4 and 5. These structures represent both an important device structure for high-power, high-frequency signal applications and a major paradigm of nanostructure fabrication techniques that are likely to be widely used as nanostructures continue to improve – top-down fabrication. Chapter 4 focused on the use of CBED to locally probe the strain fields as a function of distance from the heterointerface. Strain in the sample was evidenced by the splitting of HOLZ contained within CBED patterns taken along the [540]. The fact that lines highly indexed in the *c*-direction (e.g. [117]) show large degrees of splitting while those with low *c*-indices (e.g. [450]) showed little or no splitting was evidence of large variations in the strain component aligned with the growth axis, [0001], with smaller variations in the orthogonal directions. These observations correlated well with FEA calculations of the strain fields which showed variations in the growth direction component almost 10× greater than those calculated along the orthogonal directions. The FEA model also accounted well for the trends in HOLZ line splitting measured using a free surface total relaxation assumption. Finally, we used our FEA model to demonstrate how a passivating layer of Al_2O_3 with increasing thickness could induce an increasing tensile stress in the nanoribbon structure. Correlating these results with electrical measurements of the same structures indicates that the creation of nanoribbons is a promising route towards strain engineering of planar heterostructures and can enhance device performance.

In chapter 5, we extended our study of the InAlN/GaN HEMT devices in an attempt to develop more rapid, facile methods for strain analysis. While CBED is certainly a powerful tool for local strain analysis, the degree of data analysis and simulation work needed to properly interpret the data makes it a cumbersome technique for these highly relevant devices. Therefore, NBED and GPA were used to more directly measure the strain in the HEMT layers. Series of NBED patterns were obtained starting from the bulk and going towards the HEMT structure. By comparing the position of diffraction spots in each NBED pattern to the position of spots in a reference pattern obtained in a strain free area, the strain at each position could be determined. Our results showed an average strain in the HEMT layers of -2.7% ± 0.1% relative to the GaN buffer layer. Maps of the strain across an entire device were produced from lattice resolved

STEM images using GPA. An average strain in the HEMT layers of -2.7% ±0.5% was measured from the strain maps in agreement with our previous NBED measurements. Using these results, the FEA model developed in Chapter 4 was refined and indicates the possibility of a mixing of the HEMT layers during various high temperature processing steps. This mixing was corroborated by lattice resolved STEM images and EDS spectra. NBED and GPA proved to be valuable techniques for the routine strain characterization of nanoscale III-V heterostructures, giving insight into both the strain state of the system and possible changes the structure underwent during processing.

In Chapter 6 we turned our attention to the characterization of GaAs/GaAsP core-shell nanowires. GaAs is an important materials platform for optoelectronic devices due to its direct band gap of 1.42 eV and high electron mobility. With its higher band gap energy and smaller lattice constant, GaAsP is a useful shell material candidate for GaAs as it will be able to confine electrons to the GaAs core and be useful in tuning the band gap via strain. Additionally, GaAsP has been shown to be a promising material for optoelectronic applications in its own right. The wrap-around heterointerface of the core-shell nanowire also presents an interesting extension of the planar interface studied in previous chapters. This 3D interface does, however, eliminate the possibility of using either NBED or GPA due to a lack of unstrained reference material. Therefore, series of CBED patterns along the [556] zone axis are obtained along lines radiating from the center of a nanowire cross section towards the facet and corner surfaces. While little HOLZ line splitting is observed, the HOLZ lines are observed to shift as a function of position. Plotting the HOLZ line shift along four lines going towards facet surfaces, it is observed that no two facets produce the same trend giving evidence of the non-uniform nature of the strain fields. Strain fields are then calculated by FEA and used to calculate series of CBED patterns analogous to the experimental results. By comparing the HOLZ line splitting trends of experimental and simulated series of CBED patterns, we demonstrate that CBED can be used to accurately measure the strain fields in individual nanostructures with spatial resolutions approaching 1 nm.

The results of this thesis also open up new discussion for future work in both the strain engineering of these structures and furthering the characterization of strain. In regards to the InAlN/GaN HEMT structures, our results demonstrated that Al_2O_3 could be used to induce a tensile strain in the nanoribbon structures. Additionally, it was observed from BF-TEM images

that the crystallization of that oxide changed the strain behavior of the system. It would therefore be interesting to further investigate the possibility of using this phase change as a means of further increasing the strain in the system which could lead to increased carrier concentration and enhanced device performance. Additionally, since the geometry of a nanostructure will have significant effects on its strain state, the size and pitch of the nanoribbons could be modeled via FEA and optimized to achieve the best device performance.

Core-multishell nanowires could also be an interesting extension of our work with GaAs/GaAsP heterostructures. The fabrication of a multishell nanowire heterostructure would essentially result in the formation of a radial quantum well. By carefully controlling the compositions of each layer, the stress on that quantum well could be precisely tuned to result in a specified emission energy. The compositions of each layer could be first determined by FEA and the strain state confirmed by CBED. The ability to precisely tune the band gaps of core-multishell wires would be useful in the design of nanowire based light-emitting diodes (LEDs). Not only would the shell provide the proper passivation required for efficient recombination, but the ability to create multiple quantum wells with precisely tuned band gaps would allow for the realization of single-wire, white-light LEDs. Additionally, core-shell nanowires are strong candidates for advanced solar cell materials where the unique nanowire geometry allows for more efficient decoupling of carrier separation and transport. In each of these cases, understanding how strain is distributed throughout the nanowire will be vital in optimizing performance and designing the best structure for a particular application.

There is also additional work that could be done to further characterize the strain in each of our systems. Firstly, since NBED and GPA were determined to be unsuitable techniques for strain quantification in core-shell nanowires, it would be of interest to identify other techniques that could complement the CBED results. It is possible that the non-uniform strain fields could be detected using cathodeluminescence in STEM (CL-STEM). CL-STEM is another nanoscale characterization technique that analyzes the visible light that is emitted from a TEM sample when it is illuminated by the high energy electron beam. If the strain in a core-shell nanowire is large enough to change the band gap of the material, CL-STEM could be able to map those local changes in band gap. Secondly, the HOLZ line splitting observed in many of our CBED patterns (especially those obtained from the InAlN/GaN HEMT structures) could be more accurately

modeled using a multislice calculation. Our approach approximated the deformed material as two pieces of fully relaxed material. This allowed us to approximate the total width of the split HOLZ band using two kinematic simulations. While this method has been shown to provide a good approximation, multislice calculations of HOLZ band rocking curves have been shown able to reproduce these splitting patterns with high levels of accuracy [70, 90, 91]. These types of simulations could shed light on some of the discrepancies we encountered in our analysis of the split HOLZ line patterns and could even allow us to model the non-symmetric splitting observed in patterns obtained from core-shell nanowires.

Appendix A. Using JEMS for the simulation of CBED patterns

Chapter 3 presented and discussed the theory behind Bloch wave calculations of CBED patterns. In practice, these simulations were performed using the JEMS software suite developed by Pierre Stadelmann. This software suite provides a convenient tool set for the analysis of a range of TEM data. In this investigation, this software was primarily used for the indexing of HOLZ line patterns using kinematic simulations (Figure A-1) and simulations of CBED patterns under given

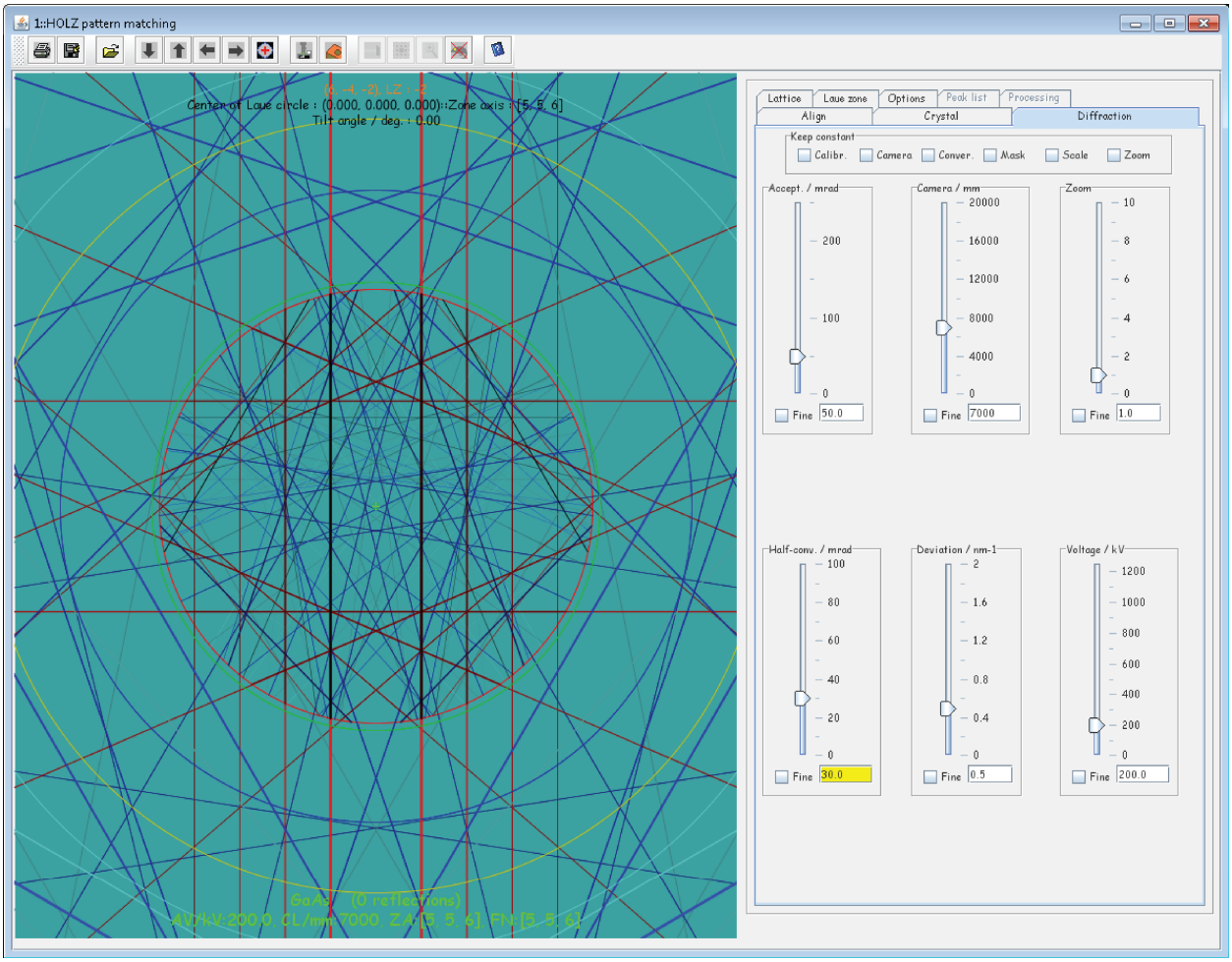

Figure A-1. User interface of the JEMS software package showing a kinematic simulation of the [556] zone axis in GaAs

strain states via Bloch wave analysis.

As discussed in Chapter 3, the simulated CBED pattern will largely depend on the thickness of the simulated crystal, number of beams taken into account, and the periodic potential through

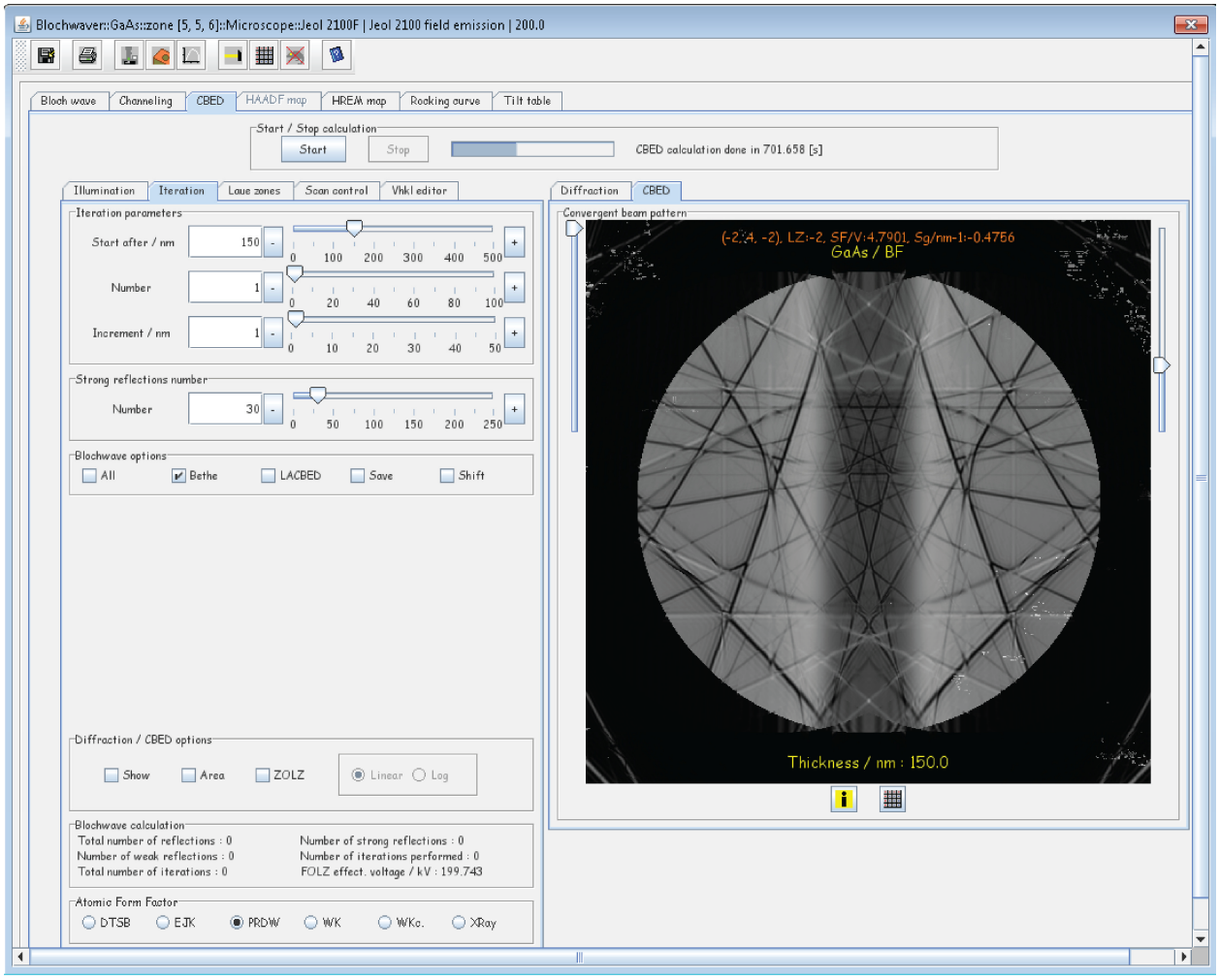

Figure A-2. User interface of the JEMS software package showing a dynamic simulation of the [556] zone axis in GaAs using 30 beams, a thickness of 150 nm, and the generalized Bethe potentials for approximating weak beam contributions

which the electron beam is propagating (i.e. the crystal lattice). While the thickness and number of beams are selected directly through the user interface (Figure A-2), the crystal lattice is input into JEMS via a crystal file. Each crystal file contains information about the number of atoms, the atom locations within the unit cell, the symmetry of the crystal, and the absorption coefficients for each atom. Two examples of these crystal files are shown below. The first is an example of a strained region of the GaAs nanowire core while the second is a strained region of the GaAsP shell. Within each of these files, the lattice constants – shown in bold – are designated as lattice|0|, |1|, |2|, |3|, |4|, and |5| and correspond to a, b, c, α, β, and γ respectively. These lattice constants in turn correspond to the 11, 33, 22, 23, 13, and 12 strain components defined in Chapter 5.

A.1. Example files

Strained GaAs

---

file|C:\ GaAs-z00.txt

name|GaAs-z00

creator|Admin

date|Fri Aug 15 11:42:13 EDT 2014

system|cubic

superCell|false

HMSymbol|216|24|0|0|0| F -4 3 m

rps|0|x , y , z

rps|1|x , -y , -z

rps|2|-x , y , -z

rps|3|-x , -y , z

rps|4|y , z , x

rps|5|-y , -z , x

rps|6|y , -z , -x

rps|7|-y , z , -x

rps|8|z , x , y

rps|9|-z , x , -y

rps|10|-z , -x , y

rps|11|z , -x , -y

rps|12|y , x , z

rps|13|-y , x , -z

rps|14|y , -x , -z

rps|15|-y , -x , z

rps|16|z , y , x

rps|17|-z , -y , x

rps|18|-z , y , -x

rps|19|z , -y , -x

rps|20|x , z , y

rps|21|x , -z , -y

rps|22|-x , -z , y

rps|23|-x , z , -y

lattice|0|0.565168

lattice|1|0.565162

lattice|2|0.565142

lattice|3|89.99299

lattice|4|89.99004

lattice|5|89.99592

atom|0|Ga,a,0.000,0.000,0.000,0.005,1.000,0.052,Def,0

atom|1|As,a,0.250,0.250,0.250,0.005,1.000,0.054,Def,0

aff|0|Ga|2.321,65.602,2.486,15.458,1.688,2.581,0.599,0.351|Doyle - Turner Acta Cryst. A24 (1968), 390

aff|1|As|2.399,45.718,2.79,12.817,1.529,2.28,0.594,0.328|Doyle - Turner Acta Cryst. A24 (1968), 390

aff|0|Ga|2.0431533,2.3264925,0.6215586,0.10935888,0.31280488,52.6676030.33151004,0.74415857,0.007030542,0.030718058,0.20452403,0.3298532|Earl J. Kirkland, Advanced Computing in Electron Microscopy

aff|1|As|0.76611197,0.14471085,1.9732872,1.7414166,0.6674049,188.379580.010006787,0.022706127,0.18018197,0.33255133,0.82346374,5.8580494|Earl J. Kirkland, Advanced Computing in Electron Microscopy

nsl|0|Ga|0.72

nsl|1|As|0.673

aff|0|Ga|0.2135,0.102,0.9768,1.0219,1.6669,4.6275,2.5662,22.8742,1.679,80.1535|L. Peng et al., Acta Cryst. A52 (1996) 257-276::Def

aff|1|As|0.2059,0.0926,0.9518,0.9182,1.6372,4.3291,3.049,19.2996,1.4756,58.9329|L. Peng et al., Acta Cryst. A52 (1996) 257-276::Def

aff|0|Ga|15.2354,3.0669,6.7006,0.2412,4.3591,10.7805,2.9623,61.4135,1.7189|XRay:: RHF::Def

aff|1|As|16.6723,2.6345,6.0701,0.2647,3.4313,12.9479,4.2779,47.7972,2.531|XRay:: RHF::Def

---

Strained GaAsP shell

---

file|C:\Users\Admin\Desktop\User Data\Eric\JEMS\GaAs\Corrected\Multishell\Facet2\GaAsP-z46.txt

name|GaAsP-z46

creator|Admin

date|Mon Aug 18 17:49:30 EDT 2014

system|cubic

superCell|false

HMSymbol|216|24|0|0|0| F -4 3 m

rps|0|x , y , z

rps|1|x , -y , -z

rps|2|-x , y , -z

rps|3|-x , -y , z

rps|4|y , z , x

rps|5|-y , -z , x

rps|6|y , -z , -x

rps|7|-y , z , -x

rps|8|z , x , y

rps|9|-z , x , -y

rps|10|-z , -x , y

rps|11|z , -x , -y

rps|12|y , x , z

rps|13|-y , x , -z

rps|14|y , -x , -z

rps|15|-y , -x , z

rps|16|z , y , x

rps|17|-z , -y , x

rps|18|-z , y , -x

rps|19|z , -y , -x

rps|20|x , z , y

rps|21|x , -z , -y

rps|22|-x , -z , y

rps|23|-x , z , -y

lattice|0|0.565030

lattice|1|0.562877

lattice|2|0.565018

lattice|3|90.00905

lattice|4|90.01155

lattice|5|89.97891

atom|0|Ga,a,0.000,0.000,0.000,0.005,1.000,0.052,Def,0

atom|1|As,a,0.250,0.250,0.250,0.005,0.900,0.054,Def,0

atom|2|P ,a,0.250,0.250,0.250,0.005,0.100,0.036,Def,0

aff|0|Ga|2.321,65.602,2.486,15.458,1.688,2.581,0.599,0.351|Doyle - Turner Acta Cryst. A24 (1968), 390

aff|1|As|2.399,45.718,2.79,12.817,1.529,2.28,0.594,0.328|Doyle - Turner Acta Cryst. A24 (1968), 390

aff|2|P |1.888,44.876,2.469,13.538,0.805,2.642,0.32,0.361|Doyle - Turner Acta Cryst. A24 (1968), 390

aff|0|Ga|2.0431533,2.3264925,0.6215586,0.10935888,0.31280488,52.6676030.33151004,0.74415857,0.007030542,0.030718058,0.20452403,0.3298532|Earl J. Kirkland, Advanced Computing in Electron Microscopy

aff|1|As|0.76611197,0.14471085,1.9732872,1.7414166,0.6674049,188.379580.010006787,0.022706127,0.18018197,0.33255133,0.82346374,5.8580494|Earl J. Kirkland, Advanced Computing in Electron Microscopy

aff|2|P|0.30971116,0.12479106,0.11825268,109.17846,1.0443068,1.34549590.026600024,0.18309815,0.9433259,2.8834162,1.3413857,7.549608|Earl J. Kirkland, Advanced Computing in Electron Microscopy

nsl|0|Ga|0.72

nsl|1|As|0.673

nsl|2|P |0.513

aff|0|Ga|0.2135,0.102,0.9768,1.0219,1.6669,4.6275,2.5662,22.8742,1.679,80.1535|L. Peng et al., Acta Cryst. A52 (1996) 257-276::Def

aff|1|As|0.2059,0.0926,0.9518,0.9182,1.6372,4.3291,3.049,19.2996,1.4756,58.9329|L. Peng et al., Acta Cryst. A52 (1996) 257-276::Def

aff|2|P |0.1005,0.0977,0.4615,0.9084,1.0663,4.9654,2.5854,18.5471,1.2725,54.3648|L. Peng et al., Acta Cryst. A52 (1996) 257-276::Def

aff|0|Ga|15.2354,3.0669,6.7006,0.2412,4.3591,10.7805,2.9623,61.4135,1.7189|XRay:: RHF::Def

aff|1|As|16.6723,2.6345,6.0701,0.2647,3.4313,12.9479,4.2779,47.7972,2.531|XRay:: RHF::Def

aff|2|P |6.4345,1.9067,4.1791,27.157,1.78,0.526,1.4908,68.1645,1.1149|XRay:: RHF::Def

---

Bibliography

[1] D. B. Williams and C. B. Carter, *Transmission electron microscopy : a textbook for materials science*, 2nd ed. New York ; London: Springer, 2008.

[2] H. L. Ibach, Hans, *Solid-state physics: An introduction to principles of materials science*, 4th ed. ed. Berlin; New York: Springer, 2009.

[3] H. Jorke*, et al.*, "SECONDARY IMPLANTATION OF SB INTO SI MOLECULAR-BEAM EPITAXY LAYERS," *Applied Physics Letters,* vol. 47, pp. 511-513, 1985.

[4] J. Welser*, et al.*, "ELECTRON-MOBILITY ENHANCEMENT IN STRAINED-SI N-TYPE METAL-OXIDE-SEMICONDUCTOR FIELD-EFFECT TRANSISTORS," *Ieee Electron Device Letters,* vol. 15, pp. 100-102, Mar 1994.

[5] J. Welser*, et al.*, *STRAIN DEPENDENCE OF THE PERFORMANCE ENHANCEMENT IN STRAINED-SI N-MOSFETS*. New York: I E E E, 1994.

[6] D. Chrastina*, et al.*, "Patterning-induced strain relief in single lithographic SiGe nanostructures studied by nanobeam x-ray diffraction," *Nanotechnology,* vol. 23, Apr 2012.

[7] J. Xiang*, et al.*, "Ge/Si nanowire heterostructures as high-performance field-effect transistors," *Nature,* vol. 441, pp. 489-493, May 2006.

[8] N. Sköld*, et al.*, "Growth and Optical Properties of Strained GaAs−GaxIn1-xP Core−Shell Nanowires," *Nano Letters,* vol. 5, pp. 1943-1947, 2005.

[9] G. Signorello*, et al.*, "Tuning the light emission from GaAs nanowires over 290 meV with uniaxial strain," *Nano Letters,* vol. 13, pp. 917-924, 2013.

[10] M. Montazeri*, et al.*, "Direct Measure of Strain and Electronic Structure in GaAs/GaP Core-Shell Nanowires," *Nano Letters,* vol. 10, pp. 880-886, Mar 2010.

[11] Q. M. Li and G. T. Wang, "Strain influenced indium composition distribution in GaN/InGaN core-shell nanowires," *Applied Physics Letters,* vol. 97, p. 3, Nov 2010.

[12] F. Ponce*, et al.*, "Microstructure and electronic properties of InGaN alloys," *Physica Status Solidi (B),* vol. 240, pp. 273-284, 2003.

[13] K. Hestroffer, *et al.*, "The structural properties of GaN/AlN core-shell nanocolumn heterostructures," *Nanotechnology,* vol. 21, p. 7, Oct 2010.

[14] M. Keplinger, *et al.*, "Structural Investigations of Core-shell Nanowires Using Grazing Incidence X-ray Diffraction," *Nano Letters,* vol. 9, pp. 1877-1882, May 2009.

[15] A. Biermanns, *et al.*, "Axial strain in GaAs/InAs core-shell nanowires," *Applied Physics Letters,* vol. 102, Jan 2013.

[16] V. Laneuville, *et al.*, "Double strain state in a single GaN/AlN nanowire: Probing the core-shell effect by ultraviolet resonant Raman scattering," *Physical Review B,* vol. 83, 2011.

[17] D. Ferrand and J. Cibert, "Strain in crystalline core-shell nanowires," *European Physical Journal-Applied Physics,* vol. 67, Sep 2014.

[18] Z. H. Feng, *et al.*, "Enhanced thermal stability of the two-dimensional electron gas in GaN/AlGaN/GaN heterostructures by Si3N4 surface-passivation-induced strain solidification," *Applied Physics Letters,* vol. 85, pp. 5248-5250, Nov 2004.

[19] D. Qiao, *et al.*, "Dependence of Ni/AlGaN Schottky barrier height on Al mole fraction," *Journal of Applied Physics,* vol. 87, pp. 801-804, Jan 2000.

[20] J. Kuzmik, "Power electronics on InAlN/(In)GaN: Prospect for a record performance," *Ieee Electron Device Letters,* vol. 22, pp. 510-512, Nov 2001.

[21] J. Kuzmik, "InAlN/(In)GaN high electron mobility transistors: some aspects of the quantum well heterostructure proposal," *Semiconductor Science and Technology,* vol. 17, pp. 540-544, Jun 2002.

[22] M. Mikulics, *et al.*, "InAlN/GaN/Si heterostructures and field-effect transistors with lattice matched and tensely or compressively strained InAlN," *Applied Physics Letters,* vol. 97, p. 173505, 2010.

[23] M. Azize and T. Palacios, "Top-down fabrication of AlGaN/GaN nanoribbons," *Applied Physics Letters,* vol. 98, p. 042103, 2011.

[24] M. Azize, *et al.*, "High-Electron-Mobility Transistors Based on InAlN/GaN Nanoribbons," *Ieee Electron Device Letters,* vol. 32, pp. 1680-1682, Dec 2011.

[25] J. H. Paek, *et al.*, "Structural and optical properties of a catalyst-free GaAs/AlGaAs core–shell nano/microwire grown on (111)Si substrate," *Physica E: Low-dimensional Systems and Nanostructures,* vol. 42, pp. 2722-2726, 2010.

[26] C. Yoon, *et al.*, "Flexible logic gates composed of high performance GaAs-nanowire-based MESFETs with MHz-dynamic operations," *Nanotechnology,* vol. 22, p. 465202, 2011 Nov 18 (Epub 2011 Oct 2011.

[27] B. Hua, *et al.*, "Single GaAs/GaAsP Coaxial Core-Shell Nanowire Lasers," *Nano Letters,* vol. 9, pp. 112-116, Jan 2009.

[28] K. Tomioka, *et al.*, "GaAs/AlGaAs Core Multishell Nanowire-Based Light-Emitting Diodes on Si," *Nano Letters,* vol. 10, pp. 1639-1644, May 2010.

[29] M. J. Tambe, *et al.*, "Realization of defect-free epitaxial core-shell GaAs/AlGaAs nanowire heterostructures," *Applied Physics Letters,* vol. 93, p. 151917, 2008.

[30] S. Adachi, "GAAS, ALAS, AND ALXGA1-XAS - MATERIAL PARAMETERS FOR USE IN RESEARCH AND DEVICE APPLICATIONS," *Journal of Applied Physics,* vol. 58, pp. R1-R29, 1985.

[31] R. Dingle, *et al.*, "ELECTRON MOBILITIES IN MODULATION-DOPED SEMICONDUCTOR HETEROJUNCTION SUPER-LATTICES," *Applied Physics Letters,* vol. 33, pp. 665-667, 1978.

[32] O. D. D. Couto, *et al.*, "Effect of a GaAsP Shell on the Optical Properties of Self-Catalyzed GaAs Nanowires Grown on Silicon," *Nano Letters,* vol. 12, pp. 5269-5274, Oct 2012.

[33] H. Sawada, *et al.*, "STEM imaging of 47-pm-separated atomic columns by a spherical aberration-corrected electron microscope with a 300-kV cold field emission gun," *Journal of Electron Microscopy,* vol. 58, pp. 357-361, Dec 2009.

[34] H. Niedrig and E. I. Rau, "Information depth and spatial resolution in BSE microtomography in SEM," *Nuclear Instruments & Methods in Physics Research Section B-Beam Interactions with Materials and Atoms,* vol. 142, pp. 523-534, Aug 1998.

[35] E. I. Rau and L. Reimer, "Fundamental problems of imaging subsurface structures in the backscattered electron mode in scanning electron microscopy," *Scanning,* vol. 23, pp. 235-240, Jul-Aug 2001.

[36] G. E. Lloyd, "Atomic-number and crystallographic contrast images with the SEM - A review of backscattered electron techniques," *Mineralogical Magazine,* vol. 51, pp. 3-19, Mar 1987.

[37] M. D. Vaudin*, et al.*, "Comparison of nanoscale measurements of strain and stress using electron back scattered diffraction and confocal Raman microscopy," *Applied Physics Letters,* vol. 93, Nov 2008.

[38] W. L. Bragg and J. J. Thomson, "The diffraction of short electromagnetic waves by a crystal," *Proceedings of the Cambridge Philosophical Society,* vol. 17, pp. 43-57, May 1914.

[39] P. Ewald, "Contributions to the theory of the interferences of X-rays in crystals," *Phys. Z,* vol. 14, pp. 465-472, 1913.

[40] P. M. Jones*, et al.*, "Higher Order Laue Zone Effects in Electron Diffraction and their Use in Lattice Parameter Determination," *Proceedings of the Royal Society A: Mathematical, Physical and Engineering Sciences,* vol. 354, pp. 197-222, 1977.

[41] R. Wittmann*, et al.*, "Quantitative determination of lattice parameters from CBED patterns: accuracy and performance," *Ultramicroscopy,* vol. 70, pp. 145-159, Jan 1998.

[42] J. M. Zuo*, et al.*, "A new approach to lattice parameter measurements using dynamic electron diffraction and pattern matching," *Journal of Electron Microscopy,* vol. 47, pp. 121-127, 1998.

[43] A. Chuvilin, "On the origin of HOLZ lines splitting near interfaces: multislice simulation of CBED patterns," *Journal of Electron Microscopy,* vol. 54, pp. 515-517, 2005.

[44] A. Béché*, et al.*, "Improved precision in strain measurement using nanobeam electron diffraction," *Applied Physics Letters,* vol. 95, Sep 2009.

[45] M. J. Hytch*, et al.*, "Quantitative measurement of displacement and strain fields from HREM micrographs," *Ultramicroscopy,* vol. 74, pp. 131-146, Aug 1998.

[46] J. L. Rouvière and E. Sarigiannidou, "Theoretical discussions on the geometrical phase analysis," *Ultramicroscopy,* vol. 106, pp. 1-17, Dec 2005.

[47] D. Cooper*, et al.*, "Strain mapping with nm-scale resolution for the silicon-on-insulator generation of semiconductor devices by advanced electron microscopy," *Journal of Applied Physics,* vol. 112, Dec 2012.

[48] D. Cooper*, et al.*, "Strain mapping for the silicon-on-insulator generation of semiconductor devices by high-angle annular dark field scanning electron transmission microscopy," *Applied Physics Letters,* vol. 100, Jun 2012.

[49] S. D. Findlay*, et al.*, "Enhanced light element imaging in atomic resolution scanning transmission electron microscopy," *Ultramicroscopy,* vol. 136, pp. 31-41, Jan 2014.

[50] X. H. Sang and J. M. LeBeau, "Revolving scanning transmission electron microscopy: Correcting sample drift distortion without prior knowledge," *Ultramicroscopy,* vol. 138, pp. 28-35, Mar 2014.

[51] K.-J. Bathe, *Finite element procedures*. Englewood Cliffs, N.J.: Prentice Hall, 1996.

[52] T. E. Trammell*, et al.*, "Equilibrium strain-energy analysis of coherently strained core–shell nanowires," *Journal of Crystal Growth,* vol. 310, pp. 3084-3092, 2008.

[53] Y. Liang*, et al.*, "Critical thickness enhancement of epitaxial SiGe films grown on small structures," *Journal of Applied Physics,* vol. 97, p. 7, Feb 2005.

[54] Y. Liang*, et al.*, "Critical thickness enhancement of epitaxial SiGe films grown on small structures," *Journal of Applied Physics,* vol. 97, Feb 2005.

[55] Y. A. Burenkov*, et al.*, "Temperature-dependence of gallium-arsenide elastic-constants," *Fizika Tverdogo Tela,* vol. 15, pp. 1757-1761, 1973.

[56] Y. A. Burenkov*, et al.*, "Elastic properties of indium-arsenide," *Fizika Tverdogo Tela,* vol. 17, pp. 2183-2186, 1975.

[57] S. Christiansen*, et al.*, "Strained state of Ge(Si) islands on Si: Finite element calculations and comparison to convergent beam electron-diffraction measurements," *Applied Physics Letters,* vol. 64, p. 3617, 1994.

[58] P. Stadelmann. (2004, 1/17/2012). *jems opening page sept 21 2004* [Webpage]. Available: http://cimewww.epfl.ch/people/stadelmann/jemswebsite/jems.html

[59] P. A. Stadelmann, "EMS - A software package for electron-diffraction analysis and HREM image simulation in materials science," *Ultramicroscopy,* vol. 21, pp. 131-145, 1987.

[60] H. Bethe, "Theory on the diffraction of electrons in crystals," *Annalen Der Physik,* vol. 87, pp. 55-129, Oct 1928.

[61] M. Ichikawa and K. Hayakawa, "Generlized Bethe potential in reflection electron-diffraction," *Journal of the Physical Society of Japan,* vol. 42, pp. 1957-1964, 1977.

[62] M. Saunders*, et al.*, "The use of Bethe potentials in zone-axis CBED pattern matching," *Ultramicroscopy,* vol. 65, pp. 45-52, Sep 1996.

[63] K. Tsuda and M. Tanaka, "Refinement of crystal structure parameters using convergent-beam electron diffraction - The low-temperature phase of SrTiO3," *Acta Crystallographica Section A,* vol. 51, pp. 7-19, Jan 1995.

[64] D. Fournier*, et al.*, "Systematic procedure for indexing HOLZ lines in convergent beam electron diffraction patterns of cubic crystal," *Journal of Electron Microscopy Technique,* vol. 13, pp. 123-149, Oct 1989.

[65] T. Martensson*, et al.*, "Epitaxial III-V nanowires on silicon," *Nano Letters,* vol. 4, pp. 1987-1990, Oct 2004.

[66] F. Qian*, et al.*, "Core/multishell nanowire heterostructures as multicolor, high-efficiency light-emitting diodes," *Nano. Lett.,* vol. 5, pp. 2287-2291, 2005.

[67] F. Qian*, et al.*, "Controlled Synthesis of AlN/GaN Multiple Quantum Well Nanowire Structures and Their Optical Properties," *Nano Letters,* vol. 12, pp. 3344-3350, Jun 2012.

[68] R. Balboni*, et al.*, "Determination of bulk mismatch values in transmission electron microscopy cross-sections of heterostructures by convergent-beam electron diffraction," *Philosophical Magazine a-Physics of Condensed Matter Structure Defects and Mechanical Properties,* vol. 77, pp. 67-83, Jan 1998.

[69] C. T. Chou, *et al.*, "SURFACE RELAXATION OF STRAINED HETEROSTRUCTURES REVEALED BY BRAGG LINE SPLITTING IN LACBED PATTERNS," *Ultramicroscopy,* vol. 55, pp. 334-347, Sep 1994.

[70] F. Houdellier, *et al.*, "Quantitative analysis of HOLZ line splitting in CBED patterns of epitaxially strained layers," *Ultramicroscopy,* vol. 106, pp. 951-959, 2006.

[71] L. Clément, *et al.*, "Strain measurements by convergent-beam electron diffraction: The importance of stress relaxation in lamella preparations," *Applied Physics Letters,* vol. 85, p. 651, 2004.

[72] M. Fieger, *et al.*, "MOVPE, processing and characterization of AlGaN/GaN HEMTs with different Al concentrations on silicon substrates," *Journal of Crystal Growth,* vol. 298, pp. 843-847, Jan 2007.

[73] J. Kuzmik, *et al.*, "InAlN/GaN HEMTs: A first insight into technological optimization," *IEEE Transactions on Electron Devices,* vol. 53, pp. 422-426, Mar 2006.

[74] M. Tanaka and K. Tsuda, "Convergent-beam electron diffraction," *Journal of Electron Microscopy,* vol. 60, pp. S245-S267, Aug 2011.

[75] A. F. Wright, "Elastic properties of zinc-blende and wurtzite AlN, GaN, and InN," *Journal of Applied Physics,* vol. 82, pp. 2833-2839, Sep 1997.

[76] S. C. Seel, *et al.*, "Tensile stress evolution during deposition of Volmer-Weber thin films," *Journal of Applied Physics,* vol. 88, pp. 7079-7088, Dec 2000.

[77] E. J. Jones, *et al.*, "Correlating stress generation and sheet resistance in InAlN/GaN nanoribbon high electron mobility transistors," *Applied Physics Letters,* vol. 101, p. 113101, Sep 2012.

[78] S. Rubanov and P. R. Munroe, "FIB-induced damage in silicon," *Journal of Microscopy-Oxford,* vol. 214, pp. 213-221, Jun 2004.

[79] A. Armigliato, *et al.*, "Electron diffraction with ten nanometer beam size for strain analysis of nanodevices," *Applied Physics Letters,* vol. 93, Oct 2008.

[80] A. Béché, "Mesure de déformation à l'échelle nanometrique par microscopie électronique en transmission," Doctorate, Institut Polytechnique de Grenoble, Grenoble, 2009.

[81] M. M. J. Treacy, *et al.*, "Z-CONTRAST OF PLATINUM AND PALLADIUM CATALYSTS," *Philosophical Magazine a-Physics of Condensed Matter Structure Defects and Mechanical Properties,* vol. 38, pp. 569-585, 1978.

[82] N. J. Ekins-Daukes, *et al.*, "Strain-balanced GaAsP/InGaAs quantum well solar cells," *Applied Physics Letters,* vol. 75, pp. 4195-4197, Dec 1999.

[83] O. Schuler, *et al.*, "A gas-source MBE growth study of strained Ga1-xInxP layers on GaAs," *Journal of Crystal Growth,* vol. 201, pp. 280-283, May 1999.

[84] N. Skold, *et al.*, "Growth and optical properties of strained GaAs-GaxIn1-xP core-shell nanowires," *Nano Letters,* vol. 5, pp. 1943-1947, Oct 2005.

[85] A. Pevzner, *et al.*, "Knocking Down Highly-Ordered Large-Scale Nanowire Arrays," *Nano Letters,* vol. 10, pp. 1202-1208, Apr 2010.

[86] M. Keplinger, *et al.*, "Core-shell nanowires: From the ensemble to single-wire characterization," *Nuclear Instruments & Methods in Physics Research Section B-Beam Interactions with Materials and Atoms,* vol. 268, pp. 316-319, Feb 2010.

[87] D. Holec, *et al.*, "HANSIS software tool for the automated analysis of HOLZ lines," *Ultramicroscopy,* vol. 109, pp. 837-844, Jun 2009.

[88] Y. K. Yogurtcu, *et al.*, "Pressure dependence of elastic behavior and force constants of GaP," *Journal of Physics and Chemistry of Solids,* vol. 42, pp. 49-56, 1981.

[89] C. S. Kim and S. H. Ahn, "Mechanical Behavior of Microscale Carbon Pillar Fabricated by Focused Ion Beam Induced Deposition," *International Journal of Precision Engineering and Manufacturing,* vol. 15, pp. 1485-1488, Jul 2014.

[90] F. Houdellier, *et al.*, "New approach for the dynamical simulation of CBED patterns in heavily strained specimens," *Ultramicroscopy,* vol. 108, pp. 426-432, Apr 2008.

[91] F. Houdellier, *et al.*, "Convergent beam electron diffraction for strain determination at the nanoscale," *Microelectronic Engineering,* vol. 84, pp. 464-467, Mar 2007.